Synthesis and Thermoelectric Properties of

Chalcogenide and Half-Heusler Phases

Von der Fakultät Chemie der Universität Stuttgart

zur Erlangung der Würde eines Doktors der

Naturwissenschaft (Dr. rer. nat.) genehmigte Abhandlung

Vorgelegt von

Tianhua Zou

aus Weihai Shandong, China

Hauptberichter:	**Prof. Dr. Anke Weidenkaff**
Mitberichter:	**Prof. Dr. Rainer Niewa**
Prüfungsausschussvorsitzender:	**Prof. Dr. Thomas Schleid**

Tag der mündlichen Prüfung: 08. Januar 2018

Institut für Materialwissenschaft der Universität Stuttgart

2018

Statement of Authorship

Hereby I declare that the Ph.D. thesis "Synthesis and Thermoelectric Properties of Chalcogenide and Half-Heusler Phases" is my original work without using any other sources except for the ones indicated, and the electronic version of the thesis is the same with the printed version.

Stuttgart, 04 December 2017 _____

Tianhua Zou

Table of Contents

List of Abbreviations

TE   Thermoelectric

PF   Power Factor

XRD   X-ray Diffraction

SPS   Spark Plasma Sintering

SEM   Scanning Electron Microscope

LFA   Laser Flash Apparatus

eDOS   Electronic Density of States

PPMS   Physical Property Measurement System

AM   Arc Melting

FH   Full-Heusler

HH   Half-Heusler

RT   Room Temperature

PGEC   Phonon-Glass Electron-Crystal Approach

TEM   Transmission Electron Microscope

SPB   Single Parabolic Band

XPS   X-ray Photoelectron Spectroscopy

Acknowledgements

First and foremost, I express my sincere gratitude to my research supervisor: Prof. Dr. Anke Weidenkaff. Prof. Dr. Anke Weidenkaff is a high academic standards material scientist and chemist. I feel grateful and honored to be her student. Although she has many duties and responsibilities in several academic associations (MRS, EMRS, ETS and DFG), she joins our weekly group meeting and leads as well as inspires our scientific discussions. I am extremely thankful to her guidance and supports.

I want to express my sincere thanks to my group leader, Dr. Wenjie Xie. Dr. Wenjie Xie helps me acquire basic experimental skills and gives me a lot of beneficial tips. We have lots of fruitful experimental results and discussions together. I would like to thank him for his patient guidance and useful comments on my experiments, thesis and publications.

I want to express my thanks to our co-workers, both past and present. Dr. Marc Widenmeyer, an expert on XRD, he helps me with the data refinement. I would like to thank Dr. Widenmeyer for the translation of German abstract in this thesis and Dr. Pingjun Ying for useful comments on the thesis. I would like to thank Dr. Song Hak Yoon and M.Sc. Cora Bubeck for the helping of the fullprof. I would like to thank M.Sc. Xingxing Xiao for the cooperation in the lab courses, Dr. Benjamin Balke for DSC measurement, M.Sc. Timotheus Jahnke for SEM measurement, M.Sc. Stefan Kilper for nanoindentation measurement and M.Sc. Achim Diem for coating the Hall samples. I would like to thank Dr. Dirk Rothenstein and Dr. Petia Atanasova for safety training. I would like to thank Lukas Fink for purchasing the materials and Dr. Angelika Veziridis for intensively correcting English. I would like to thank M.Sc. Weiwu Li and Prof. Dr. Martin Dressel for the band gap measurement. I would like to thank M.Sc. Yufei Liu, Prof. Dr. Jian He and Prof. Dr. Terry M. Tritt from Department of Physics and Astronomy of Clemson University for the useful discussion on the experiments. I would like to thank Dr. Zhicheng Zhong and Dr. Philipp Hansmann from Max-Planck-Institut für Festkörperforschung for the calculation of the band structure of chalcogenide. I would like to thank M.Sc. Tiantian Jia and Prof. Dr. Yongsheng Zhang

Abstract

Thermoelectric generators can directly convert heat into electricity. They have received increasing attention by the materials science community and developed rapidly in the last decades. In this thesis strategies to improve the thermoelectric performance of diverse chalcogenide and half-Heusler phases are investigated.

In the first part the thermoelectric transport properties of $Cu_{3-x}Sm_xSbSe_4$ ($x \leq 0.025$) chalcogenide samples are studied in the temperature range of 300 K < T < 650 K. From density functional theory calculations, it can be concluded that through appropriate substitution the relatively lighter valence band can be activated to contribute to the transport properties. In this work, the weighted mobility is enhanced due to activating the light valence band through slight Sm substitution. In addition, in the Sm-doped samples, the lattice thermal conductivity is reduced dramatically because the Sm doping induces a stronger point-defect phonon scattering. Finally, a zT of ~1.0 at 648 K for $Cu_{3-x}Sm_xSbSe_4$ with a charge carrier concentration of 4.3×10^{18} cm^{-3} at room temperature is obtained.

In the second part, the thermoelectric transport properties of $Cu_{3-x}Sm_xSbSe_{4-y}S_y$ ($x = 0$, 0.005, 0.0075 and $y = 0$, 0.5, 0.1, 0.15) samples are studied in the temperature range of 300 K < T < 650 K. Doping and alloying can induce mass fluctuations and strain field fluctuations related to the interatomic coupling force differences between the introduced atom and the host lattice. Through the Callaway model it is demonstrated that the Sm and S co-doping induces stronger mass fluctuations and strain field fluctuations than that of the pristine sample. A large decrease in the lattice thermal conductivity is achieved due to the improved point defects, resulting in an evident improvement of the thermoelectric performance.

In the third part the thermoelectric transport properties of Cu-excess $Zr_{0.4}Hf_{0.6}NiSn$:xCu ($x \leq 0.05$) and Cu-doped $Zr_{0.4}Hf_{0.6}Ni_{1-y}Cu_ySn$ ($y \leq 0.05$) as well as Co-excess $Zr_{0.4}Hf_{0.6}NiSn$:zCo ($z \leq 0.05$) samples are investigated in the temperature range of 300 K < T < 975 K. For Co-excess samples, it is found that Co shows a negative contribution to the thermoelectric

transport properties because of the decreased electric conductivity. Compared to the Cu-doped samples, the electric resistivity is enhanced due to the increased carrier concentration, while the lattice thermal conductivity is decreased by the increased phonon scattering in the Cu-excess samples. For Cu-excess material the formation of half-Heusler (HH) / full-Heusler (FH) nanocomposites has been achieved successfully. In the Cu-excess HH / FH nanocomposites some charge carriers (electrons) of the FH nanoparticles are injected into the HH matrix, because the carrier concentration of the FH phase is much higher than that of the HH phase. At the same time, phonon scattering at the interfaces between FH nanoparticles and HH matrix is significantly enhanced, resulting in a reduced lattice thermal conductivity. The highest zT value of ~1.3 is obtained for the composition $Zr_{0.4}Hf_{0.6}NiSn:2\%Cu$ at 875 K, which is ~100 % higher than that of the pristine sample.

X

Zusammenfassung

Thermoelektrische Generatoren können Wärme direkt in elektrische Energie wandeln. Die dem zugrunde liegenden thermoelektrischen Materialien sind in den letzten Jahrzehnten vermehrt untersucht worden. Des Weiteren konnte in den vergangenen Jahren eine rasche Weiterentwicklung der Materialien und dem Verständnis ihrer physikalischen Eigenschaften beobachtet werden. Die vorliegende Arbeit beschäftigt sich mit Konzepten zur Steigerung der thermoelektrischen Leistungsfähigkeit, verschiedene Chalkogenide und intermetallische Halb-Heusler-Phasen (HH) dienen hierbei als Modellsysteme.

Im ersten Teil der Arbeit werden die relevanten thermoelektrischen Transporteigenschaften von $Cu_{3-x}Sm_xSbSe_4$ ($x \leq 0{,}025$) im Temperaturbereich 300 K < T < 650 K präsentiert. Auf Grundlage von mittels Dichtefunktionaltheorie erzielten Ergebnissen kann darauf geschlossen werden, dass eine gezielte Substitution mit Sm zur Aktivierung des so genannten schwachen Valenzbandes führt und dieses dadurch maßgeblich zu den Transporteigenschaften des Materials beiträgt. Der durch die Sm-Dotierung aktivierte Beitrag des schwachen Valenzbandes führt zu einer Verbesserung der gewichteten Ladungsträgermobilität. Zusätzlich wird für Sm-dotierte Proben eine deutlich reduzierte thermische Leitfähigkeit des Kristallgitters durch ein verstärktes Auftreten von Punktdefekten, welche die Phononen effektiv streuen können, erhalten. Daraus resultierend wurde für $Cu_{3-x}Sm_xSbSe_4$, mit einer Ladungsträgerkonzentration bei Zimmertemperatur von $4{,}3 \times 10^{18}$ cm^{-3}, ein zT-Wert von ca. 1,0 während der Temperaturerhöhung auf 648 K beobachtet.

Im zweiten Teil der Arbeit werden die Transporteigenschaften von $Cu_{3-x}Sm_xSbSe_{4-y}S_y$ (x = 0; 0,005; 0,0075 und y = 0; 0,5; 0,1; 0,15) im Temperaturbereich 300 K < T < 650 K eingehend untersucht. Dotierung und Legierungsbildung kann zu Änderungen der Massenverteilung und zur Bildung von lokalen Spannungsfelder führen. Letztere werden durch die unterschiedlichen interatomaren Bindungskräfte zwischen Wirtsgitter und den eingebrachten Atomen verursacht. Mittels des Callaway-Modells wurde gezeigt, dass die Ko-

Dotierung mit Sm und S stärkere Veränderungen der Massenverteilung und der Spannungsfelder als die Einbringung der Einzelkomponenten bewirkt. Die durch den Anstieg der Punktdefektkonzentration verursachte Reduzierung der thermischen Leitfähigkeit des Kristallgitters resultiert in einer klar nachweisbaren Steigerung der thermoelektrischen Leistungsfähigkeit des Materials.

Im letzten Teil der Arbeit wurde die Abhängigkeit der Transporteigenschaften von der Zusammensetzung von Halb-Heusler (HH) / Heusler (FH) Nanokompositen analysiert. Die Untersuchungen wurden im Temperaturbereich 300 K $< T <$ 975 K an drei Gruppen von Nanokompositen durchgeführt: i) Co-Überschuss $Zr_{0,4}Hf_{0,6}NiSn{:}z$Co ($z \leq 0{,}05$), ii) Cu-dotiert $Zr_{0,4}Hf_{0,6}Ni_{1-y}Cu_ySn$ ($y \leq 0{,}05$) und Cu-Überschuss $Zr_{0,4}Hf_{0,6}NiSn{:}x$Cu ($x \leq 0{,}05$). Im ersten Fall wurde ein negativer Einfluss von Co auf die thermoelektrischen Eigenschaften festgestellt. Im zweiten Fall wurde eine Erhöhung der Ladungsträgerkonzentration gemessen.Im dritten Fall wurde erfolgreich ein HH/FH Nanokomposit hergestellt. Dieses besitzt aufgrund der Anwesenheit der FH-Phase eine deutlich höhere Ladungsträgerkonzentration. Dies führt zu einer Injektion von Ladungsträgern (hier: Elektronen) aus der FH-Phase in die HH-Phase. Parallel wird auch in diesem Fall eine Absenkung der thermischen Leitfähigkeit beobachtet. Allerdings resultiert der Hauptbeitrag hier von der Phononenstreuung an der Grenzfläche zwischen FH-Nanopartikeln und HH-Matrix. Für die Zusammensetzung $Zr_{0,4}Hf_{0,6}NiSn{:}2\%$Cu wurde bei 875 K ein zT-Wert von ca. 1,3 gemessen. Dies stellt eine Steigerung von ~100 % gegenüber der unbehandelten Probe dar.

Chapter 1 Introduction

In this chapter I will introduce the fundamental knowledge of thermoelectricity and two important thermoelectric materials: chalcogenide and half-Heusler. First it introduces the basic fundamentals for thermoelectricity, in which the Seebeck effect and Pelter effect, figure of merit zT and strategies to increase zT are discussed. Then the two representative thermoelectric materials: chalcogenide Cu_3SbSe_4 and half-Heusler ZrNiSn are introduced and discussed.

1.1 Fundamental knowledge for thermoelectricity

The demands of large energy consumption mostly provided by the non-renewable fossil fuels are increasing with the fast development of economy and society. However, most of the industrial energy consumption is lost through waste heat. Therefore, the recovery of waste heat is very important to significantly decrease overall energy consumption. Thermoelectricity is a potential option as a result of the special property that can convert waste heat into electricity directly and reversibly.[1] Below two fundumental thermoelectric effects as well as figure of merit zT (which evaluates the performance of thermoelectric materials) will be introduced. A discussion of thermoelectricity should start with two of the most fundamental thermoelectric effects: Seebeck effect and Peltier effect.

1.1.1 Seebeck effect and Seebeck coefficient

While two different temperatures T and $T + \Delta T$ are carried out on the joint of two different materials, a voltage difference ΔV will be generated. As revealed in **Figure 1-1**, this effect (Seebeck effect) is discovered by the German physicist Thomas Johann Seebeck in around 1821.[2] The Seebeck coefficient S is shown in the following as the ratio of $\Delta V / \Delta T$:

$$S = \frac{\Delta V}{\Delta T} \tag{1-1}$$

Seebeck coefficient gives us the information of entropy per unit charge carried by electrical currents. The Seebeck coefficient is related to charge carriers (electrons and holes). In details, for intrinsic p-type or n-type materials, the motivated holes from the valence band or electrons from the conduction band will contribute to the Seebeck coefficient. When the electrons and holes coexist, the whole Seebeck coefficient is a sum of their relative contributions weighted by their contributions to the electrical conductivities (σ_n and σ_p).[3] So the Seebeck coefficient can be expressed as:

$$S = \frac{\sigma_n \cdot S_n + \sigma_p \cdot S_p}{\sigma_n + \sigma_p} \tag{1-2}$$

where σ_n and S_n are the electrical conductivity and Seebeck coefficient from electrons, σ_p and S_p the electrical conductivity and Seebeck coefficient from holes respectively.

When the electrons are dominated (n-type) in the materials, the sign of the Seebeck coefficient will be negative. When the holes are dominated (p-type), the sign of the Seebeck coefficient will be positive.
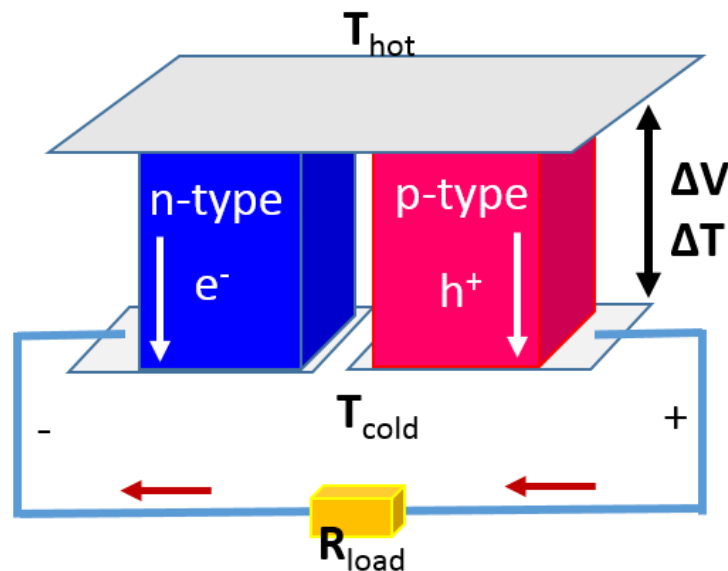
Figure 1-1. The power generation (Seebeck effect).[2]

1.1.2 Peltier effect

As shown in **Figure 1-2**, the Peltier effect is opposite to the Seebeck effect. When an electrical current flows through the joint of two different materials, the temperature gradient is created. This effect (Peltier effect) is discovered by the French physicist Jean Charles Athanase Peltier.[4]

The relation between the heat flow generated by the Peltier effect and the current can be expressed as:

$$\dot{q} = \Pi \cdot I \tag{1-3}$$

where $\dot{q}$ is the heat flow generated by the Peltier effect, Π the Peltier coefficient and I the applied current.

Peltier effect is connected with the Seebeck effect, because the Peltier coefficient Π is related to the Seebeck coefficient S by the following equation:

$$\Pi = S \cdot T \tag{1-4}$$
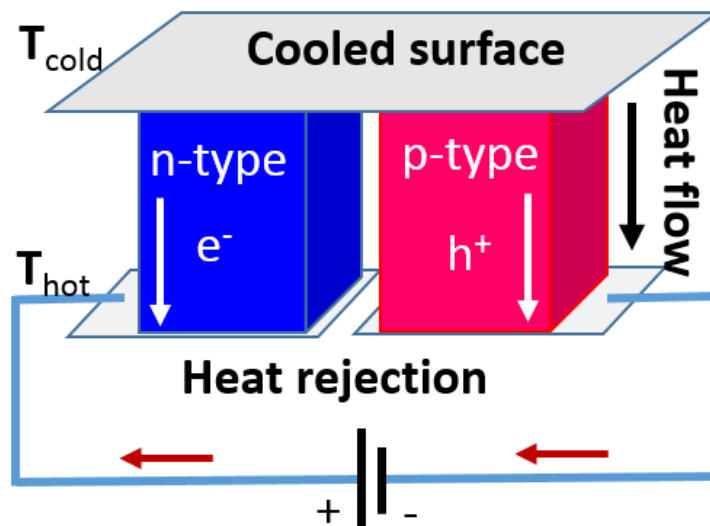
Figure 1-2. The active refrigeration (Peltier effect).[2]

3

1.1.3 Figure of merit (zT)

The conversion efficiency of a thermoelectric material is characterized by the figure of merit, zT, defined as:

$$zT = \frac{S^2}{\rho\kappa}T = \frac{S^2\sigma}{\kappa}T \qquad (1\text{-}5)$$

where S is the Seebeck coefficient, ρ the electrical resistivity, κ the total thermal conductivity, σ the electrical conductivity. The part $S^2\sigma$ is termed power factor (PF).[5]

The total thermal conductivity κ describes the heat-conducting property. For metals, the electrical carriers dominate on the heat conduction. For insulators, the lattice phonons play the main role. For semiconductors, there are two main contributions for total thermal conductivity.[6] So in a semiconductor, κ is composed of the lattice thermal conductivity κ_L and the carrier contribution κ_e: $\kappa = \kappa_L + \kappa_e$. κ_e is assessed by using the measured electrical conductivity σ through the Wiedemann-Franz relation: $\kappa_e = L\sigma T$, where L is the Lorenz number. For limit of metals and degenerate semiconductor, $L = 2.44 \cdot 10^{-8}\ \Omega\mathrm{WK}^{-2}$, while for limit of nondegenerate semiconductors, $L = 1.48 \cdot 10^{-8}\ \Omega\mathrm{WK}^{-2}$.

The total thermal conductivity is calculated by the following equation:

$$\kappa = DC_p\alpha \qquad (1\text{-}6)$$

where D is the density of the sample, C_p is the specific heat capacity, and α is the thermal diffusivity.[7]

Normally we can get the C_p through Dulong-Petit law. Dulong-Petit law means that the solids have the same molar heat capacity:

$$C_\text{p} = 3R \tag{1-7}$$

where R means the universal gas constant.

The Dulong-Petit law considers the degrees of freedom of the vibration of the atoms. According to the equipartition law, if an atom vibrates around the equilibrium position, each degree of freedom will possess an energy of $k_\text{B}T$, where k_B is the Boltzmann constant. As each atom will vibrate in three dimensions, so each atom will have an energy of $3k_\text{B}\text{T}$. The inner energy U of the system equals the averaged energy of each atom multiplies the number of atoms. One mole of atoms equals Avogadro's constant N_A. Molar heat capacity $C_{V,\text{m}}$ equals partial differentiation of inner energy U with respect to T given by the following equation:

$$C_{\text{p,m}} \approx C_{V,\text{m}} = (\tfrac{\partial U}{\partial T})_V \approx 3N_\text{A}k_\text{B} = 3R \tag{1-8}$$

The specific heat capacity is the heat capacity correlated to the mass of the material. Hence, specific heat capacity can be calculated using the following equation:

$$C_{\text{p,m}} = \frac{3NR}{M} \tag{1-9}$$

where N is the number of atoms in one formula unit of the compound and M is the molar mass.

This approximation is called classical theory and the classical theory is valid at high temperature range. At low temperatures the measured heat capacities will deviate from Dulong-Petit law and then the Debye model is suitable.

The Carnot efficiency can be used to describe the conversion efficiency of the TE device as well.[8] The maximum conversion efficiency η_{max} is calculated by the following equation:

$$\eta_{max} = \frac{T_H - T_C}{T_H}\left(\frac{\sqrt{1+zT_m}-1}{\sqrt{1+zT_m}+\frac{T_C}{T_H}}\right) = \eta_C\left(\frac{\sqrt{1+zT_m}-1}{\sqrt{1+zT_m}+\frac{T_C}{T_H}}\right) \tag{1-10}$$

where T_H is the temperature of the hot side, T_C the temperature of cold side, η_C is the Carnot efficiency and T_m the mean temperature.

Figure 1-3 shows the maximum TE conversion efficiency η as a function of the temperature gradient and figure of merit zT at the clod side temperature $T_C = 300$ K. When temperature difference is fixed, thermoelectric device with higher zT materials will possess higher conversion efficiency. Therefore, it is of importance to enhance zT values of thermoelectric materials. In next section strategies of improving zT will be introduced and discussed.
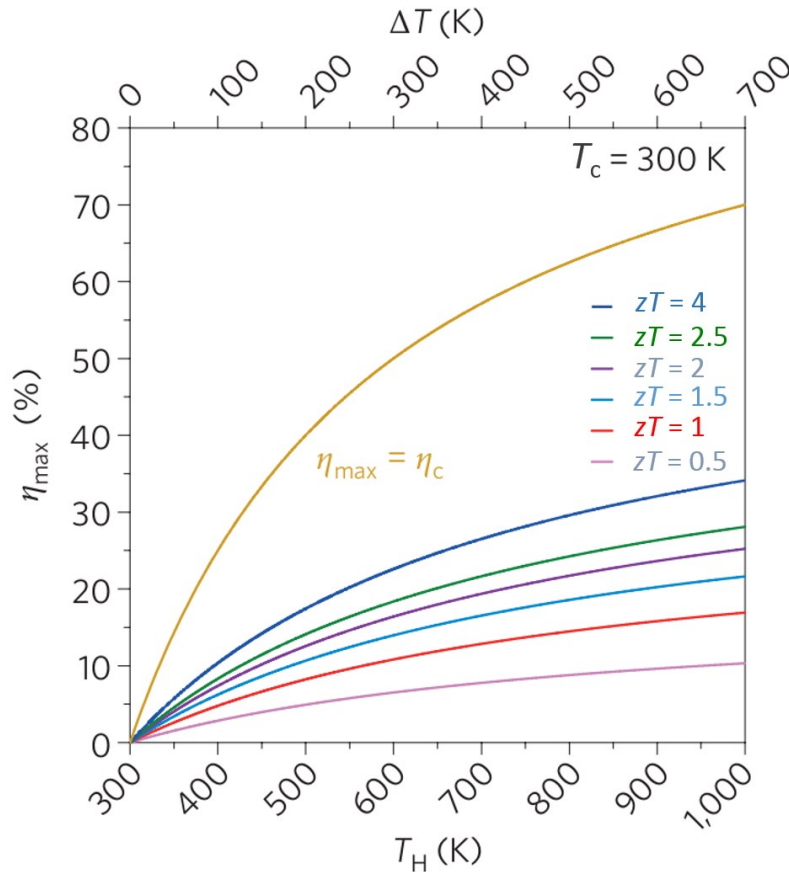
Figure 1-3. The maximum TE conversion efficiency η as a function of the temperature gradient and figure of merit zT at the clod side temperature $T_C = 300$ K.[9]

1.2 Strategies to increase zT

As discussed in last section (1.1.3), zT is a combination of four physical parameters (S, ρ, κ and T). Since three fundamental parameters (S, ρ, κ) are interrelated to each other, it is not so straightforward to enhance zT by simply optimizing one of S, ρ and κ. Anyway, in order to simplify the question, the approaches of optimizing individual three fundamental parameters (S, ρ, κ) will be discussed separately. In most cases, zT enhancement normally results from combined strategies which optimize two of [S (or ρ), κ] or all of [S, ρ, κ].

1.2.1 Strategies to decrease resistivity

The electrical conductivity can be calculated by the following equation:

$$\sigma = \frac{1}{\rho} = ne\mu \qquad (1\text{-}11)$$

where n is carrier concentration, e the elementary charge, and μ the carrier mobility. In order to decrease ρ or enhance σ, carrier concentration and/or carrier mobility should be increased.

1.2.1.1 Optimizing carrier concentration

Optimizing the carrier concentration is still one of the most effective methods to improve thermoelectric properties of most TE materials.[10] Generally, the optimum carrier concentration for good TE materials is in the range of 10^{19} to 10^{21} cm^{-3}. Normally, there are two different approaches to tune carrier concentration, *i.e.*, substitution and introducing point defects.

(1) Substitution:

Extrinsic substitution is a conventional approach to adjust the carrier concentration.[11] Normally, the method is achieved by filling some guest atoms in a caged structure or alloying

with elements from the nearby columns in the element periodic table.[12] According to the types of charge carriers (n-type or p-type), the elements (left column or right column) will be chosen.

Although the method looks simple, choosing a suitable dopant is not so easy in fact. The reason why some higher TE performances theoretically predicted have not been realized in the experiments is that the optimum carrier concentration cannot be achieved due to the solubility limit.[13] In some materials containing two or more elements, there should be two or more element solubility limits.[14] For example, in $CoSb_3$ skutterudite, the research of the solubility of the different dopant atoms is confusing due to it has two solubility limits depending on whether it is Co-rich or Sb-rich in this material.[15]

(2) Point defects:

Introducing point defects can tune the carrier concentration as well, including interstitials, vacancies and antisites.[16] The types and concentrations of these intrinsic point defects are very sensitive to the composition of the materials. In principle, a smaller difference of covalent radius and the electronegativity between the cation and the anion leads to a smaller formation energy of the cation antisite defects.[17, 18]

For example, in the p-type $Bi_{2-x}Sb_xTe_3$, difference in covalent radius and electronegativity between Sb and Te is smaller than that between Bi and Te. So the formation energy of antisite defects will be reduced and thus carrier concentration will be increased with the increasing Sb content.[18-20]

1.2.1.2 Improving carrier mobility

A high carrier mobility is required for a good electric conductivity and thermoelectric performance as well. In a semiconductor, the carrier mobility is related to the electronic structure and the different scattering mechanisms, including acoustic phonon scattering, ionized impurity scattering and grain boundary scattering, *etc.*[21]

When there are several different parallel carrier scattering mechanisms, their contributions could be expressed in the Matthiessen's rule,[22] in which the combined relaxation time τ_C can be obtained by the addition of the inverse relaxation times for the different scattering processes, $\tau_c^{-1} = \Sigma\ \tau_i^{-1}$, in which τ_i means the phonon relaxation time of the ith scattering process.[23]

(1) Acoustic phonon scattering:

Normally, above room temperature acoustic phonon scattering is dominant among the different scattering mechanisms in the thermoelectric materials. The scattering of carriers and the perturbation of the energy bands is caused by the local strain when an acoustic phonon wave goes through the lattice in the crystal. The process is deformation potential scattering from acoustic phonons, in which deformation potential is used to describe the coupling strength between carriers–phonons.[24] Normally different deformation potential coefficients can affect the carrier mobility greatly.

According to the single parabolic band (SPB) model,[25] the acoustic phonon scattering carrier mobility is expressed as:

$$\mu_{ac} \sim \frac{C_l}{m_I^* m_b^{*3/2} \varXi^2 T^{3/2}} \tag{1-12}$$

where C_l is the average longitudinal elastic modulus, m_I^* is the transport effective mass along the direction of the conduction, m_b^* is single-valley density of states effective mass and $\varXi$ is the deformation potential. So if we want to have a high carrier mobility, the materials should have a large C_l and small m_I^*, m_b^* and $\varXi$.

(2) Ionized impurity scattering:

In most heavily doped TE materials, the carrier concentration is in the range of 10^{19} to 10^{21} cm^{-3}. So in the heavily doped semiconductors with high carrier concentrations, the ionized impurity atoms in the lattice can provide scattering centers for charge carriers. To improve

the carrier mobility, modulation doping is proposed to solve the problem. Modulation doping can be achieved by embedding a heavily doped minor secondary phase into the pristine matrix. The charge carriers in the minor secondary phase can be separated from their parent grains and moved into the pristine matrix. In such case, the carrier mobility will increase because of the reduced carrier scattering around the ionized impurities.

Chen and Ren *et al.* successfully demonstrate this strategy by inserting some heavily doped silicon nanograins into the pristine SiGe matrix.[26, 27] The schematic diagram illustrating the modulation doping is shown in **Figure 1-4**. They embed heavily doped silicon nanograins into an undoped SiGe host matrix. The carrier concentration of silicon nanograins will be separated from their parent grains and inject into the pristine matrix. The reduced carrier scattering around the ionized impurities leads to increased carrier mobility. In their experiment, a large improvement in power factor as well as *zT* value has been achieved.
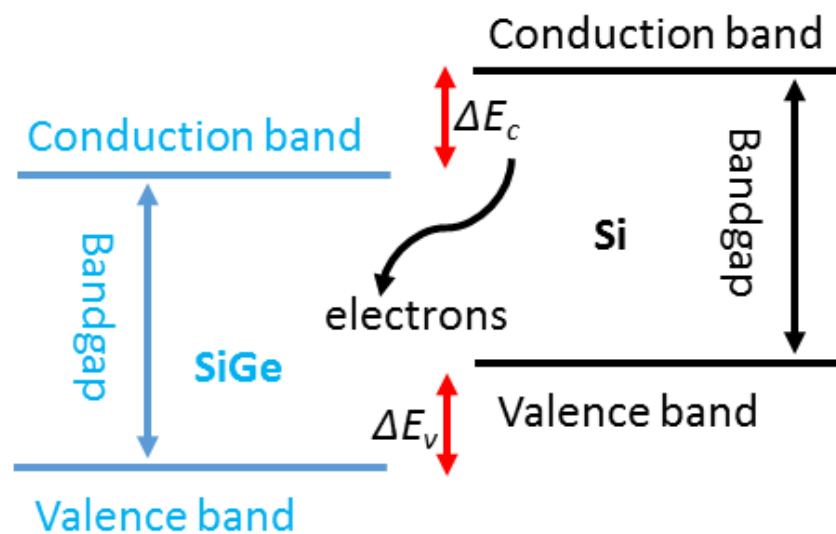
Figure 1-4. A schematic diagram illustrating the modulation doping.

(3) Grain-boundary scattering:

In nanostructured materials, when the grain size is comparable to the electron mean free path, grain-boundary scattering will be noticeable.[28] In the single-crystal, the anisotropy of

carrier mobility is generally strong, while the anisotropy of carrier mobility is generally weak because of the random orientation of the grains in polycrystalline samples. In order to have a good carrier mobility, we need to reduce the impact of different grain boundaries on the transport, especially in polycrystalline anisotropic structure samples.[29] Reconstructing the random grain boundaries in the polycrystal to somewhat-ordered structure could be an effective strategy.

One approach is the mechanical alignment of the grains through uniaxial compression during the synthesis, such as hot press and spark plasma sintering.[30, 31] For example, in both n-type $Bi_2Te_{2.1}Se_{0.9}$ and p-type $Bi_{0.4}Sb_{1.6}Te_3$ samples prepared through SPS, an obvious electrical conductivity anisotropy is observed, which means the existence of texture.

In textured $Bi_{0.875}Ba_{0.125}CuSeO$ obtained through a hot-forging process, Sui *et al.* achieve a high *zT*.[32] The carrier mobility along the direction perpendicular to the pressing direction is increased greatly. Because of the increase in carrier mobility, the electrical conductivity and the power factor are increased.

In their experiment, the whole synthesis processing of the samples including four steps is shown in **Figure 1-5**, so the as-synthesized, the first hot-forged, the second hot-forged and the third hot-forged samples with textured microstructures are named as 0T, 1T, 2T and 3T, respectively. First the mixed raw powders are put in a graphite die followed by cold pressing and heating at 1023 K to get the as-synthesized bulks (**Figure 1-5a**). Then the as-synthesized bulks are ground into powders and sintered by hot press under the 80 MPa stress at 973 K to get cylinder-shaped samples (**Figure 1-5b**). The cylinder-shaped samples are cut and followed by second times and third times hot-forging in larger dies to get the textured bulks as shown in **Figures 1-5c** and **d**.
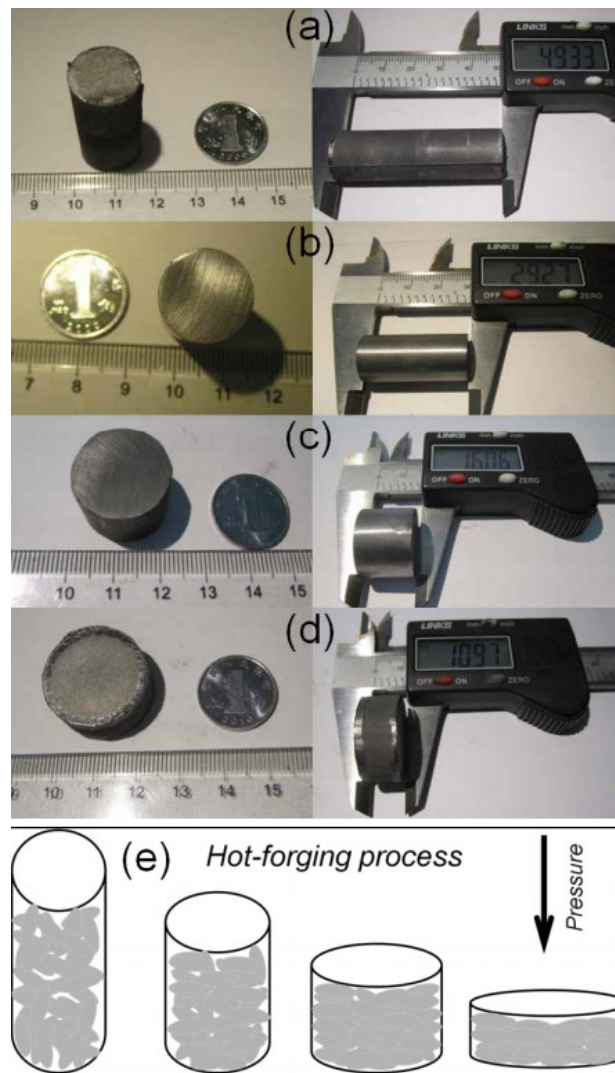
Figure 1-5. Typical samples used in the reference: (a) As-synthesized sample (0T); (b) One step hot-forged sample (1T); (c) Two steps hot-forged sample (2T); (d) Three steps hot-forged sample (3T); (e) The scheme of hot-forging process.

1.2.2 Strategies to increase Seebeck coefficient

Recently some unique physical mechanisms related to band structure engineering have been proposed and experimentally achieved in thermoelectric research, such as energy filtering in PbTe-based nanocomposites embedded with Pb nanoparticles[33, 34], distortion of the electronic density of states (resonant energy level) in Tl doped PbTe[35], and band convergence[36-38].

12

1.2.2.1 Through energy filtering to enhance thermoelectric performance

Normally potential barriers formed at grain boundaries and interfaces can negatively affect the carrier mobility, but they are possible to play a positive role through enhanced energy filtering effect (EFE) in thermoelectric materials as well.[39-44] EFE is an additional scattering mechanism introduced through preferentially scattering low energy electrons, as illustrated in **Figure 1-6**.[45] In **Figure 1-6**, the Seebeck coefficient is proportional to the integral of the calculated Seebeck distribution versus energy for heavily doped $Si_{80}Ge_{20}$ curve. Actually low energy electrons will reduce the thermopower because this portion of the Seebeck distribution is negative. In a nanocomposite system, the obvious scattering mechanism is grain boundary scattering and interface scattering, which can reduce the carrier mobility and preferentially scatters carriers with energies lower than the barrier height.[46] EFE is a good example of how nanostructured materials can be used to improve electrical transport properties while still maintaining good thermal transport properties.[47-50]
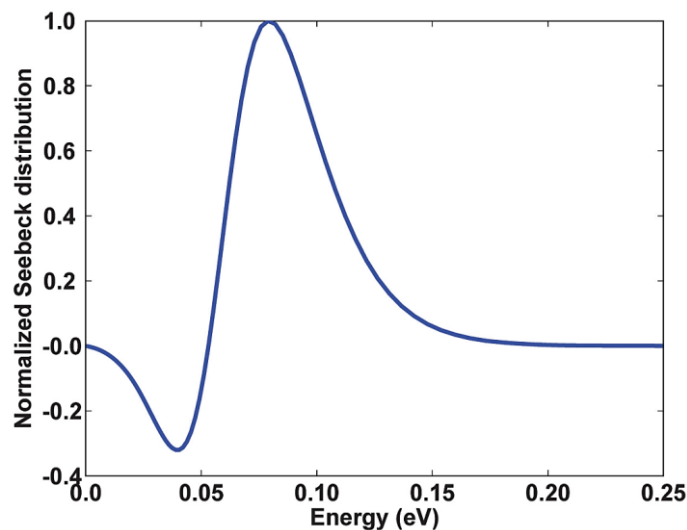
Figure 1-6. Calculated normalized Seebeck distribution versus energy for heavily doped bulk n-type $Si_{80}Ge_{20}$. [45]

In metal-based InGaAs / InGaAlAs superlattices, Daryoosh Vashaee and Ali Shakouri's work shows that metal-based superlattices with tall barriers can achieve a large zT (>5) at room temperature in a detailed calculation.[51] Faleev and Leonard use perturbation theory

and partial wave method to investigate PbTe based composites dispersed with Pb nanoparticles, and they assume that the electron scattering on spherically symmetrical interface potentials is independent of other scattering mechanisms. The calculated thermopower of PbTe-Pb nanocomposite is larger than that of bulk PbTe matrix.[52]

1.2.2.2 Through resonant levels to enhance the density of electrical states

The Mott equation describes a relationship between the Seebeck coefficient and the carrier properties, and is defined as:

$$S = \frac{\pi^2 k_{\mathrm{B}}^2 T}{3q} \left[\frac{\partial \ln(\sigma(E))}{\partial E} \right]_{E=E_{\mathrm{f}}}$$

$$= \frac{\pi^2 k_{\mathrm{B}}^2 T}{3q} \left[\frac{1}{p} \frac{\partial p(E)}{\partial E} + \frac{1}{\mu} \frac{\partial \mu(E)}{\partial E} \right]_{E=E_{\mathrm{f}}} \tag{1-13}$$

with carrier mobility $\mu(E) = q\tau/m^*$, where q the carrier charge, $p(E)$ and $\mu(E)$ energy dependence of carrier density and mobility, m^* the effective mass and E_{f} is the Fermi energy. From the equation, one approach to enhance the Seebeck coefficient is the introduction of resonant distortion of electrical density of states near the Fermi level (E_{f}) reflected by increased effective mass m^*.

Introducing impurity band energy levels to increase the thermopower has resulted in an obvious increase in zT.[35, 53] Previously resonant impurity is a concept introduced in solid state physics for metals. [54-56]

Theoretically Hicks[57] and Mahan[58] predict enhancements in thermoelectric properties due to an increase in the electronic density of states first. The resonant level can be regarded as a bound level with an energy that falls above the conduction band edge or below the valence band edge,[59] creating a local maximum in the electronic density of states, as shown in **Figure 1-7**. The figure represents schematically the case for In:PbTe, where the resonant states are in the conduction band. Band structure calculations show not only impurities create

sharp DOS peaks close to the Fermi level, but also those peaks should be of the similar character as the host band structure. Results show that d- or even f-state impurities are useful to improve the thermopower of metals, but s-or p-state resonance levels are more suited to improve thermoelectric properties of semiconductors.[60-62]
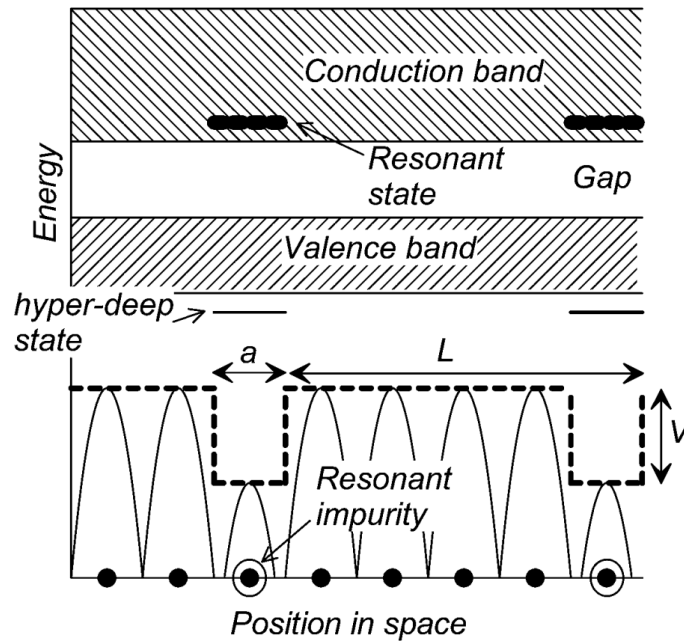
Figure 1-7. Schematic energy versus distance diagram where the spheres on the bottom represent atoms. The periodic potential of the host atoms of the solid is experienced by conduction electrons and results in the formation of conduction and valence bands, extended states available to the nearly-free electrons. [59]

1.2.3 Strategies to reduce lattice thermal conductivity

In a semiconductor as discussed above, normally κ is composed of the lattice thermal conductivity κ_L and the carrier contribution κ_e: $\kappa = \kappa_L + \kappa_e$. To get high TE performance, it is important to explore different strategies to suppress the κ_L. The most popular method is the introduction of the multiscale scattering centers to increase the phonon scattering, as listed in **Table 1-1**.[63]

Table 1-1. Different strategies to scatter different wavelength phonons.

	Short wavelength phonons	Medium wavelength phonons	Long wavelength phonons
point defects	√	✗	✗
nanostructuring	√	√	✗
dislocations	✗	√	✗
grain boundaries	✗	✗	√

The lattice thermal conductivity can be estimated by the Matthiessen's rule. According to the Matthiessen's rule, the combined relaxation time is attained by the addition of the inverse relaxation times for the different scattering processes. Normally the inverse relaxation time is proportional to the frequencies of the specific phonon scattering modes. So lattice thermal conductivity κ_L is related to different phonons scattering modes and frequencies. So to reduce the κ_L we need to suppress the transmission of phonons with various frequencies.[64] As shown in **Figure 1-8**, to reduce the κ_L, it is possible to introduce simultaneously all-scale hierarchical scattering centers into the host, including point defects, nanoscale grain boundaries and precipitates, dislocations.[65, 66]

In scattering of short wavelength phonons, the contributions from point defects are quite important. Point defects include vacancies, interstitials, antisites and alloying.[67, 68]

However, the disadvantage of point defects scattering is that the point defects may scatter the carriers as well, which decreases the mobility.

In scattering of short to medium wavelength phonons, nanostructure engineering is employed normally.[69] Up to now, the most successful nanostructure engineering method in TE research is that the increased grain boundaries or the formed nanoscale precipitates. Ball-milling and melting-spinning are two typical technologies to fabricate nanoscale powders.[70] Forming nanoscale precipitates in the matrix materials is the effective nanostructuring strategy to reduce the κ_L as well.

In scattering of medium wavelength phonons, dislocations are effective to reduce the κ_L, and may be formed by deliberate plastic deformation of the samples during the fabrication process of TE materials.[71, 72] Kim *et al.* report that a large decrease in κ_L of the $Bi_{0.5}Sb_{1.5}Te_3$ because of the dense dislocation arrays formed at the ordered boundaries of nanograins in the matrix through liquid-phase sintering.[73]
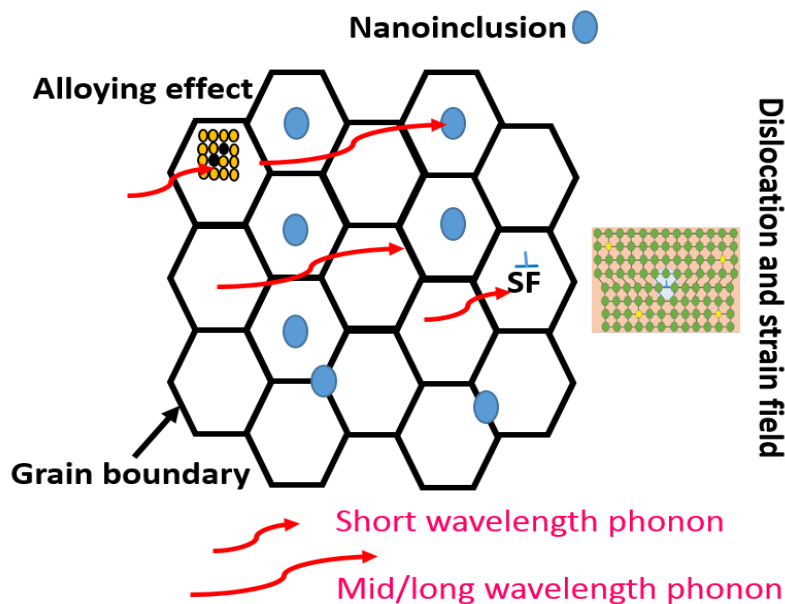
Figure 1-8. A schematic diagram illustrating the various phonon scattering mechanisms.[66]

1.3 Cu₃SbSe₄ chalcogenide and ZrNiSn half-Heusler

As discussed above, the transport properties are the key criterion to choose a good thermoelectric candidate. The transport properties are related to the crystal structure directly. By reviewing the relation between structures and properties of all existing thermoelectric materials, it can be found that materials with diamond-like structure can achieve the tradeoff between the scattering of electrons and phonons. Thus it is possible to find a diamond-like structured TE material with good electric transport properties and thermal transport properties at the same time. Besides, a good thermoelectric material normally has low thermal conductivity and charge carrier concentration of $10^{19} \sim 10^{21}$ cm^{-3} which ensures a high power factor ($S^2\sigma$). Tritt[6] did a hypothetical calculation to show that a corresponding minimum S should be fulfilled to achieve a certain zT value. In his calculation, assumed the $\kappa_L = 0$, the material would require $S = 157$ μVK^{-1} for $zT = 1$ and $S = 225$ μVK^{-1} for $zT = 2$. Of course the assumption is over simplified and real material will need to have higher S to achieve the projected zT values. However, it at least emphasizes that high Seebeck coefficient is crucial to achieve high zT. According to the references,[74-76] Cu₃SbSe₄ chalcogenide and ZrNiSn half-Heusler (HH) are two good candidates with high Seebeck coefficient among the diamond-like structure thermoelectrics. Therefore, Cu₃SbSe₄ chalcogenide and half-Heusler are chosen as the investigated subjects in this thesis, and their crystal structures will be introduced below.

1.3.1 Cu₃SbSe₄ chalcogenide

In chalcogenide Cu₃SbSe₄, the atomic configurations $3d^{10}4s^1$ for Cu, $5s^25p^3$ for Sb, and $4s^24p^4$ for Se atoms are treated as the valence electrons. According to atomic electronegativities, Cu is the more electropositive element while Se is more electronegative. For the valence electrons, Cu will lose one valence electron to form Cu$^+$, and Se will gain two valence electrons to form Se^{2-} ionic states. Sb is a group-V element, so Sb will lose electrons from the outermost p state to form Sb^{3+} valence state or lose electrons from p and s states to

form Sb^{5+} valence state. In Cu_3SbSe_4, to keep the balance of the charges, Sb should be Sb^{5+} valence state instead of Sb^{3+} valence state.[77]
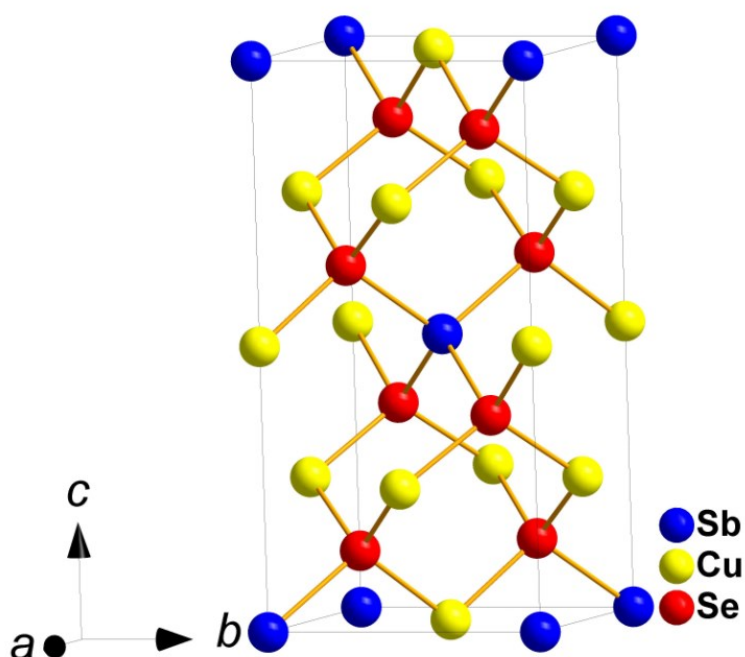
Figure 1-9. The crystal structure of Cu_3SbSe_4.

The crystal structure of the compound is shown in **Figure 1-9**. The tetragonal crystal structure of Cu_3SbSe_4 is lower in symmetry compared to the cubic system, and its electron band structure near the Fermi level is dominated by the *s* states of Sb and *p* states of Se.[77] The material has a low lattice thermal conductivity and large Seebeck coefficient due to the distorted diamond-like structure. In the crystal structure, there are the Cu / Se framework and the tetrahedral $SbSe_4$. The one-dimensional array of the $SbSe_4$ tetrahedra is inserted into the three-dimensional Cu / Se framework. There are two inequivalent Cu atoms (two different Wyckoff sites) in the crystal structure, and both each Cu and Sb atom has four Se nearest neighbors.

In the structure, it has distorted $CuSe_4$ tetrahedra and slightly flattened $SbSe_4$ tetrahedra. The bond lengths of Sb-Se are larger than that of Cu-Se bonds, so the diamond-like tetrahedral structure is distorted by the insertion of $SbSe_4$. For two inequivalent Cu atoms, the bond

19

lengths of Cu-Se are different as well. This difference of Cu-Se bonding increases the anisotropy of electronic and phonon scattering. The Cu / Se framework is the main pathway for the hole conduction. Normally through substitution the electrical conductivity can be tuned in the Cu / Se framework.[74]

Currently, the most interest and attentions have been focused on tuning carrier concentration of Cu_3SbSe_4 by substitution of Sb and Se sites. For example, Sb is substituted by Ge[78], Al[79], Sn[80], Bi[81] and In[82] to enhance the carrier concentration and thermoelectric performance. However, it has been rarely reported to enhance TE performance of Cu_3SbSe_4 via Cu-site substitution. To the best of our knowledge, the only one reported work of Cu-site substitution is Zn substitution[83], but unfortunately compared with the unsubstituted Cu_3SbSe_4 the carrier concentration of Zn substituted Cu_3SbSe_4 is decreased and the TE performance becomes worse. The representative reported experimental results are summarized in **Figure 1-10**. [74, 78-83]
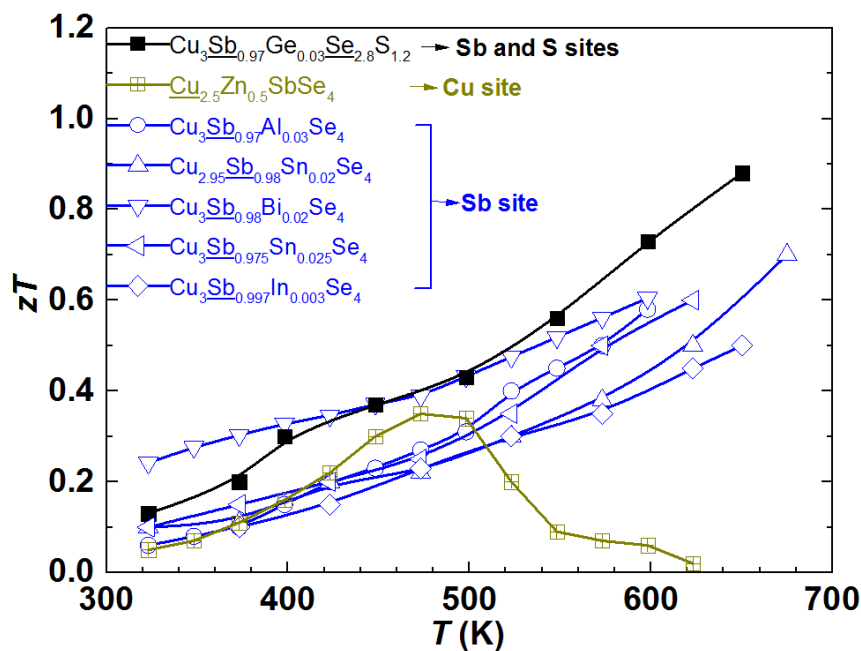
Figure 1-10. Temperature dependence of figure of merit zT of different element-doped Cu_3SbSe_4.

In the most reported references, the enhancement of electrical conductivity through the increase of carrier concentration is the key to enhance TE performance. Is it possible to improve the performance via increasing the carrier mobility? According to the reference, the valence band of Cu_3SbSe_4 is degenerated shown in **Figure 1-11**.[84] **Figure 1-11** is the band structure of Cu_3SbSe_4 in body center tetragonal primitive unit cell (8 atoms / cell). From the figure we see that it is a direct-band semiconductor and the valence band is degenerated in the Γ point. Normally transport properties of Cu_3SbSe_4 material are very well characterized within a single parabolic band (SPB) model and are dominated by the relatively heavy valence band.[80] Besides the heavy valence band, there are two more light valence bands at the Γ point. If the relatively light valence band can be activated via substitution to contribute the transport properties as well, it will be highly possible to enhance the carrier mobility.
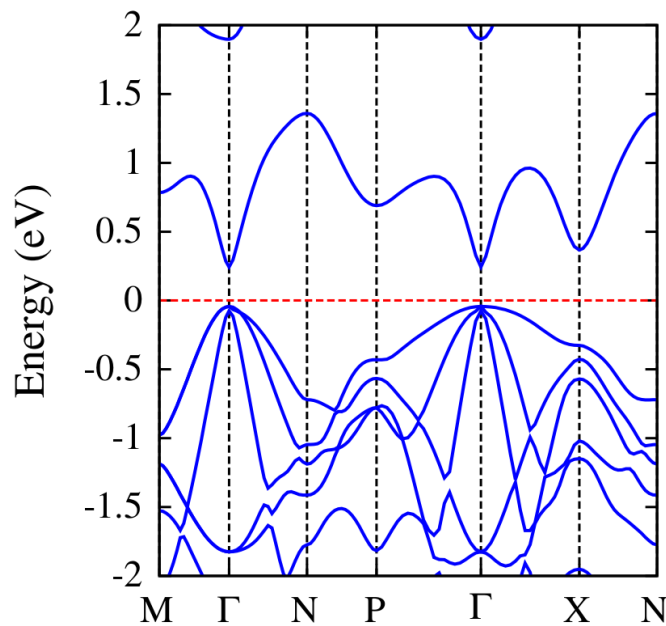
Figure 1-11. Band structure of Cu_3SbSe_4 in body center tetragonal primitive unit cell (8 atoms / cell).

1.3.2 ZrNiSn half-Heusler

The half-Heusler phase is characterized by the formula *XYZ* while the full-Heusler phase has the formula *XY₂Z*. For half-Heusler, *X* is usually a transition metal, *Y* is a transition metal,

while *Z* is a main-group element of group 14 or 15, most frequently the *sp* metalloid (Sb) or metal (Sn).[85]
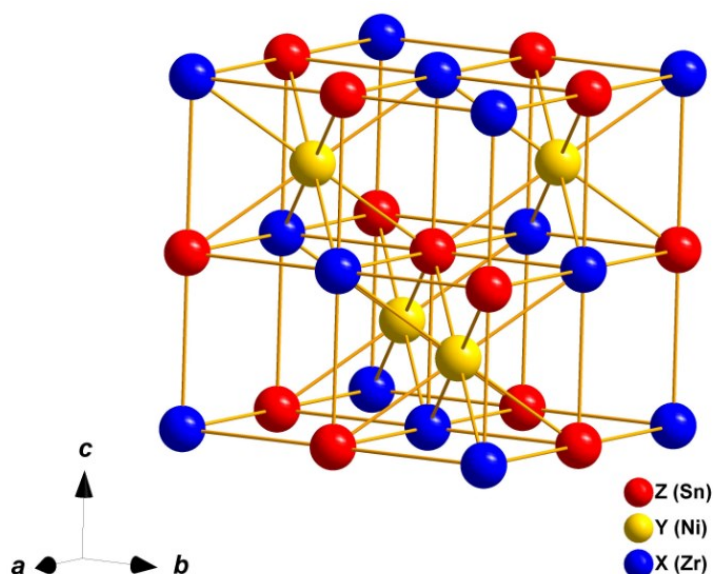
Figure 1-12. Crystal structure of *XYZ* (ZrNiSn) half-Heusler compounds.

Figure 1-12 shows crystal structure of *XYZ* (ZrNiSn) half-Heusler compounds. We can regard half-Heusler as a kind of stuffed diamond-like structure.[86] In this model *Y* and *Z* will form a diamond-like lattice (*i.e.*, the zinc blende lattice). In other degree, *X* and *Z* can form a rock salt structure and in this model *Y* will locate at one of the two body diagonal positions, leaving the other one in unoccupied state in the cell. In the structure, it will have one vacant face-centered cubic sublattice and three filled interpenetrating face-centered cubic sublattices.

We can treat *XYZ* half-Heuslers as an X^{n+} ion stuffing a zinc blende $(YZ)^{n-}$ sublattice. According to the Zintl–Klemm concept,[87] *X* is the most electropositive element while *Y* and *Z* are more electronegative. *X* will donate the valence electrons to *Y* and *Z*. So we can describe half-Heusler as $X^{n+}(YZ)^{n-}$. Zintl-anion framework is formed by the (*YZ*) covalent tetrahedrally bonded diamond-like sublattice. The electropositive X^{n+} occupies the octahedral vacancies around the tetrahedral framework. In this model, the number of valence electrons is 18.[88]
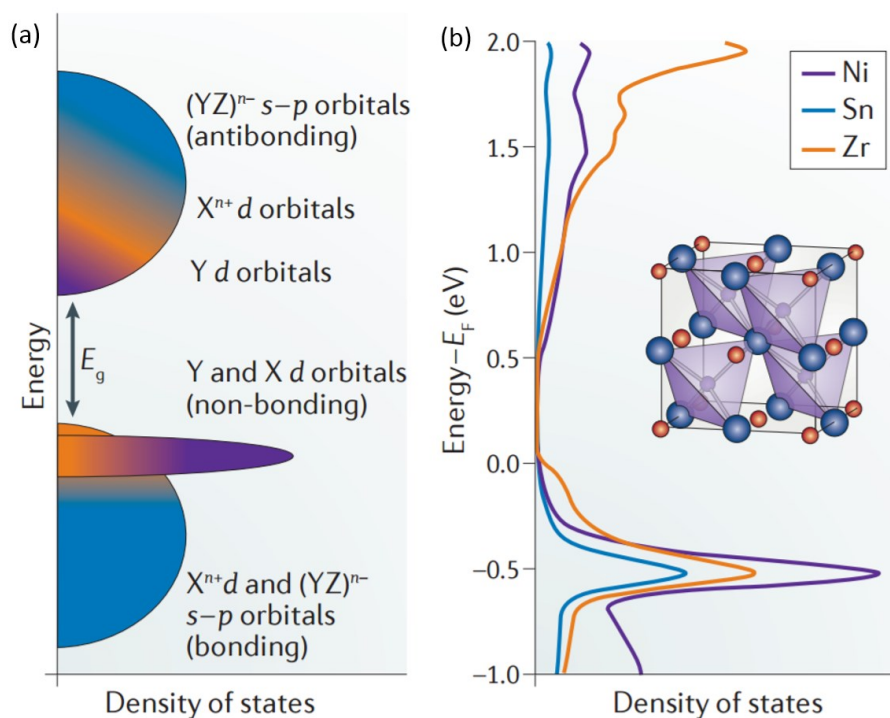
Figure 1-13. The schematic formation of the density of states in $X^{n+}(YZ)^{n-}$. The s–p bonding orbitals of the tetrahedrally (sp^3 hybridized) coordinated Zintl-anion framework form the lower energy valence band (blue) with the X^{n+} cation contribution in the valence band edge (orange), because of the X^{n+} d-orbital interaction with the $(YZ)^{n-}$ framework. (b) The calculated partial density of states of ZrNiSn, showing the different elemental contributions. E_F is Fermi energy.[89]

   Figure 1-13a is the schematic formation of the density of states in $X^{n+}(YZ)^{n-}$. In this figure, the purple line part is the localized, non-bonding d orbitals of Y, which forms the flat and heavy valence band. Y d band has the influence on valence band states of holes. This leads to a better performance in n-type material compared with the p-type material.[90-92] Because there is a larger overlap of the bonding s and p orbitals, flat Y d orbitals are not at the valence band edge. The interaction of X element d-orbital and the $(YZ)^{n-}$ bonding orbitals form the valence band edge.

   In the case of ZrNiSn, Zr^{4+} d orbitals and Ni d orbitals form the conduction band. Because Zr^{4+} has the higher electropositivity, the atomic orbitals of Zr^{4+} are higher. Although filled d orbitals show mostly Ni-like character, there is some Zr^{4+} contribution.[93] **Figure 1-13b**

shows the calculated partial density of states. From the picture, we see the filled d orbitals are the interaction of the Zr^{4+} and Ni d orbitals.
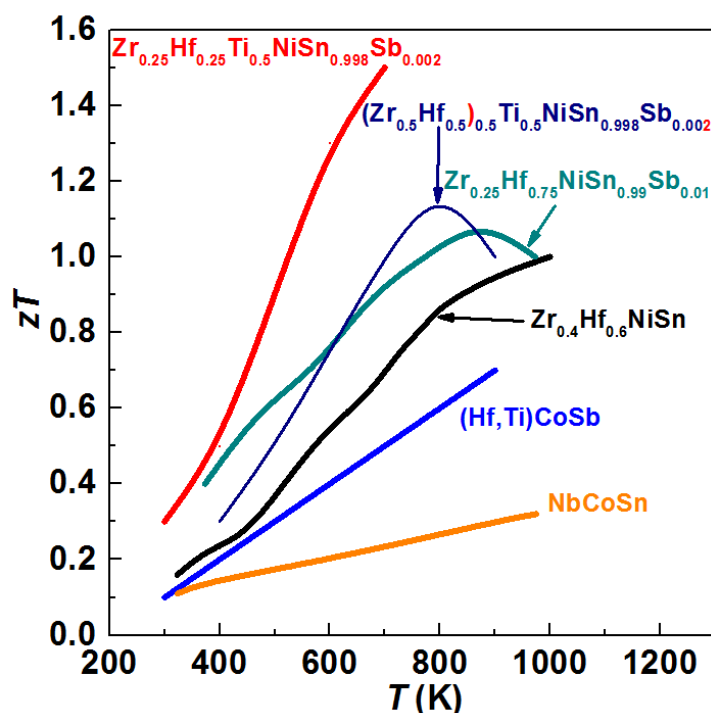
Figure 1-14. Temperature dependence of record values of the figure of merit zT for some n-type half-Heusler compounds.

HH compounds have attracted attentions as a promising candidate material for high temperature thermoelectric applications. Normally, the 18-valence electrons HH systems have a high effective mass and a large Seebeck coefficient. For instance, at room temperature the Seebeck coefficient of n-type HH compounds ZrNiSn and HfNiSn are in the range of $-200\ \mu V/K$ to $-400\ \mu V/K$.[76] In theory, more than 30 different half-Heusler materials have been studied by ab initio calculations.[94, 95] In experiment, several half-Heusler compounds[96-98] have been investigated to improve the thermoelectric properties, among them ZrNiSn is the most intensively investigated one. **Figure 1-14** shows temperature dependence of record values the figure of merit zT for some n-type half-Heusler compounds.[99-104] One of the highest figures of merit ($zT = 1.5$ at 700 K) is reported by Sakurada and Shutoh in n-type $(Zr_{0.5}Hf_{0.5})_{0.5}Ti_{0.5}NiSn_{1-y}Sb_y$ sample.[99] Although attempts to

24

reproduce the result failed, their work encourages more and more researchers to investigate the thermoelectric transport properties of ZrNiSn-based half-Heusler compounds.
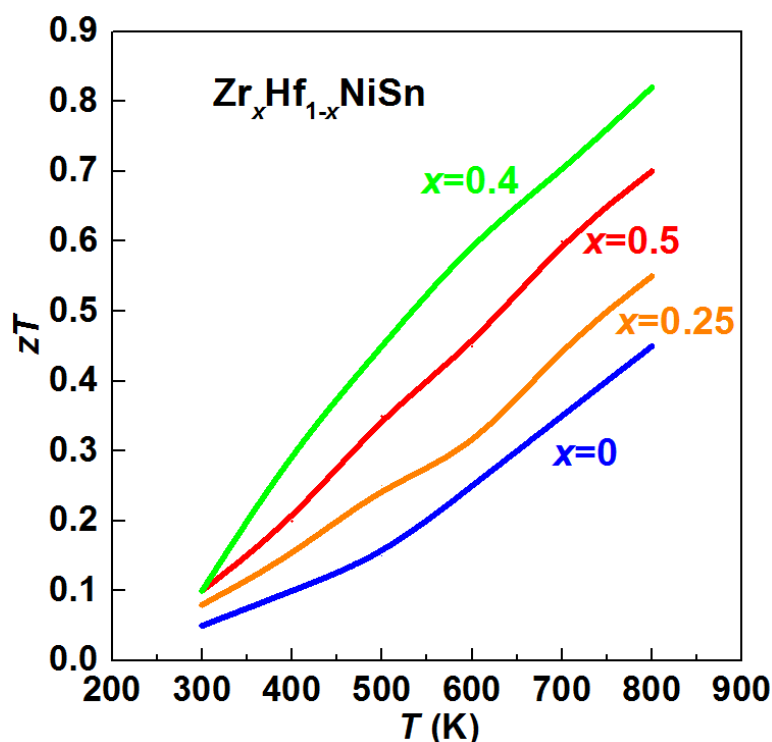
Figure 1-15. Temperature dependence of figure of merit zT for $Zr_xHf_{1-x}NiSn$ samples with $x = 0, 0.25,$ 0.40 and 0.50.[100]

Alloying different elements at the transition-metal sites of half-Heusler can decrease the lattice thermal conductivity by induced mass differences and strain fluctuations. One effective approach is using isoelectronic Hf to substitute Zr. According to the reference,[100] in $Zr_xHf_{1-x}NiSn$ samples with $x = 0, 0.25, 0.40$ and 0.50, $Zr_{0.4}Hf_{0.6}NiSn$ has the best thermoelectric performance, as shown in **Figure 1-15**. So in this thesis, we choose $Zr_{0.4}Hf_{0.6}NiSn$ as our investigated goal.

The disadvantage for the HH compounds is the relatively high thermal conductivity. Therefore, over last decades, the main research efforts have focused on methods to decrease the thermal conductivity. Recently, Makongo *et al.*[105] and Chai *et al.*[106, 107] use excess Ni in the Ni site to form the half Heusler / full Heusler (HH / FH) compounds, resulting in

improving the thermoelectric performance. In the periodic table Co, Cu and Ni are in the adjacent column and same rows. In consideration of the above results, we expect that excess Cu and Co may offer similar functions as excess Ni did in half-Heusler.

1.4 The organization of this thesis

In this thesis, all discussions are focused on two types of thermoelectrics: chalcogenide Cu_3SbSe_4 and half-Heusler $Zr_{0.4}Hf_{0.6}NiSn$. The thesis is organized as follows:

In chapter 2, major experimental is introduced in details, including sample synthesis of Cu_3SbSe_4 chalcogenide and $Zr_{0.4}Hf_{0.6}NiSn$ half-Heusler, characterization methods, apparatus used in the experiment and their measurement principles.

For Cu_3SbSe_4 chalcogenide, as discussed above Cu / Se framework is the main pathway for the hole conduction. Sm is the rare earth metal and has the *f*-electron delocalization.[108] So we choose Sm as the dopant in the Cu site and expect that Sm may engage the light valence band to achieve an enhanced mobility and higher *ZT* values. So we design the experiment $Cu_{3-x}Sm_xSbSe_4$ ($x = 0$, 0.0025, 0.005, 0.0075, 0.01 and 0.025) presented in chapter 3.

In chapter 3, through Sm substitution the electronic transport properties of Cu_3SbSe_4 are improved and we notice that there is still same space to decrease the lattice thermal conductivity. According to the reference, experimental results from Skong *et al.* [78, 109] indicate that the transport properties (shown by the black line in **Figure 1-10**) of Cu_3SbSe_4-Cu_3SbS_4 solid solution material is noble due to the low lattice thermal conductivity. Se and S are in the same column and adjacent rows in the periodic table. Based on the Cu_3SbSe_4-Cu_3SbS_4 solid solution and the Sm-doped work in chapter 3, we choose double substitutions of Sm and S to combine the two advantages of high power factor ($Cu_{3-x}Sm_xSbSe_4$) and low lattice thermal conductivity (Cu_3SbSe_4-Cu_3SbS_4). So we synthesize $Cu_{3-x}Sm_xSbSe_{4-y}S_y$ ($x = 0$, 0.005, 0.0075 and $y = 0$, 0.5, 0.1, 0.15), and the results are presented in chapter 4.

For half-Heusler $Zr_{0.4}Hf_{0.6}NiSn$, to check whether excess Cu and Co can offer similar functions as excess Ni did, so we design the experiment Cu-excess $Zr_{0.4}Hf_{0.6}NiSn{:}x$Cu ($x \leq$ 0.05) and Cu-doped $Zr_{0.4}Hf_{0.6}Ni_{1-y}Cu_{y}Sn$ ($y \leq 0.05$), and Co-excess $Zr_{0.4}Hf_{0.6}NiSn{:}z$Co ($z \leq$ 0.05) presented in chapter 5 and chapter 6. In Cu-excess experiment presented in chapter 5 and Co-excess experiment presented in chapter 6, the half-Heusler (HH) / full-Heusler (FH) nanocomposites can also be achieved. At the same time, phonons scattering at the interfaces between FH nanoparticles and HH matrix is enlarged significantly, resulting in reducing lattice thermal conductivity.

Chapter 2 Experimental

2.1 Sample synthesis and preparation

2.1.1 Sample synthesis of chalcogenide

Polycrystalline $Cu_{3-x}Sm_xSbSe_4$ ($x \leq 0.025$) samples and $Cu_{3-x}Sm_xSbSe_{4-y}S_y$ ($x =$ 0, 0.005, 0.0075 and $y =$ 0, 0.5, 0.1, 0.15) were synthesized by melting high purity elemental Cu (99.9 %, powder), Sb (99.999 %, shot), Se (99.999 %, shot), Sm (99.999 %, powder) and S (99.9 %, powder) in stoichiometric proportions.

All the raw materials were sealed into evacuated quartz tubes under high vacuum. The tubes were heated to 1173 K for 12 h, then cooled to 823 K, and finally quenched in ice water. After quenching, samples were annealed at 623 K for 48 h to promote homogeneity. The ingots were pulverized into fine powders. Then the disc-shaped bulk samples were obtained by spark plasma sintering (SPS, **Figure 2-1**) for 5 min at 653 K under a pressure of 50 MPa. The relative densities of bulk samples after SPS exceed 94%.

Figure 2-1. Spark plasma sintering (SPS) apparatus used in the experiment in MPI-FKF Stuttgart.

2.1.2 Sample synthesis of half-Heusler

The ingots with nominal composition $Zr_{0.4}Hf_{0.6}NiSn:xCu$ ($x \leq 0.05$), $Zr_{0.4}Hf_{0.6}Ni_{1-y}Cu_ySn$ ($y \leq 0.05$), $Zr_{0.4}Hf_{0.6}Ni_2Sn$, $Zr_{0.4}Hf_{0.6}Ni_{1.98}Cu_{0.02}Sn$ and $Zr_{0.4}Hf_{0.6}NiSn:zCo$ ($z \leq 0.05$) were prepared by arc melting (Edmund Bühler GmbH, **Figure 2-2**) of stoichiometric amount of Zr (lump, 99.8%), Hf (rod, 99.8%), Ni (shot, 99.95%), Sn (shot, 99.95%), Cu (powder, 99.9%) and Co (powder, 99.9%) under an argon atmosphere for several minutes.

The ingots were remelted at least four times to ensure homogeneity. The obtained ingots were mechanically milled into fine powders. The obtained powders were loaded into the graphite die and compacted by spark plasma sintering at 1433 K for 5 min under 50 MPa in vacuum. The as-sintered samples were annealed at 1173 K for one week. The relative densities of annealed bulk samples exceed 94%.
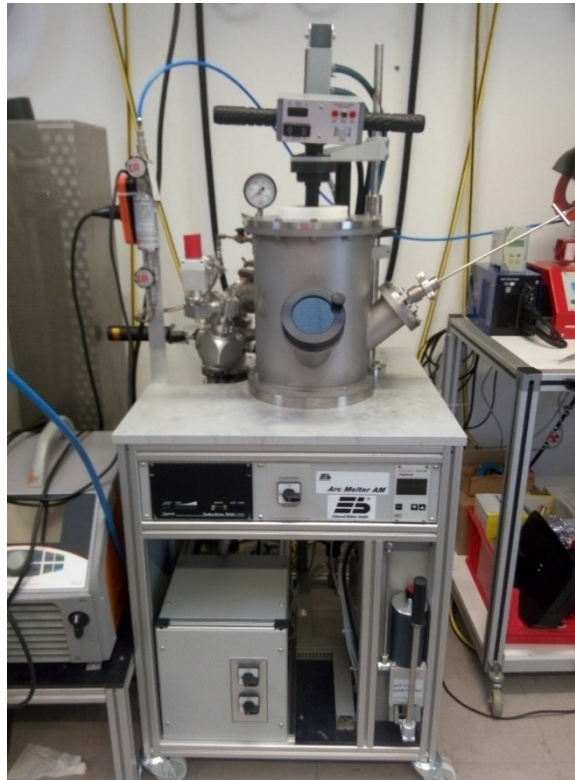
Figure 2-2. Arc melting equipment (Edmund Bühler GmbH) used in the experiment.

2.2 Characterization methods

X-ray diffraction (XRD) with Cu K_α radiation was used to check the phase constitutions of the samples. Moreover, the pristine sample was packed in sealed thin-walled glass capillary ($d = 0.5$ mm) and analyzed by temperature-changing XRD. A Bruker D8 Advance in Debye-Scherrer geometry equipped with a (111) Ge monochromator (Cu-$K_{\alpha 1}$) and a Vantac detector was used for temperature-dependent XRD measurements. Refinements of the unit cell parameters were carried out by LeBail fitting[110] using the FULLPROF 2.k program[111]. Unpolarized infrared reflectivity measurements were performed on sintered bulk materials at room temperature over a broad energy range ($\omega = 100$ cm^{-1} – 24000 cm^{-1}) with a Bruker vertex 80 Fourier-transform IR spectrometer coupled to a microscope (Bruker Hyperion®). The bulk materials have been polished to have a shiny and flat surface, which allow us to obtain a good absolute value of the reflectance. The bulk modulus was derived by nanoindentation (Nanoindenter XP, Keysight®) with a pyramidal Berkovich® tip. Calculations for the modulus were performed based on Oliver and Pharr (LIT) model[112], and the bulk modulus of the samples is about 65-67 GPa. The X-ray photoelectron spectroscopy (XPS) was used to determine the chemical state of the element in the compounds. The microstructure of samples is observed by scanning electron microscope (SEM). Phase characterization of the nanoparticles was carried out using a transmission electron microscope (TEM). TEM analysis was performed on lamellas which were prepared by in situ lift-out technique using a FEI Scios DualBeam FIB/SEM.

The electrical resistivity and thermopower were measured by ZEM-3 (ULVAC-RIKO®) in helium atmosphere. The uncertainty for electrical conductivity and thermopower is ± 7% and ± 7%. Hall coefficients were measured on a physical property measurement system (PPMS, Quantum Design®) in a magnetic field up to ± 0.5 T, and also cross checked via high temperature Hall Effect Systems (Lakeshore®) in a magnetic field up to ± 0.8 T. The estimated error of Hall coefficient is within ± 10%. The thermal diffusivities α were measured on disc samples (2–3 mm thick) with a NETZSCH LFA-457 apparatus in argon atmosphere.

The thermal conductivities κ were calculated according to $\kappa = DC_{p}\alpha$, where C_{p} is heat capacity obtained by differential scanning calorimetry (DSC404, NETZSCH®), and D is the density measured using the Archimedes method. The uncertainty for thermal conductivity is $\pm$ 10%.

2.2.1 XRD

The phase analysis is done by a Rigaku SmartLab X-ray Diffractometer as shown in **Figure 2-3**.

Figure 2-3. Rigaku SmartLab X-ray Diffractometer.

The measurement parameters are listed:

Measurement mode: θ / 2θ mode

Radiation type: Cu-$K_{\alpha 1,2}$ radiation

K_{β} Filter: Nickel foil

Slits: 5° Soller slits

Beam slit width: 10 mm

Geometry: Bragg-Brentano geometry

Angle range: 10°-90°.

Step width: 0.04°

Step duration: 0.3 s
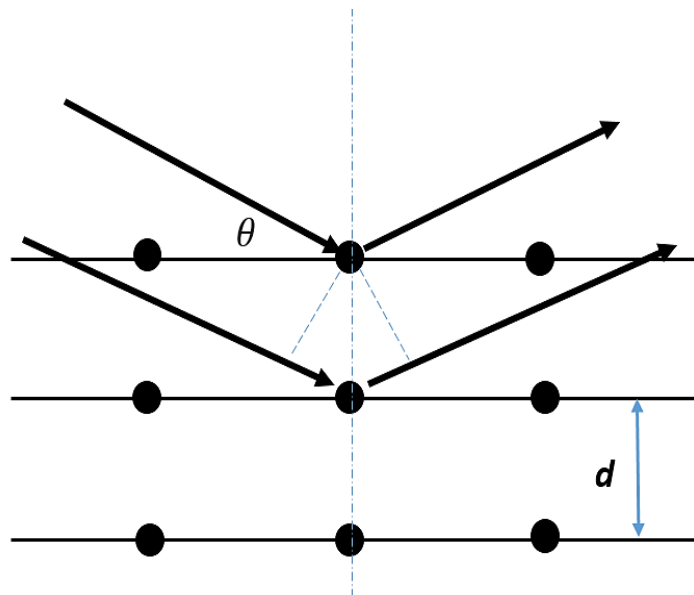
Figure 2-4. The schematic of Bragg's law.

Atoms are regular arrays in crystals. When an X-ray strikes an electron, the electrons of atoms will emanate secondary spherical waves. In most directions the waves are destructive interferences, however they are constructive interferences in some specific directions, which appear as spots on the diffraction pattern called reflections and are determined by Bragg's law (shown in **Figure 2-4**):

$$2d \sin \theta = n\lambda \tag{2-1}$$

where d means lattice spacing, θ is the incident angle, n means an integer, and λ is the wavelength of the beam.

2.2.2 LFA

Thermal diffusivity is obtained through a Netzsch laser flash system (LFA-457) shown in **Figure 2-5**.

Figure 2-5. Netzsch laser flash system (LFA-457).

LFA measurement principle is shown in **Figure 2-6**. The laser pulse heats the bottom of the measured sample. The energy will transfer from the bottom of the sample to the top. So, the detector can measure the changing of time-dependent temperature.[113] The mathematical model of this temperature increase permits the determination of the temperature-dependent thermal diffusivity.[113]

The specific heat capacity can be attained by comparison with a standard sample offered by the company measured in the same conditions. The uncertainty of the value measured by

34

LFA is around 10–20 %. So more precise value of heat capacity should be attained by differential scanning calorimetry (DSC).
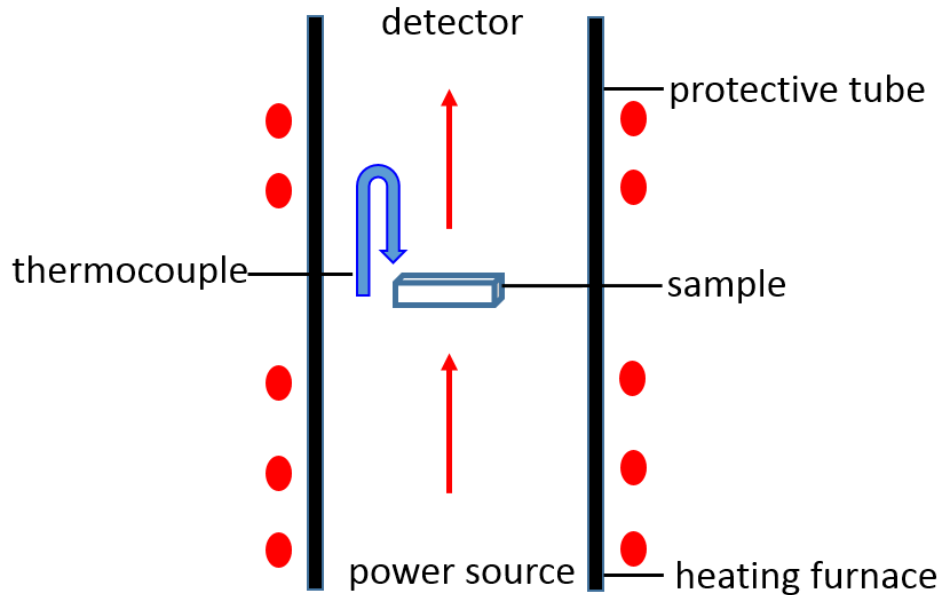
Figure 2-6. Measurement principle of LFA.[113]

2.2.3 ZEM

The electrical resistivity and Seebeck coefficient are measured by a Ulvac Riko Inc. ZEM-3 system shown in **Figure 2-7**.

The sketch of ZEM-3 is shown in **Figure 2-8**. The measured bar-shape sample is mounted between the upper and lower blocks. The Seebeck coefficient is calculated by the equation:

$$S = \frac{dE}{(T_2 - T_1)} \qquad (2\text{-}2)$$

To create a temperature gradient, the heat from the lower block goes through the sample in a fixed measurement temperature. Through the thermocouples we can get the two different temperatures (T_2 and T_1). At the same time the thermal electromotive force or the Seebeck voltage dE is obtained.[114]

Figure 2-7. ZEM-3 system (Ulvac Riko Inc.).

Through four-point probe method one can get the electrical resistivity. A constant current will go through the sample, so the voltage gradient dV between the same thermocouples can be measured as well.
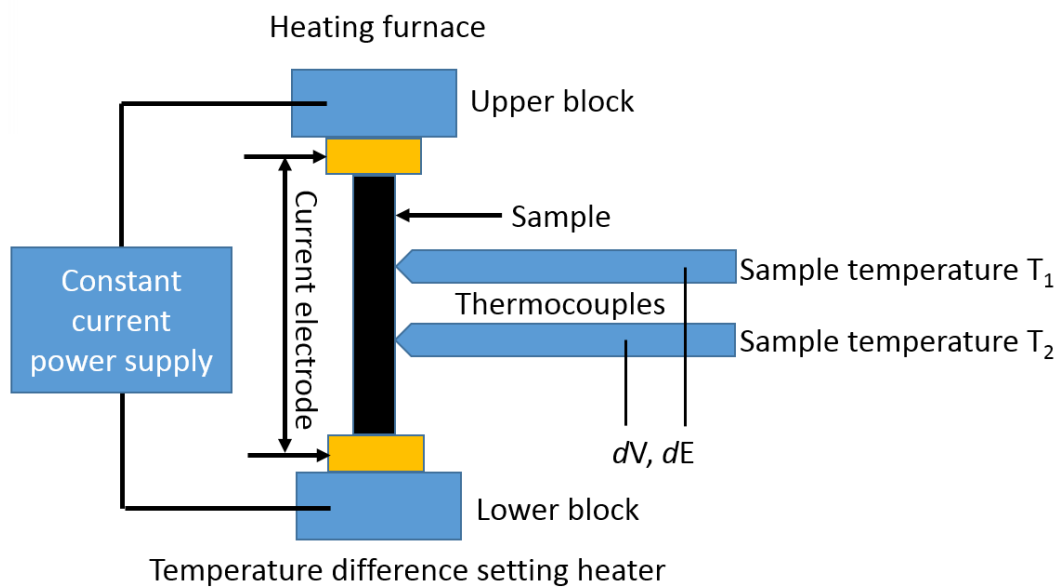
Figure 2-8. The schematic of ZEM-3. [115]

2.2.4 SEM

The microstructure of samples is observed by scanning electron microscope (SEM). The electron will interact with the nucleus and electrons of the sample when high energy electron beams focus and scan over the surface of the sample. **Figure 2-9** shows the different signals created including secondary electrons, back-scattered electrons, characteristic X-rays, light (cathodoluminescence), specimen current and transmitted electrons. Secondary electrons images can provide us the surface morphology of the sample and backscattered electrons images can provide us the information about different phases of the sample.[116]

Electron beam

X-Rays

Cathadoluminescence

Auger electrons

Secondary electrons

Backscattered electrons
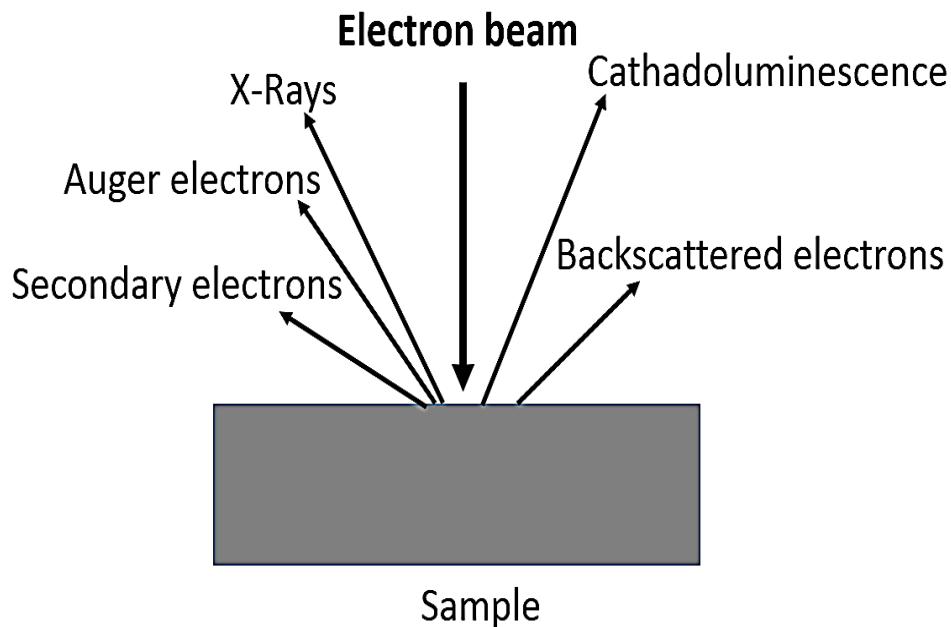
Sample

Figure 2-9. The multitude signal types of SEM.[117]

2.2.5 PPMS

The Hall coefficients of samples are measured by physical property measurement system (PPMS) from Quantum Design shown in **Figure 2-10**. Then the carrier concentration can be calculated through the following equation:

$$R_{\mathrm{H}} = \frac{1}{ne} \qquad\qquad (2\text{-}3)$$

where R_{H} is the Hall coefficient, n the carrier concentration, e the elementary charge.[118] According to the Hall carrier concentration from PPMS and resistivity from ZEM, we can get the Hall carrier mobility (equation 1-11 in chapter 1).

Figure 2-10. PPMS (Quantum Design).

The low temperature resistivities of samples are measured by van der Pauw method in PPMS as well. The resistivity can be calculated through the following equation:

$$\rho = \frac{\pi d}{ln2}\left[\frac{R_{\mathrm{AB}}+R_{\mathrm{BC}}}{2}\right]f(\frac{R_{\mathrm{AB}}}{R_{\mathrm{BC}}}) \qquad\qquad (2\text{-}4)$$

where A B C and D mean 4 corners of the samples, R means the resistance, and f is the function of ratio $\left(\frac{R_{\mathrm{AB}}}{R_{\mathrm{BC}}}\right)$ and can be given approximately as:

$$f = 1 - \left[\frac{R_{AB}-R_{BC}}{R_{AB}+R_{BC}}\right]^2 \frac{ln2}{2} - \left[\frac{R_{AB}-R_{BC}}{R_{AB}+R_{BC}}\right]^4 \left\{\frac{(ln2)^2}{4} - \frac{(ln2)^3}{12}\right\} \qquad (2\text{-}5)$$

2.2.6 TEM

A transmission electron microscope (TEM) is used to analyze the samples in the realms from microspace to nanospace. As shown in **Figure 2-11**, the TEM consists of four parts: electron source, electromagnetic lens system, sample holder, and imaging system.
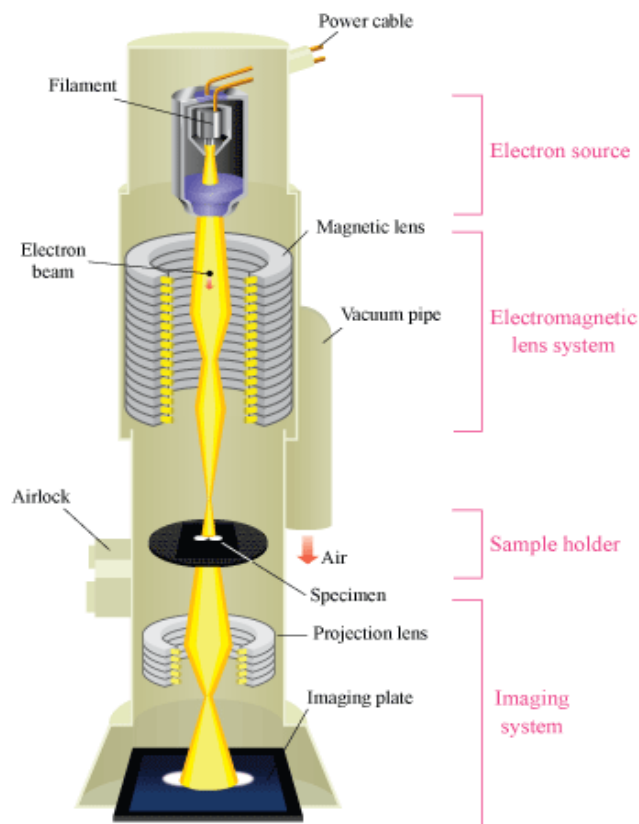
Figure 2-11. The schematic outline of a TEM.[119]

TEM can give high-resolution and high magnification imaging to show the detailed micro-structural information. Through diffraction pattern, X-ray and electron-energy analysis, TEM can investigate the crystal structures, orientations and different chemical compositions, nanoprecipitates in the samples.[120]

2.2.7 XPS

To get more information about Cu in the compounds $Zr_{0.4}Hf_{0.6}NiSn:xCu$, the X-ray photoelectron spectroscopy (XPS) experiment is carried out to determine the chemical state of the Cu element in the compounds. In the XPS experiment, we measure around 3-7 nm deep in the samples, so we assume that the oxide is on the surface while the metallic components are below the surface.
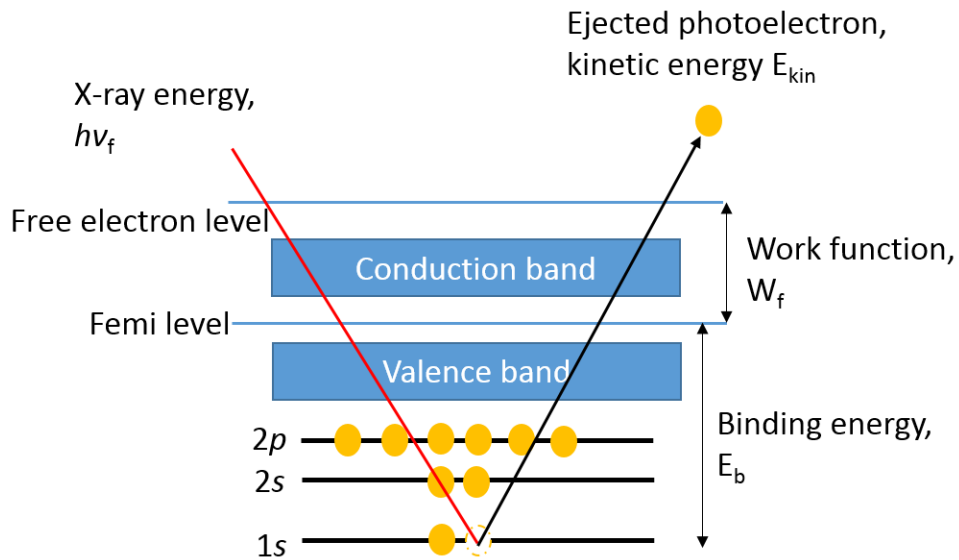
Figure 2-12. Principle of XPS.[121]

X-ray photoelectron spectroscopy (XPS) is a surface characterization technique. XPS shows the chemical elements at the surface and the nature of the chemical bond information between these elements.[122] Photoemission principle of XPS is shown in **Figure 2-12**: when an X-ray attacks the surface of the sample, some electrons under the fermi level will be excited to escape.[123] The binding energy E_b can be expressed as:

$$E_b = h\nu_f - E_{kin} - W_f \tag{2-6}$$

where W_f means work function, E_{kin} kinetic energy of ejected photoelectron, ν_f frequency of X-ray energy, h Plank constant.

In summary, the detailed experimental procedures for Cu_3SbSe_4 and half-Heusler are shown in **Figure 2-13**.
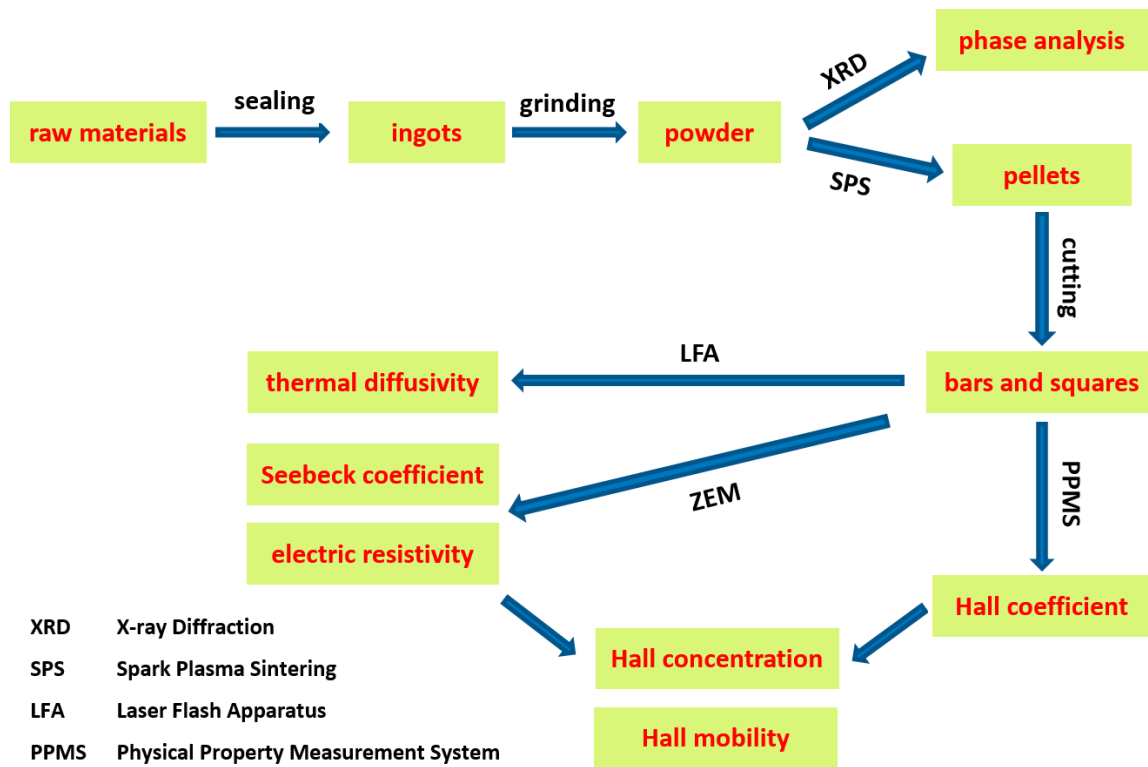
Figure 2-13. A schematic figure demonstrating the detailed experimental procedure.

Experimental

Chapter 3 Synthesis and Thermoelectric Properties of Sm Doped Chalcogenide Cu₃SbSe₄

3.1 Abstract

The synthesis and thermoelectric performances of $Cu_{3-x}Sm_xSbSe_4$ ($x \leq 0.025$) samples are investigated in this chapter. High thermoelectric performance of a material arises from various compromises between adversely inter-dependent transport properties. A key tradeoff is the 3-way interplay between the carrier concentration n_H, carrier mobility μ_H, and effective mass m^*. Doping typically changes the electronic structure in a way that all three quantities are affected. While it is rather obvious that the carrier concentration is changed, dopants give rise also to additional scattering and thereby generally decrease the carrier mobility. Therefore, it is rare to see carrier concentration and carrier mobility simultaneously increase upon doping. In Cu_3SbSe_4, however, we have observed that slight Sm doping increases both carrier concentration and carrier mobility owing to details of the band structure and the engagement of a light valence band by Sm doping. In addition, Sm doping dramatically reduces the lattice thermal conductivity by enhancing point-defect scattering of heat carrying phonons. As a result, we have attained a zT of ~1.0 at 648 K for Cu_3SbSe_4:Sm at a carrier concentration of 4.3×10^{18} cm^{-3}.

3.2 Introduction

Research on thermoelectric materials is an active area in science and engineering in the wake of energy and environmental crises in recent years. Without moving parts, greenhouse gas emissions and noises, all solid-state thermoelectric devices are promising for energy harvesting of waste heat and refrigeration. As discussed in chapter 1, zT depends crucially on the material's electrical and thermal properties at the same time. Furthermore, it is instructive to define a second quantity, namely, the material's quality factor B.[124]

$$B \sim \frac{\mu((m^*/m_0)^{\frac{3}{2}})}{\kappa_{\text{lat}}} T^{5}/_{2} \tag{3-1}$$

where m^*, m_0, μ, κ_{lat}, are the effective mass, free electron mass, carrier mobility, and lattice thermal conductivity, respectively. The product of μ and $(m^*/m_0)^{3/2}$ is called the weighted mobility. In light of Eq. (3-1), a good thermoelectric material should have a large weighted mobility and, at the same time, a low lattice thermal conductivity, which can be regarded as a weaker version of the ´electron-crystal phonon-glass´ (ECPG) paradigm.[125]

Enhancing the weighted mobility is a challenge in that the two governing contributors μ and m^* are both determined by the electronic band structure and scattering mechanism. Experimentally, there is no simple way to tune μ and m^* separately. Substitution doping has been the primary approach to tune μ and m^* since the beginning of modern thermoelectric research.[126] Doping directly determines the carrier concentration n, which in turn affects μ and m^*. n and μ are generally inversely inter-dependent because the dopants not only contribute extra carriers but also lead to more scattering of the carriers which decreases μ. Modulation doping is a promising approach in this regard but its implementation has inherent restrictions.[27]

To give new insights into the weighted mobility, it is instructive to inspect μ and m^* of state-of-the-art thermoelectric materials such as PbTe[37, 127] and SiGe[128]. These materials possess a high weighted mobility with a cubic crystal structure. The obvious

common character of these materials is that their band structures near the Fermi level are dominated by *s* or *p* states (orbits). An immediate question arises as to whether a material with an *s*- or *p*-states dominated Fermi surface but a lower crystal symmetry would be able to have a large weighted mobility. This is the motivation of our present work on Cu$_3$SbSe$_4$ compounds.

Copper chalcogenides have recently received increasing attention due to a high thermoelectric performance and low raw material costs. Good examples are the mixed conductor Cu$_2$Se with a liquid-like phonon behavior[129] and the layered oxyselenide BiCuSeO[130, 131] The tetragonal crystal structure of Cu$_3$SbSe$_4$ is lower in symmetry compared to the cubic system, and its electron band structure near the Fermi level is dominated by the *s* states of Sb and *p* states of Se.[77]

From density functional theory (DFT) calculations with spin-orbit coupling, shown in **Figure 3-1a**, we can determine a rather flat (i.e. heavy) band around E_f (band H) which is dominating the transport properties. Results reported by Wei *et al.* confirmed that the transport properties of Cu$_3$SbSe$_4$ material are very well characterized within a single parabolic band (SPB) model.[80] However, through appropriate doping / substitution, a much lighter band (band L) can be activated to contribute also to the transport of electron holes and, consequently, the carrier mobility can be increased.

Figure 3-1b is *B* factor versus mobility over lattice thermal conductivity at 325 K for the pristine and Sm-doped Cu$_3$SbSe$_4$ specimens. The carrier concentration *n* is given in units of cm^{-3}. **Figure 3-1c** is temperature-dependent figure of merit *zT*. **Figure 3-1d** is a comparison of different element-doped Cu$_3$SbSe$_4$ compounds. In the present work, we achieve simultaneously an enhanced weighted mobility via engaging the light valence band and reduced lattice thermal conductivity by strengthening point-defect scattering of heat carrying phonons, resulting in higher *B* factors shown in **Figure 3-1b** and *zT* values shown in **Figure 3-1c**. The highest *zT* of ~1.0, which is unprecedented for Cu$_3$SbSe$_4$ compounds prepared by

a melting method, is achieved for Sm-doped Cu_3SbSe_4 with a carrier concentration of 4.3e18 cm^{-3} (**Figure 3-1d**). [74, 78-83]
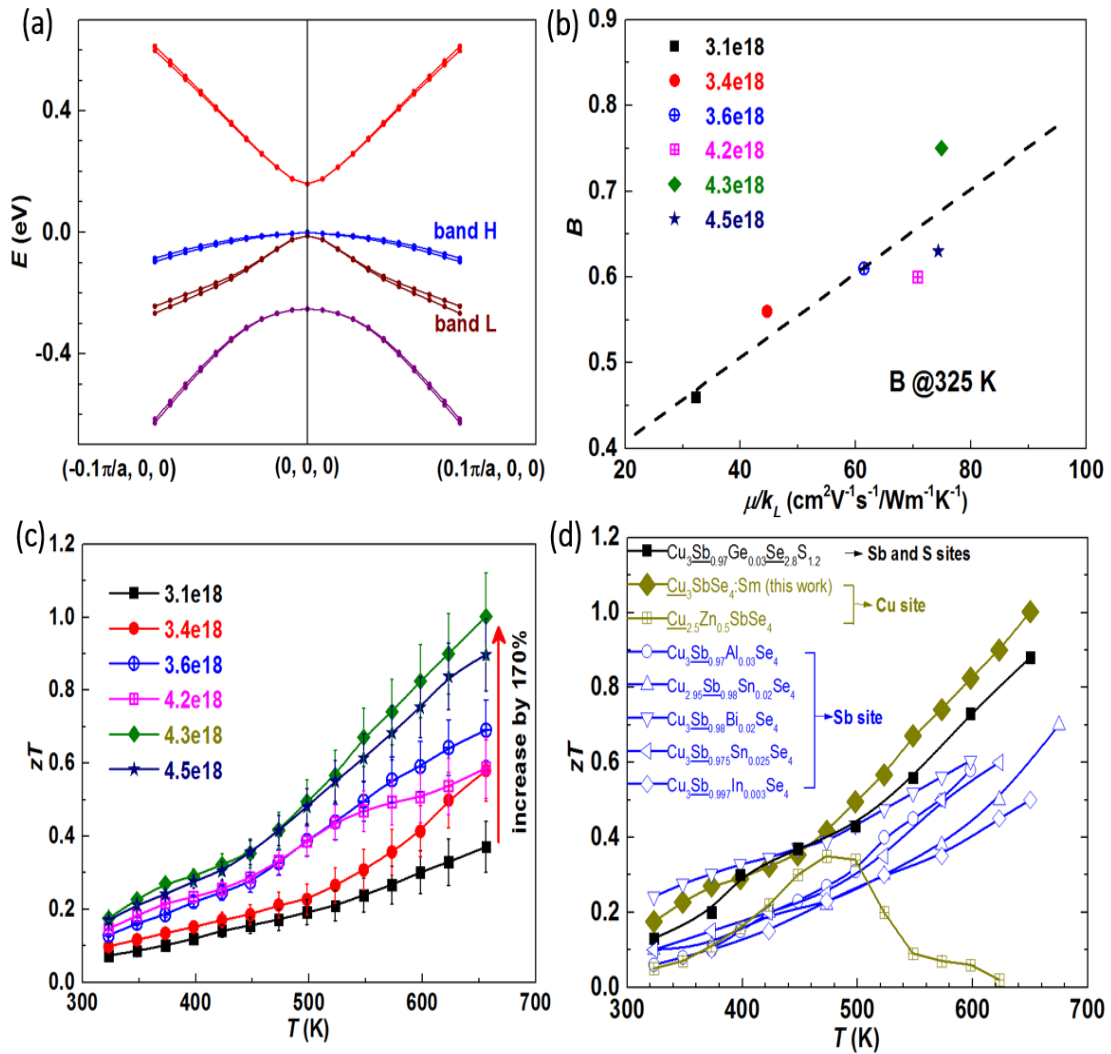
Figure 3-1. (a) Calculated band structure of Cu_3SbSe_4 including spin-orbit coupling (SOC). (b) B factor versus mobility over lattice thermal conductivity at 325 K for the pristine and Sm-doped Cu_3SbSe_4 specimens. The carrier concentration n is given in units of cm^{-3}. (c) Figure of merit zT as a function of temperature for the pristine and Sm-doped Cu_3SbSe_4 specimens. (d) A comparison of different element-doped Cu_3SbSe_4 compounds.

3.3 Experimental procedure: DFT calculations

The electronic structure of Cu_3SbSe_4 was obtained by using the experimental crystal structure. Density functional theory (DFT) calculations were performed with the VASP (Vienna ab initio simulation package) code[132] using the Heyd-Scuseria-Ernzerhof (HSE) hybrid functional[133] for electronic exchange and correlation and a $8 \times 8 \times 6$ k-point grid including the Gamma point. Spin-orbit coupling is also included in the calculation. By analyzing the band structure we find an energy gap of 0.16 eV at the Gamma point Γ. While the highest valence band is rather flat (*i.e.* heavy) only 10 meV below a band with much larger slope (*i.e.* lighter effective mass) is found.

3.4 Results and discussion

3.4.1 Phase constitution characterization

Table 3-1. The nominal composition and carrier concentration n for the samples.

Sample name	Nominal composition	n (cm^{-3})
3.1e18	Cu_3SbSe_4	3.1(2) e18
3.4e18	$Cu_{2.9975}Sm_{0.0025}SbSe_4$	3.4(4) e18
3.6e18	$Cu_{2.995}Sm_{0.005}SbSe_4$	3.6(4) e18
4.3e18	$Cu_{2.9925}Sm_{0.0075}SbSe_4$	4.2(5) e18
4.2e18	$Cu_{2.99}Sm_{0.01}SbSe_4$	4.1(8) e18
4.5e18	$Cu_{2.975}Sm_{0.025}SbSe_4$	4.4(7) e18

As discussed above, doping alters the carrier concentration, which in turn governs the weighted mobility. Since the transport properties directly depend on the carrier concentration,

the room temperature Hall carrier concentration is used to identify the samples. **Table 3-1** summarizes the nominal composition, and the corresponding carrier concentration of as prepared $Cu_{3-x}Sm_xSbSe_4$ $(x \leq 0.025)$ samples.

In this study, the carrier concentration was derived from the Hall coefficient. We hereafter use the carrier concentration to denote the Sm-doped samples, in the form of "Cu_3SbSe_4:Sm, n", where the n is the numerical value of carrier concentration in the units of cm^{-3}. From **Table 3-1**, we see that even in the undoped sample, there are Cu and Se deficiencies and the similar results are found in Wei *et al.*' work.[134]
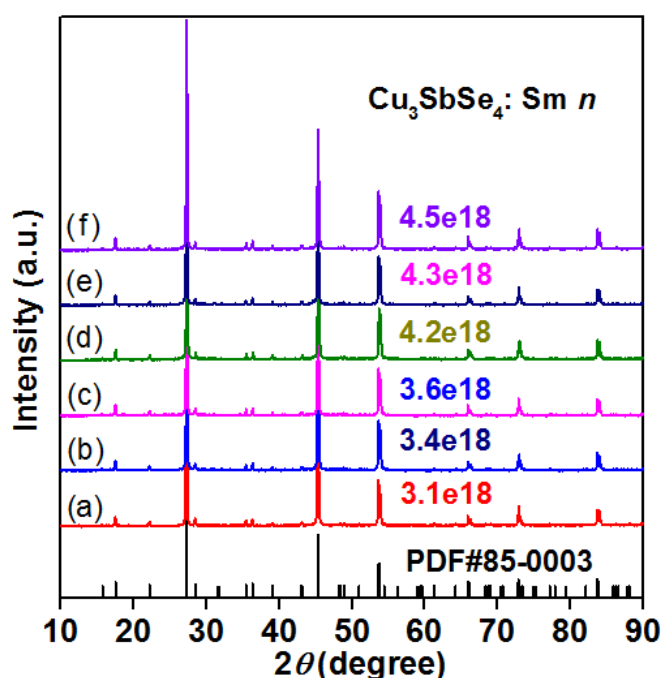
Figure 3-2. XRD patterns of the pristine and Sm doped Cu₃SbSe₄ samples.

Phase constitutions of the pristine and Sm doped Cu₃SbSe₄ samples are investigated by XRD, as shown in **Figure 3-2**. From **Figure 3-2**, all diffraction reflections can be well indexed to the tetragonal Cu₃SbSe₄ structure. This exhibits that no obvious impurity phases are witnessed in the produced specimens. To make sure there is no phase transition and phase separation during our processing, a Bruker D8 Advance in Debye-Scherrer geometry equipped with a (111) Ge monochromator (Cu-$K\alpha_1$) and a Vantac detector is used for

48

temperature-dependent powder X-ray diffraction measurements shown in **Figure 3-3a**. We test the temperature-changing XRD from room temperature (RT) to 50 °C, 100 °C, 150 °C, 175 °C, 200 °C, 225 °C，250 °C，300 °C，350 °C and then cool down to the room temperature finally. From **Figure 3-3b** we can see that there are only obvious peak shifts towards lower angle with the temperature increasing due to the lattice expansion.
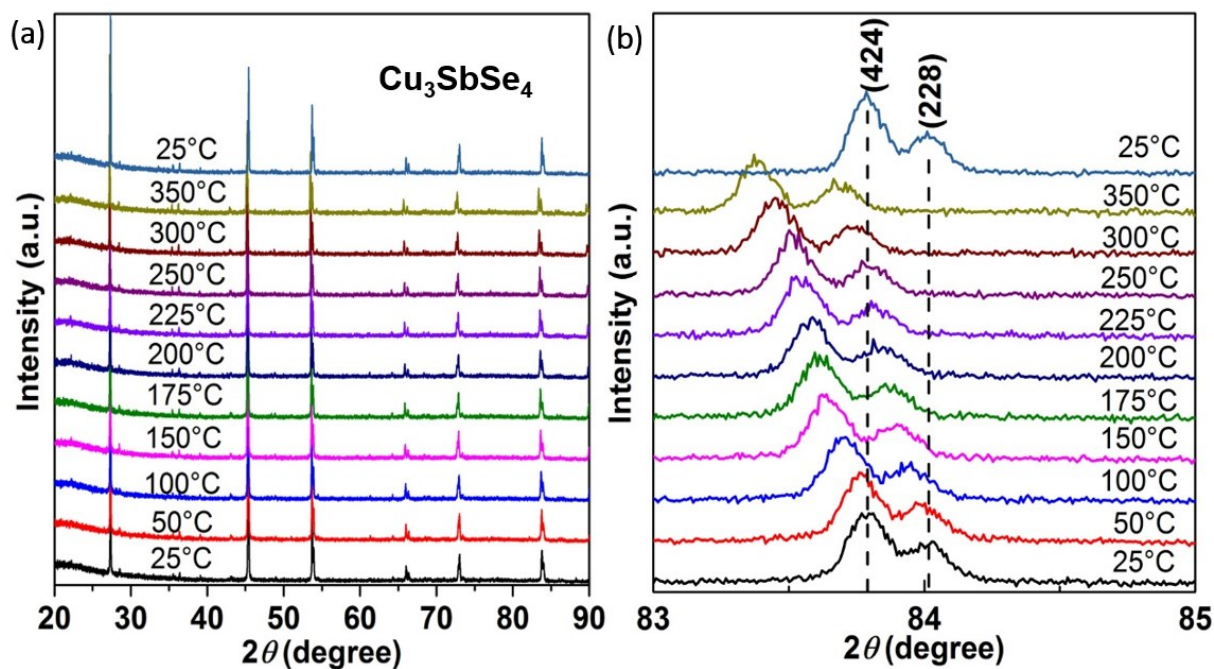
Figure 3-3. (a) Temperature-changing XRD pattern of Cu₃SbSe₄ and (b) peak shift due to heat expansion at high angle.

Refinements of the temperature-changing XRD pattern of the unit cell parameters are carried out by LeBail fitting[110] using the FULLPROF 2.k program[111] and the results are shown in **Table 3-2**. From the **Table 3-2**, we can conclude that the unit cell parameters a, c and V are increasing from room temperature (RT) to 50 °C, 100 °C, 150 °C, 175 °C, 200 °C, 225 °C，250 °C，300 °C，350 °C. We notice the unit cell parameters at RT1 (room temperature before heating) are larger than that of RT2 (room temperature after heating). There are Cu and Se deficiencies in the compound, so after heating, the unit cell parameters will be kind of smaller because of the evaporation of Cu and Se.

Table 3-2. Results of LeBail fits of Cu_3SbSe_4.

	a/ pm	c/ pm	V/ 10^6 pm³	R_p/ %	R_{wp}/ %	R_{Bragg}/ %	χ^2
RT1	565.52(1)	1126.06(2)	360.13(1)	9.19	12.6	4.05	1.21
323 K	565.64(1)	1126.24(3)	360.34(3)	9.84	13.6	0.137	1.47
373 K	566.01(1)	1126.71(3)	360.96(1)	9.30	12.5	0.588	1.17
423 K	566.37(1)	1127.16(3)	361.56(1)	11.0	14.3	95.9	1.47
473 K	566.73(1)	1127.64(4)	362.18(2)	12.8	16.3	57.3	1.87
523 K	567.11(2)	1128.12(4)	362.81(2)	13.9	17.7	97.0	2.15
623 K	567.92(1)	1129.07(2)	364.16(1)	10.1	13.4	82.5	1.18
RT2	564.87(2)	1124.80(5)	358.90(2)	9.09	12.4	0.143	1.17

3.4.2 Decoupling of electrical and thermal properties

The temperature-dependent electrical resistivity of the pristine (3.1e18) and Sm-doped Cu_3SbSe_4 specimens is presented in **Figure 3-4a**. The electrical resistivity of Cu_3SbSe_4 is significantly reduced upon slight Sm doping, owing to the enhancement of both carrier concentration and Hall mobility. Fitting the resistivity of pristine Cu_3SbSe_4 with the Arrhenius relation $\rho = \rho_0 \exp(E_a/k_B T)$, where ρ_0, E_a and k_B are pre-exponential factor, apparent activation energy for the conduction, and the Boltzmann constant, respectively, leads to an apparent activation energy and band gap ($E_g = 2E_a$) of ~ 0.13 eV and 0.26 eV quite close to values reported in literature.[80]
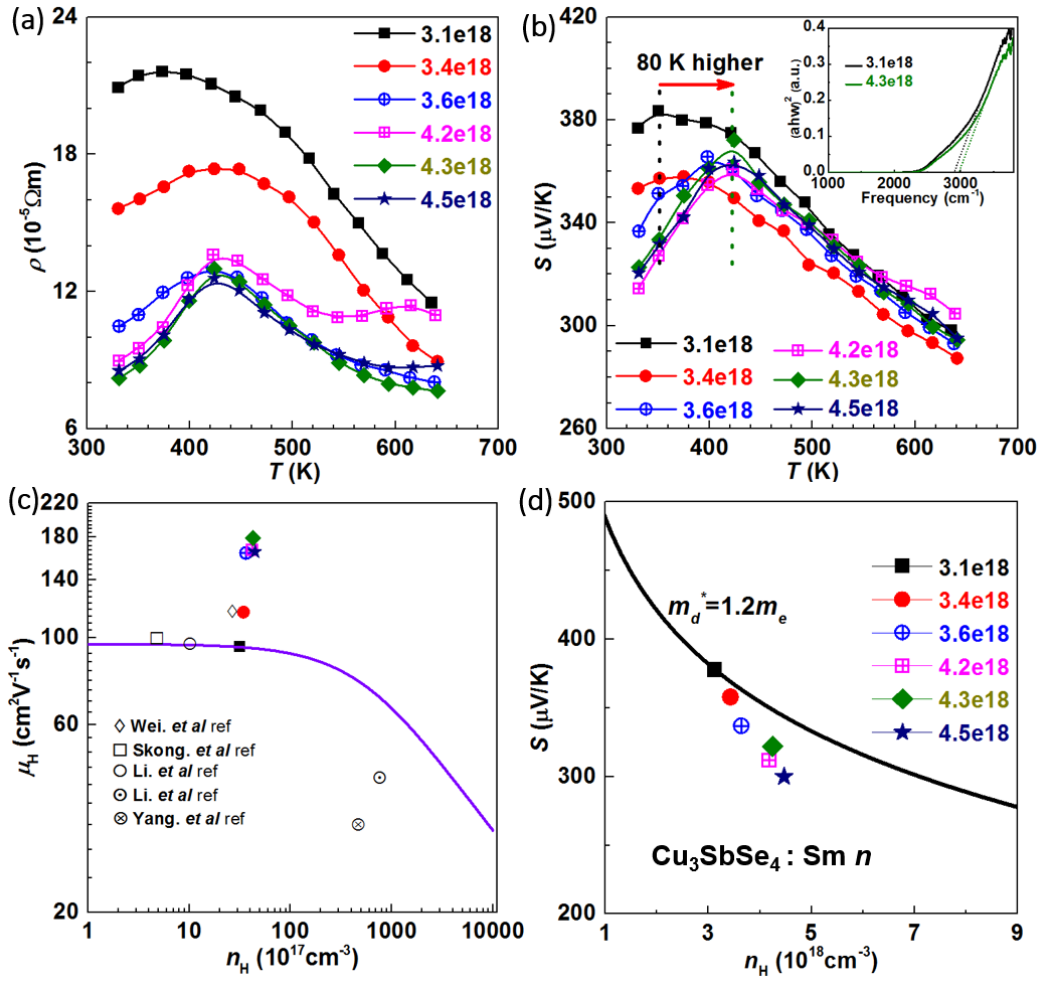
Figure 3-4. (a) Temperature dependence of electrical resistivity of the pristine (3.1e18) and Sm-doped Cu₃SbSe₄ specimens. (b) Temperature dependence of thermopower of the pristine and Sm-doped Cu₃SbSe₄ specimens, and inset is the frequency dependence of the absorption coefficient of the pristine sample (3.1e18) and Sm-doped Cu₃SbSe₄ (4.3e18) sample. (c) The Hall mobility as a function of the carrier concentration for the pristine and Sm-doped Cu₃SbSe₄, and the purple solid line is for pristine Cu₃SbSe₄ with $m_d^* = 1.2m_e$. (d) Pisarenko plot of the pristine and Sm-doped Cu₃SbSe₄ at room temperature, and the black solid line represents the pristine Cu₃SbSe₄ with $m_d^* = 1.2m_e$.

Figure 3-4b displays the temperature-dependent thermopower. Over the entire temperature range, the thermopower is positive, indicating a p-type conduction with holes as the major charge carriers. Using the Goldsmid-Sharp formula $E_g = 2eS_{max}T_{S_{max}}$,[135] band gap E_g of the pristine sample and the Cu₃SbSe₄:Sm, 4.3e18 sample are around 0.28 eV and 0.32 eV,

respectively. Apparently, Sm doping slightly opens a band gap. In addition, the band gap was estimated by optical properties using unpolarized infrared reflectivity measurements. The optical conductivity was extracted from the reflectivity data via Kramers-Kroning transformation. At low frequencies, the data were extrapolated to zero frequency with a constant value, while the high energy part were extrapolated up to 500000 cm^{-1} using a free-electron model $R(\omega) \sim \omega^{-4}$. The frequency-dependent absorption coefficient α ($\propto \sigma(\omega)$) times the photon energy ω were fitted with the formula $\alpha \hbar \omega \propto (\hbar \omega - E_g)^{1/2}$ assuming a direct transition above the gap,[136] where E_g is the direct energy gap, $\sigma(\omega)$ is the real part of the conductivity. The inset of **Figure 3-4b** is the frequency-dependent the absorption coefficient of the pristine sample (3.1e18) and Sm-doped Cu$_3$SbSe$_4$ (4.3e18) sample. As shown in the inset of **Figure 3-4b**, E_g of the undoped sample and Cu$_3$SbSe$_4$:Sm, 4.3e18 are found to be ~ 0.35 eV and 0.37 eV, respectively. A similar band gap of Cu$_3$SbSe$_4$ is reported in Zn$_4$Sb$_3$-Cu$_3$SbSe$_4$ nanocomposites by Zou *et al.* using an UV−visible absorption spectrometry.[137]

The increase of the band gap by Sm doping also leads to a suppression of the bipolar effect, thus, improving the figure of merit. In thermoelectrics, the bipolar effect is detrimental as the thermopower will be suppressed if electrons and holes are both present.[138] As shown in **Figure 3-4b**, the crossover temperature of thermopower has been shifted to ~ 80 K higher temperature due to the larger band gap.

Figure 3-5 is the Hall mobility as a function of temperature for the pristine and Sm-doped Cu$_3$SbSe$_4$ from PPMS. The Hall mobility of all the samples decreases with increasing temperature, roughly following a $T^{-3/2}$ law that is expected from electron-acoustic phonon scattering. Surprisingly, the Hall mobilities of Sm-doped samples are higher than that of pristine Cu$_3$SbSe$_4$.
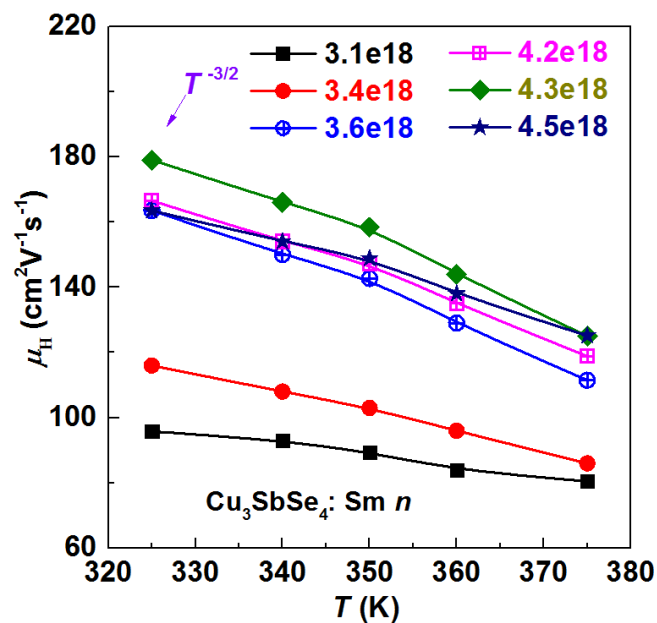
Figure 3-5. Hall mobility as a function of temperature for the pristine and Sm-doped Cu₃SbSe₄ from PPMS.
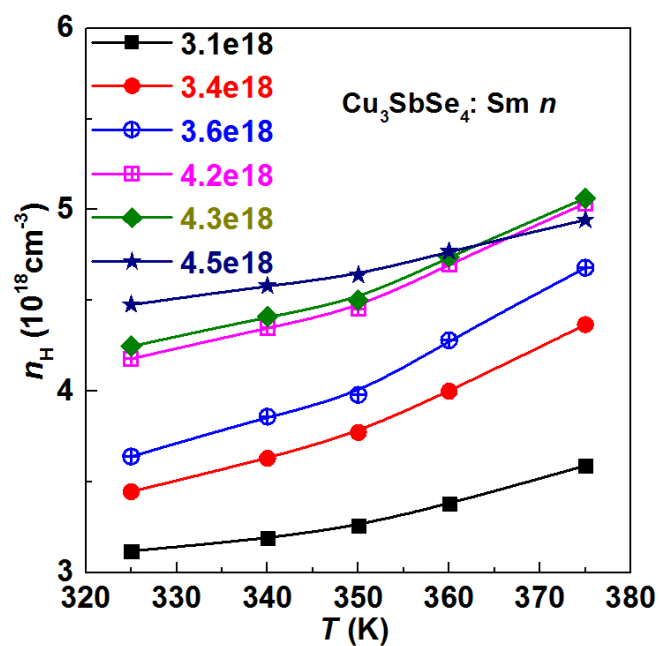
Figure 3-6. Hall carrier density as a function of temperature for the pristine and Sm-doped Cu₃SbSe₄ from PPMS.

The measured carrier concentration n_H at different temperatures from PPMS is shown in **Figure 3-6**. The carrier concentrations of all the samples increase with increasing temperature and Sm doping generally increases the carrier concentration but not in a linear relation with the nominal Sm doping ratio.
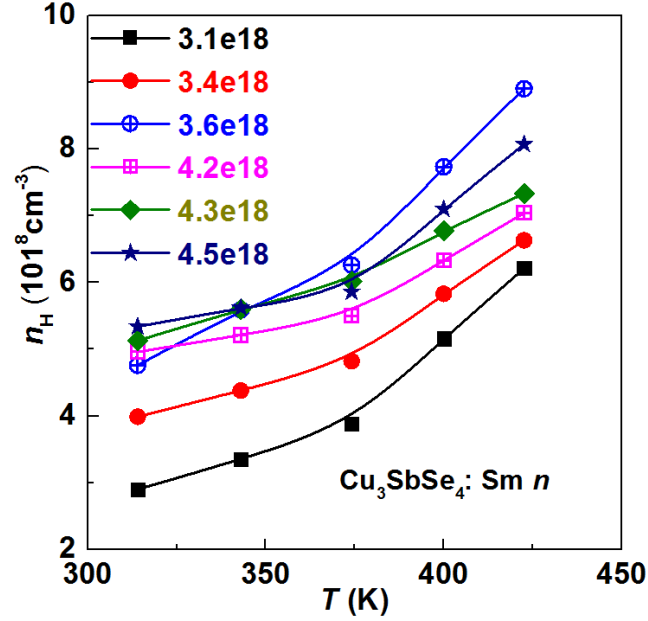
Figure 3-7. Hall carrier density as a function of temperature for the pristine and Sm-doped Cu₃SbSe₄ from high temperature Hall Effect System.

To confirm the trend of the changing of carrier concentration, we use the Van der Pauw method in a magnetic field up to ± 0.8 T to measure the carrier concentration as well, shown in **Figure 3-7**. The measured carrier concentration n_H at different temperatures from PPMS and using the Van der Pauw method in a magnetic field up to ± 0.8 T match satisfactorily. **Figure 3-4c** shows the carrier concentration dependence of Hall mobility μ_H. In the SPB model, μ_H in a system with a reduced chemical potential η could be expressed as[80]:

$$\mu_H = \frac{3\sqrt{\pi}}{8} \mu_0 \frac{F_{-1/2}(\eta)}{F_0(\eta)} = \frac{\pi e \hbar^4 \rho v_{LA}^2 N_V^{5/3}}{2\sqrt{2} m^{*5/2} (k_B T)^{3/2} \Xi^2} \frac{F_{-1/2}(\eta)}{F_0(\eta)} \tag{3-2}$$

$$F_n(\eta) = \int_0^\infty \frac{x^n dx}{1+\exp(x-\eta)} \tag{3-3}$$

where μ_0 is the nondegenerate limit of mobility governed by the acoustic phonon scattering process, v_{LA} is the longitudinal speed of sound, N_V is the degeneracy of band, $\hbar$ is the reduced Planck constant, η is the reduced Fermi level $E_F/(k_BT)$, and Ξ is the deformation potential coefficient.

Though the SPB model is oversimplified, it can provide useful information about the trend of change when applied on a multiple-band system like Cu_3SbSe_4. Here we use the data v_{LA} of 3859 ms^{-1},[77] $N_V = 3$[139] and a deformation potential coefficient Ξ of 15 eV at 300 K.[80] The SPB model provides a good description for the undoped sample, with μ_H determined to be 90 $cm^2V^{-1}s^{-1}$. Our result are consistent with other literature reports on pristine samples [74, 80, 81, 140, 141]. On the other hand, the mobility of the doped sample, is about 87% higher than this value. m^* can be calculated from the carrier concentration dependence of thermopower (Pisarenko plot, **Figure 3-4d**) for each sample and reveals a clear decrease when going from pristine to doped samples. A smaller effective mass usually means more mobile carriers and a higher thermoelectric performance.[37, 142]

Previous band structure calculations for Cu_3SbSe_4 suggest that the valence band edge at the Γ point consists of a doubly degenerate band and a single light band about 10 meV below. There are two possibilities occurred in the experiment. One is the shift of the fermi level. Consequently, as the chemical potential moves deep into the valence bands with increasing carrier density, the single light band begins to play a more noticeable role in the transport, leading to a smaller m^* when analyzed with the SPB model. The doping ratio is quite relevant for carrier mobility as well. When the doping ratio of Sm is increased further, the mobility will decrease slightly, as shown in **Figure 3-4c** and **Figure 3-5**. Another possibility is the thermally activated behavior. Because the properties are tested above the room temperature, the hole in the light valence band is activated to the heavy band thermally. So the carrier mobility comes from the contribution of both heavy and light bands.
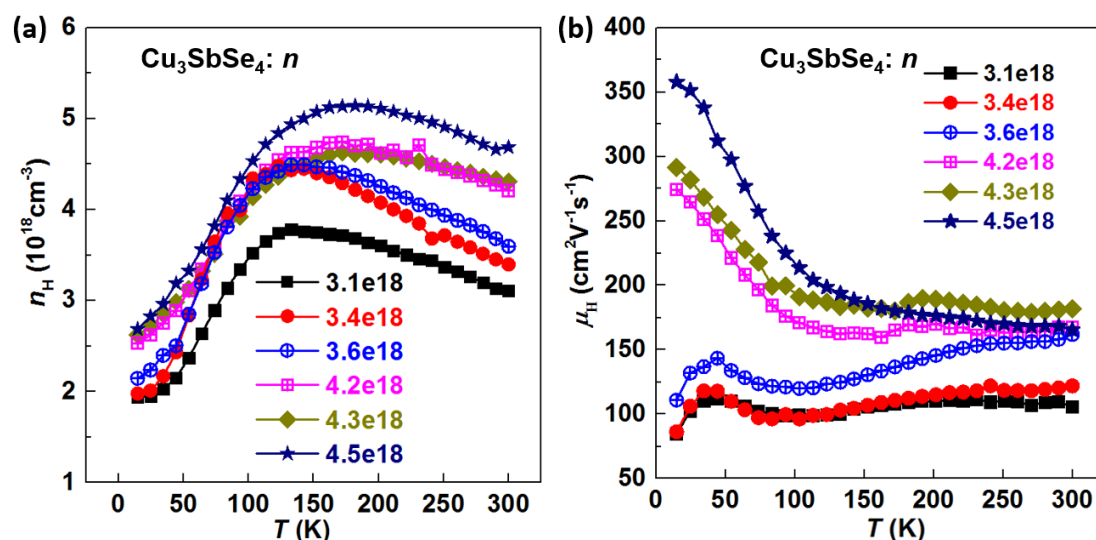
Figure 3-8. (a) Hall carrier density as a function of temperature from 5 K to 300 K for the pristine and Sm-doped Cu_3SbSe_4.(b) Hall carrier mobility as a function of temperature from 5 K to 300 K for the pristine and Sm-doped Cu_3SbSe_4.

To get more information about the transport properties, we measure the low temperature Hall carrier density n_H from 5 K to 300K. The measured carrier concentration and mobility from PPMS is shown in **Figure 3-8**. The carrier concentrations of all the samples increase with increasing temperature from 5 K to 150 K and decrease with increasing temperature from 150 K to 300 K. The trend of carrier mobilities of the three relatively heavily doped samples (4.2e18, 4.3e18 and 4.5e18) are quite different from other three samples. Specially, when the temperature is lower than 50K, carrier mobilities of the three relatively heavily doped samples are much larger than those of other three samples. At the low temperature range, the thermal activation is not so obvious, so the improved transport properties should come from the changing of the band structure.

The power factor PF (= S^2/ρ) of all the Sm-doped Cu_3SbSe_4 samples is presented in **Figure 3-9**. The PF of doped samples is indeed elevated as compared with that of Cu_3SbSe_4 in the entire studied temperature range. At 650 K, the PF values reach 1.07×10^{-3} W/mK² and 1.15×10^{-3} W/mK² for Cu_3SbSe_4:Sm, 3.6e18 and Cu_3SbSe_4:Sm, 4.3e18, which is around 40% and 50% larger than that of the pristine compound (7.7×10^{-4} W/mK²).

56
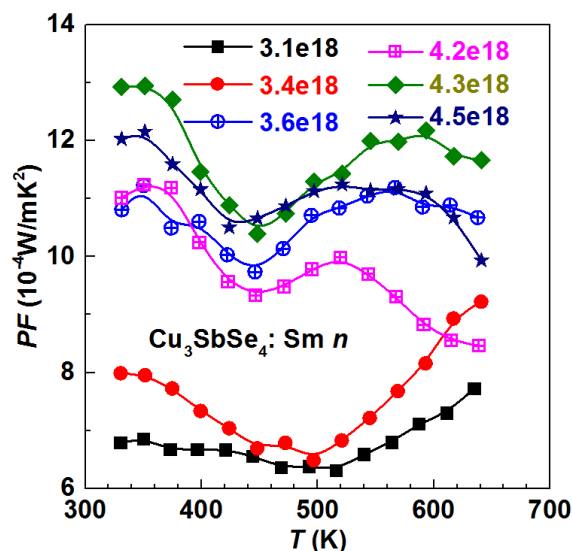
Figure 3-9. Power factor as a function of temperature for the pristine and Sm-doped Cu₃SbSe₄.

3.4.3 Reduced lattice thermal conductivity and phonon scattering mechanisms.
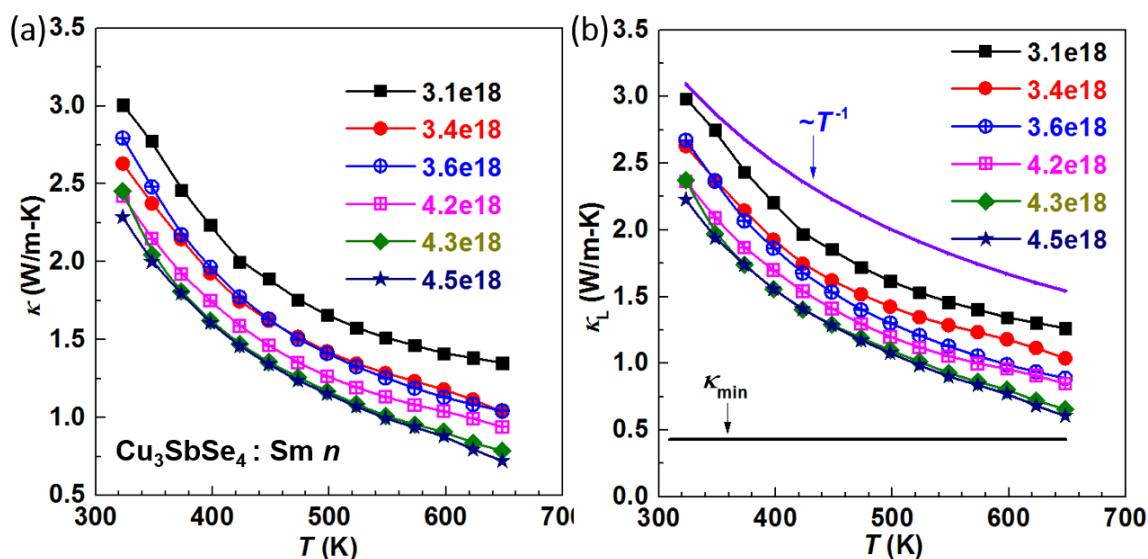
Figure 3-10. Temperature dependence of (a) total thermal conductivity and (b) lattice thermal conductivity for the pristine and Sm-doped Cu₃SbSe₄ specimens.

Figure 3-10a displays the temperature-dependent thermal conductivity κ. It can be seen that κ of all the specimens drops with increasing temperature. κ_L of the doped samples is much

lower than that of the pristine sample. In a semiconductor, κ is composed of the lattice thermal conductivity κ_L and the carrier contribution κ_e: $\kappa = \kappa_L + \kappa_e$. κ_e is normally assessed by using the measured electrical conductivity σ through the Wiedemann-Franz relation: $\kappa_e = L\sigma T$, where L is the Lorenz number.
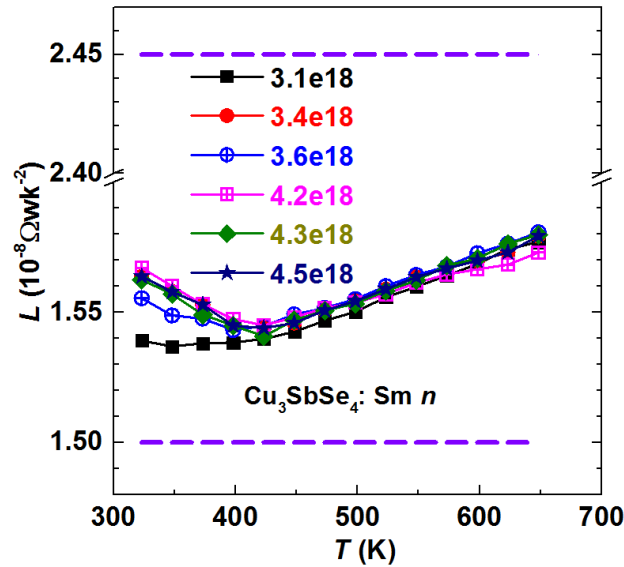
Figure 3-11. Temperature dependence of calculated Lorenz number L for the pristine and Sm-doped Cu$_3$SbSe$_4$.

The Lorenz number is evaluated by using the measured thermopower S data.[143] The calculated L values are close to the non-degenerate limit (**Figure 3-11**). The low L values thus imply a partially degenerate character in the samples. To get the thermal conductivity, we measure the thermal diffusivity from LFA and heat capacity from DSC. **Figure 3-12** shows C_p as a function of temperature for the pristine and Sm-doped Cu$_3$SbSe$_4$ from DSC. C_p of the doped samples is higher than that of the pristine sample.

The κ_L of the doped samples is lower than that of the pristine sample, mainly resulting from the enhancement of phonon scattering, as revealed in **Figure 10b**. The exponential fall is following T^{-1} relation, indicating the dominance of Umklapp phonon-phonon scattering

mechanism. For instance, κ_L of the doped sample Cu$_3$SbSe$_4$:Sm, 4.5e18 is only 0.65 W/mK at 648 K, which is about 48 % smaller than that of the pristine sample (1.25 W/mK). However, the κ_L of the doped samples is still higher than the theoretical minimum lattice thermal conductivity, κ_Lmin plotted in **Figure 10b** calculated by the Cahill's formula[22] and is found be around 0.47 W/mK from 300 K to 650 K, indicating there is still space to improve.
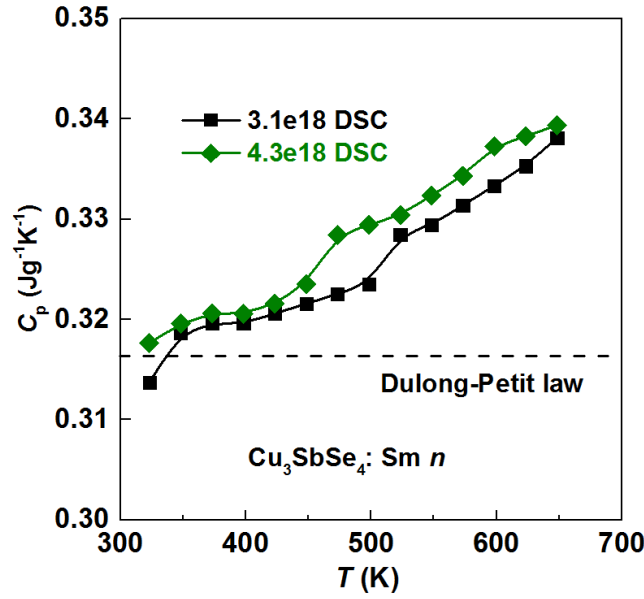
Figure 3-12. C_p as a function of temperature for the pristine and Sm-doped Cu$_3$SbSe$_4$ from DSC.

The complex interplay of phonon scattering can be valued through the Callaway model. In this model, the phonon scattering can be estimated as[144]:

$$\kappa_\text{L} = \frac{k_B}{2\pi^2 v}\left(\frac{k_B}{\hbar}\right)^3 T^3 \int_0^{\theta_D/T} \tau(x) \frac{x^4 e^x}{(e^x-1)^2}\, dx \tag{3-4}$$

where x equals $\hbar\omega/k_B T$ (ω is the phonon frequency), v the phonon velocity and θ_D the Debye temperature. The Debye model gives the relationship between Debye temperature θ_D and Debye frequency ω_D as $k_B\theta_\text{D} = \omega_\text{D}$. The phonon velocity v calculated from transverse acoustic velocities v_TA and $v_\text{TA'}$ (TA denoting a lower group velocity and TA' a higher one) and longitudinal acoustic velocity v_LA via

$$v = \left\{ \frac{1}{3} \left(\frac{1}{v_{LA}{}^3} + \frac{1}{v_{TA}{}^3} + \frac{1}{v_{TA'}{}^3} \right) \right\}^{-1/3} \qquad (3\text{-}5)$$

The Debye temperature and the phonon velocity used here are from Zhang *et al.*'s work and Qiu *et al.*'s work listed in **Table 3-3**. [77, 145]

Table 3-3. Average longitudinal acoustic velocity (LA), transverse acoustic velocity (TA/TA'), Gruneisen parameters (γTA/TA'/LA), Debye temperatures (θ_DTA/TA'/LA), and phonon velocities (vTA/TA'/LA) used in calculation from Zhang *et al.*'s work and Qiu *et al.*'s work.

Parameter	Zhang *et al.*'s work	Qiu *et al.*'s work
γ_{TA}	1.27	0.85
$\gamma_{TA'}$	1.14	0.83
γ_{LA}	1.26	1.34
θ_{DTA} (K)	60	64
$\theta_{DTA'}$ (K)	65	67
θ_{DLA} (K)	78	77
v_{TA} (m/s)	1485	1806
$v_{TA'}$ (m/s)	1699	2096
v_{LA} (m/s)	3643	3859

Thermal conductivity is limited by Umklapp phonon-phonon scattering, point defect scattering, and boundary scattering. We neglect the small contribution from the normal phonon-phonon and phonon-electron scattering interactions here. In the Matthiessen's rule,[22] the combined relaxation time τ_C can be obtained by the addition of the inverse

relaxation times for the different scattering processes, $\tau_c^{-1} = \Sigma \, \tau_i^{-1}$, in which τ_i means the phonon relaxation time of the ith scattering process.

The inverse relaxation time τ_U can be described:[146]

$$\tau_U{}^{-1} = \frac{\hbar\gamma^2\varpi^2 T}{Mv^2\theta_D}\exp(-\frac{\theta_D}{3T}) \tag{3-6}$$

where γ is the Grüneisen parameter, V volume per atom, and M the average mass. Here γ used for calculation is 1.22 and 1.01 from the references listed in **Table 3-3** respectively.[77, 145]
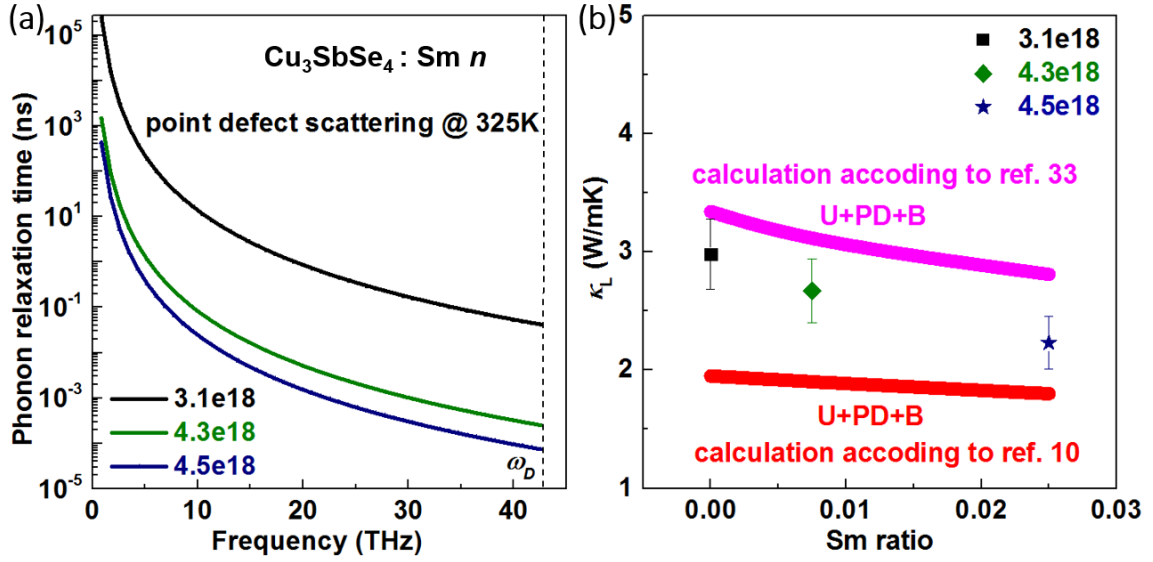
Figure 3-13. (a) Calculated phonon relaxation time versus frequency of point defect scattering at 325 K for the pristine and Sm-doped Cu₃SbSe₄ specimens. b) Comparison of experimental and calculated lattice thermal conductivities at 325 K.

Point defects scattering comes from the mass and the strain fluctuations in the crystal lattice. τ_{PD} is given by

$$\tau_{PD}{}^{-1} = \tau_M{}^{-1} + \tau_S{}^{-1} = \frac{V\varpi^4}{4\pi v^3}(\Gamma_M + \Gamma_S) \tag{3-7}$$

where Γ_M and Γ_S are the disorder scattering parameters due to mass and strain field fluctuations, respectively. The disorder scattering parameters are given by[147]

$$\frac{\kappa_L}{\kappa_L^p} = \frac{\tan^{-1} u}{u}, \ u^2 = \frac{\pi^2 \theta_D \ni}{h v^2} k_L^p (\Gamma_M + \Gamma_S) \tag{3-8}$$

where κ_L, κ_L^p, $u, \ni$ are the lattice thermal conductivity of the crystal with disorder, the lattice thermal conductivity of the crystal without disorder, the disorder scaling parameter, the average volume / atom, respectively. The calculated disorder scattering parameters for the pristine and Sm-doped Cu₃SbSe₄ specimens according to the values from Zhang *et al.*'s work and Qiu *et al.*'s work are listed in **Table 3-4**. Sm doping enhances Γ_M and Γ_S, resulting in smaller τ_{PD} shown in **Figure 3-13**.

TABLE 3-4. The calculated disorder scattering parameters for the pristine and Sm-doped Cu₃SbSe₄ specimens according to the values from Zhang *et al.*'s work and Qiu *et al.*'s work.

Parameter	According to Zhang *et al.*'s work	According to Qiu *et al.*'s work
$\Gamma_M + \Gamma_S$(3.1e18)	0	0
$\Gamma_M + \Gamma_S$(4.3e18)	0.0012(3)	0.0018(2)
$\Gamma_M + \Gamma_S$(4.5e18)	0.0040(1)	0.0059(0)

Boundary scattering can be estimated as $\tau_{BS} = d/v$, in which d is the average grain size.[148] The effect of boundary scattering may be important in polycrystal materials. In this paper, $d = 20 \pm 10$ μm is estimated from the scanning electron microscope observation, as shown in **Figure 3-14**.

Normally, the Umklapp scattering and the point defect scattering are the dominant scattering mechanism at high frequency phonons, while the boundary scattering is the

dominant mechanism at low frequencies. In this work, $\tau_{PD} \approx 7.46 \times 10^{-5}$ and 6.35×10^{-5} s at Debye frequency were obtained for the samples Cu₃SbSe₄:Sm 4.3e18 and Cu₃SbSe₄:Sm 4.5e18 through using the data from Qiu *et al.*'s work, implying that strong point defect scattering exists, shown in **Figure 3-13a**.
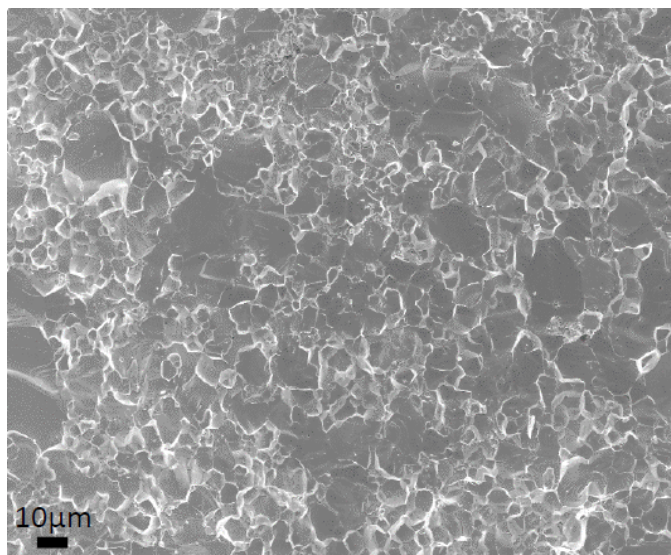
Figure 3-14. Typical scanning electron microscope image of Cu₃SbSe₄ sample.

Figure 3-13b combines thermal conductivities calculated according to the different data from Zhang *et al.*'s work and Qiu *et al.*'s work on the assumption of different scattering mechanisms (U: Umklapp scattering, PD: point defect scattering, B: boundary scattering.) with experimental values at 325 K. Umklapp scattering and the point defect scattering are the dominant collisions processes, and boundary scattering plays an important role in this temperature range as well. The calculated κ_L considering all these scattering mechanisms according to the data from Zhang *et al.*'s work is lower than the experimental values, while the calculated κ_L considering all these scattering mechanisms according to the data from Qiu *et al.*'s work is higher than the experimental values. The experimental data is just in the middle of the two calculation results. The result qualifies that the Callaway model is a useful tool to predict the thermal conductivity limitation for chalcogenide thermoelectric materials.

The zT values of all the samples are displayed in **Figure 3-1c**. As shown in this figure, at the whole temperature range, zT of all the Sm-doped samples is larger than that of the pristine sample.

3.5 Summary

A systematic combination of theory and experiment reveals that slight Sm doping in Cu_3SbSe_4 increases carrier concentration n and carrier mobility simultaneously owing to the Sm doping engaged light valence band which leads to a significantly improved PF. Furthermore, Sm doping reduces the lattice thermal conductivity via enhanced point-defect scattering of heat carrying phonons. The highest $zT \sim 1.0$ at 648 K is achieved for the sample Cu_3SbSe_4:Sm, with $n = 4.3 \times 10^{18}$ cm^{-3}, which is around 170 % larger than that of the pristine Cu_3SbSe_4 studied here.

Chapter 4 Enhanced Point Defects Scattering in $Cu_{3-x}Sm_xSbSe_{4-y}S_y$ via Sm and S Co-doping

4.1 Abstract

Doping and alloying aiming to induce point defects by mass and strain field fluctuations is an effective strategy to decrease the lattice thermal conductivity, and consequently boost the performance of thermoelectric materials. Through the Callaway model, we demonstrate that Sm and S co-doping induces strong mass differences and strain field fluctuations in Cu_3SbSe_4. The results prove that doping with proper elements can increase point defect scattering of heat-carrying phonons, leading to a lower thermal conductivity and a higher thermoelectric performance.

This work discussed in this chapter is in preparation for publication.

4.2 Introduction

For decades, the main strategy for designing the high performance thermoelectrics with low lattice thermal conductivity is the introduction of point defects or nanoprecipitates corresponding to the different scattering spectrum of heat-carrying phonons.[149, 150] Nanostructuring with the nanoscale precipitates inserted in the matrix materials can be achieved by several different approaches, such as the endotaxial nanoprecipitates[69, 76, 150-152] and dispersing nano-inclusions in the matrix.[137, 153]

Generally point defects can be obtained through doping or/and alloying. Doping or/and alloying will induce mass fluctuations related to the mass difference and strain field fluctuations related to the interatomic coupling force differences between the introduced atom and the host lattice to decrease the lattice thermal conductivity.[68, 154]

Copper chalcogenides have attracted increasing attention because of impressive thermoelectric performance and relatively low raw material costs. Cu_3SbSe_4 has a low lattice thermal conductivity and large Seebeck coefficient due to the distorted structure. Results reported by Skong $et~al.$ [78, 109] indicate that the transport properties of Cu_3SbSe_4-Cu_3SbS_4 solid solution material is noble due to the low lattice thermal conductivity. Se and S are in the same column and adjacent rows in the periodic table.

In chapter 3, we demonstrate that Sm doping in Cu position can improve the electric thermal properties greatly. Based on the low lattice thermal conductivity of Cu_3SbSe_4-Cu_3SbS_4 solid solution and the good power factor of Sm doped Cu_3SbSe_4 presented in chapter 3, we dope Cu_3SbSe_4 by two elements (Sm and S) to synthesize $Cu_{3-x}Sm_xSbSe_{4-y}S_y$ (x = 0, 0.005, 0.0075 and y = 0, 0.5, 0.1, 0.15) with respect to combine the two advantages of high power factor and low lattice thermal conductivity. This is the motivation of this work.

In this work, through S and Sm doping, we achieve a large decrease in the lattice thermal conductivity due to the increased point defects, resulting in an obviously enhanced

thermoelectric performance of Cu$_{3-x}$Sm$_x$SbSe$_{4-y}$S$_y$. The ultralow lattice thermal conductivity is understood very well through the Callaway model, and it owes to the enhanced mass fluctuation and strain field fluctuations in the co-doped samples.

4.3 Results and discussion

4.3.1 Phase constitution characterization
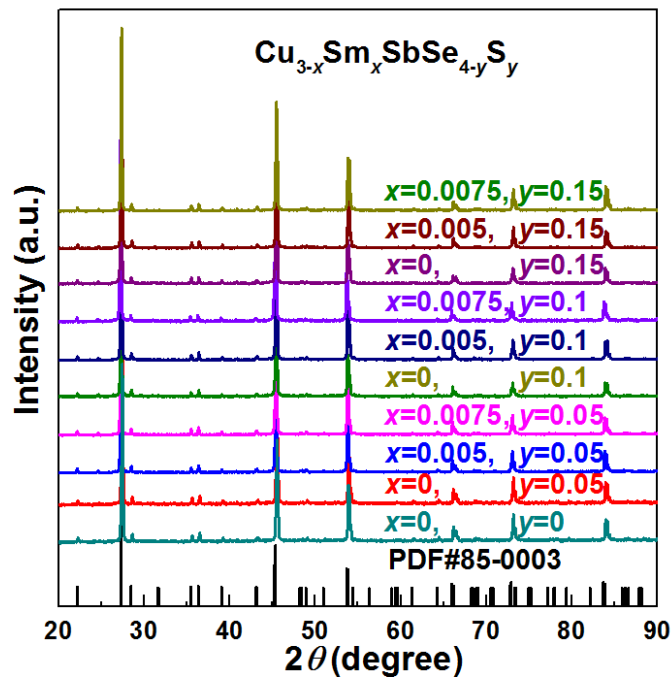
Figure 4-1. XRD patterns of Cu$_{3-x}$Sm$_x$SbSe$_{4-y}$S$_y$ (x = 0, 0.005, 0.0075 and y = 0, 0.5, 0.1, 0.15).

Phase constitutions of Cu$_{3-x}$Sm$_x$SbSe$_{4-y}$S$_y$ (x = 0, 0.005, 0.0075 and y = 0, 0.5, 0.1, 0.15) samples are investigated by XRD, and the XRD results are shown in **Figure 4-1**. All diffraction reflections can be well indexed to the tetragonal Cu$_3$SbSe$_4$ structure (standard JCPDS number: 85-0003; space group I-42m). This exhibits that no obvious impurity phases are witnessed in the produced specimens.

4.3.2 Electrical and thermal properties

Table 4-1 summarizes the nominal composition, the corresponding carrier concentration n and carrier mobility μ of the prepared $Cu_{3-x}Sm_xSbSe_{4-y}S_y$ ($x = 0$, 0.005, 0.0075 and $y = 0$, 0.5, 0.1, 0.15) samples.

Table 4-1. The nominal composition, carrier concentration n and carrier mobility μ for the samples at room temperature.

Nominal composition	n (cm^{-3})	μ (cm^{2}V^{-1}s^{-1})
Cu_3SbSe_4	3.1(2) e18	95.7(3)
$Cu_{2.995}Sm_{0.005}SbSe_4$	3.6(4) e18	116.1(2)
$Cu_{2.9925}Sm_{0.0075}SbSe_4$	4.2(5) e18	163.5(0)
$Cu_3SbSe_{3.95}S_{0.05}$	2.4(9) e18	114.1(6)
$Cu_3SbSe_{3.9}S_{0.1}$	2.0(7) e18	133.1(2)
$Cu_3SbSe_{3.85}S_{0.15}$	1.8(5) e18	125.1(7)
$Cu_{2.995}Sm_{0.005}SbSe_{3.95}S_{0.05}$	3.5(7) e18	167.6(6)
$Cu_{2.9925}Sm_{0.0075}SbSe_{3.95}S_{0.05}$	4.0(5) e18	317.0(6)
$Cu_{2.995}Sm_{0.005}SbSe_{3.9}S_{0.1}$	2.8(3) e18	44.6(2)
$Cu_{2.9925}Sm_{0.0075}SbSe_{3.9}S_{0.1}$	3.2(8) e18	54.1(3)
$Cu_{2.995}Sm_{0.005}SbSe_{3.85}S_{0.15}$	2.3(3) e18	24.9(7)
$Cu_{2.9925}Sm_{0.0075}SbSe_{3.85}S_{0.15}$	2.0(4) e18	51.2(8)
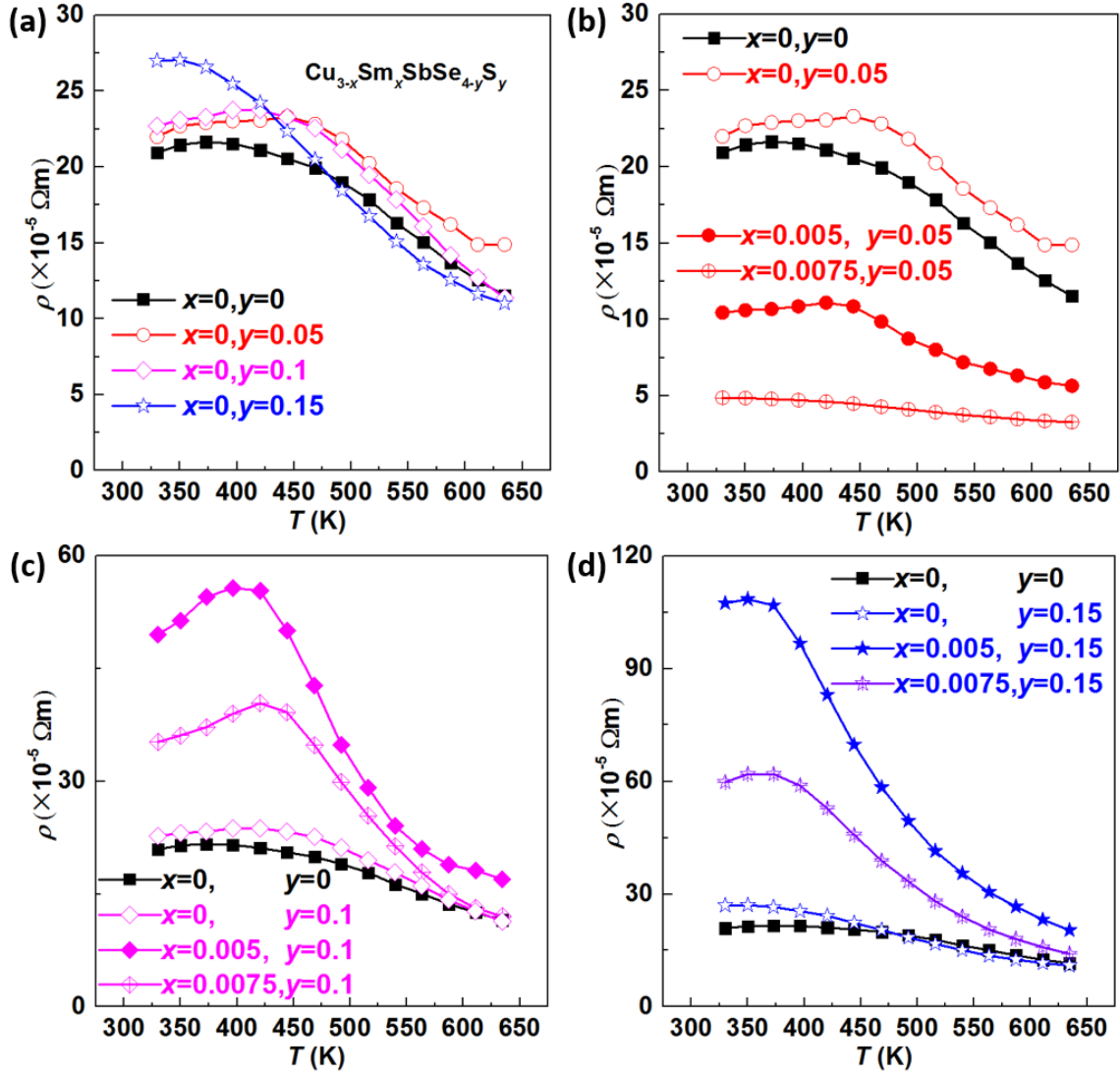
Figure 4-2. Temperature dependence of electrical resistivity of (a) Cu$_3$SbSe$_{4-y}$S$_y$ (y = 0, 0.5, 0.1, 0.15), (b) Cu$_{3-x}$Sm$_x$SbSe$_{4-y}$S$_y$ (x = 0, 0.005, 0.0075 and y = 0, 0.5), (c) Cu$_{3-x}$Sm$_x$SbSe$_{4-y}$S$_y$ (x = 0, 0.005, 0.0075 and y = 0, 0.1) and (d) Cu$_{3-x}$Sm$_x$SbSe$_{4-y}$S$_y$ (x = 0, 0.005, 0.0075 and y = 0, 0.15).

The temperature-dependent electrical resistivity is presented in **Figure 4-2**. Fitting the resistivity of pristine Cu$_3$SbSe$_4$ with the Arrhenius relation $\rho = \rho_0 \exp(E_a / \kappa_B T)$, where ρ_0, E_a and κ_B are pre-exponential factor, apparent activation energy for the conduction, and the Boltzmann constant, respectively, leads to an apparent activation energy of ~ 0.13 eV quite close to values reported in literature.[80]
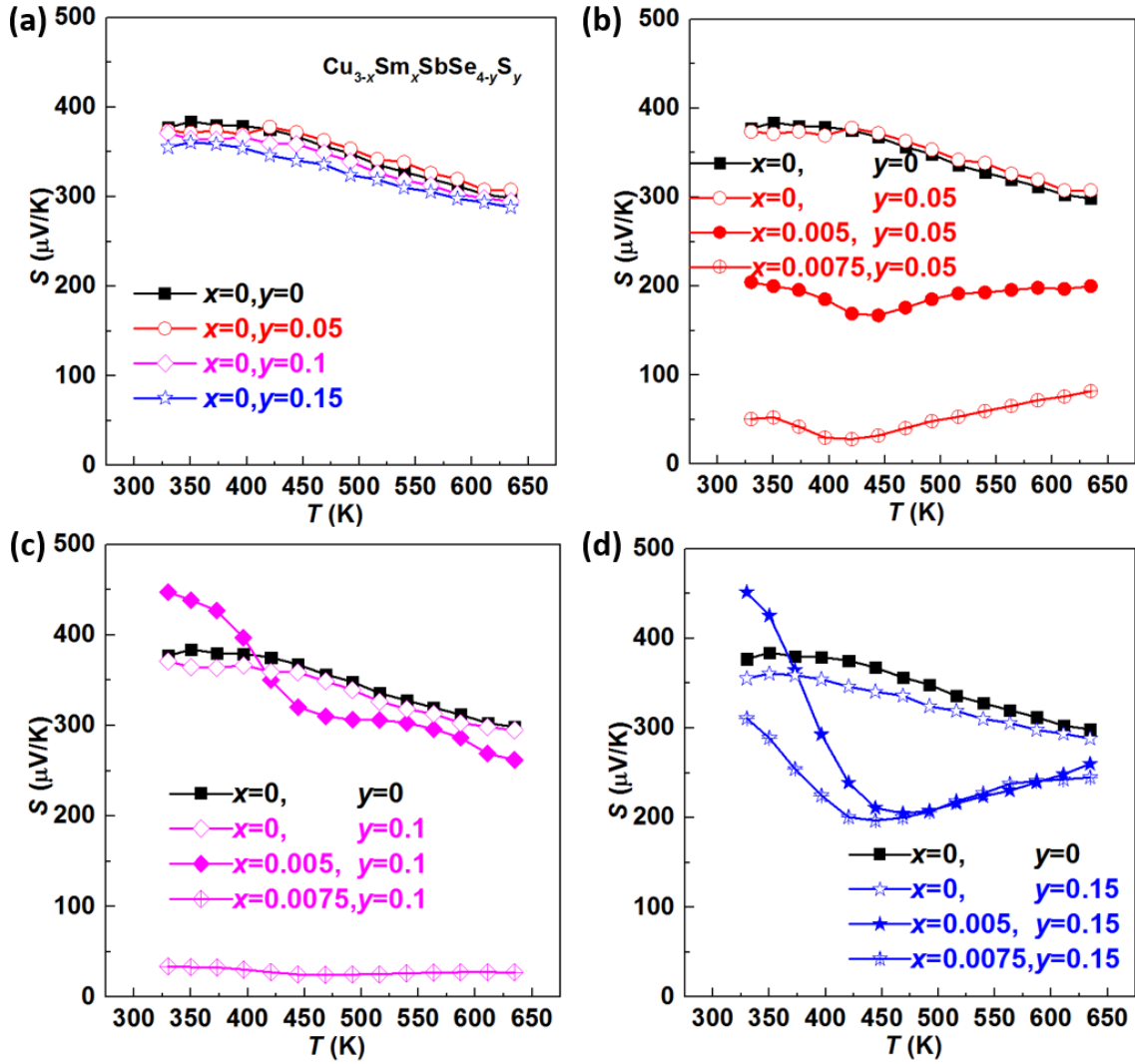
Figure 4-3. Temperature dependence of thermopower of (a) $Cu_3SbSe_{4-y}S_y$ ($y = 0, 0.5, 0.1, 0.15$), (b) $Cu_{3-x}Sm_xSbSe_{4-y}S_y$ ($x = 0, 0.005, 0.0075$ and $y = 0, 0.5$), (c) $Cu_{3-x}Sm_xSbSe_{4-y}S_y$ ($x = 0, 0.005, 0.0075$ and $y = 0, 0.1$) and (d) $Cu_{3-x}Sm_xSbSe_{4-y}S_y$ ($x = 0, 0.005, 0.0075$ and $y = 0, 0.15$).

The temperature-dependent electrical resistivity is presented in **Figure 4-2**. **Figure 4-2a** is temperature-dependent electrical resistivity for the specimens $Cu_3SbSe_{4-y}S_y$ ($y = 0, 0.5, 0.1, 0.15$). From the figure, we can notice that the electrical resistivity of the only S-doped sample is larger than that of the pristine sample. **Figure 4-2c** and **Figure 4-2d** are temperature-dependent electrical resistivity for the specimens $Cu_{3-x}Sm_xSbSe_{3.9}S_{0.1}$ and $Cu_{3-x}Sm_xSbSe_{3.85}S_{0.15}$. The electrical resistivity of high S content substituted samples is larger than that of the pristine sample. The electrical resistivity of larger Sm content substituted

$Cu_{2.927}Sm_{0.075}SbSe_{3.9}S_{0.1}$ and $Cu_{2.927}Sm_{0.075}SbSe_{3.85}S_{0.15}$ samples is smaller than that of lower Sm content substituted $Cu_{2.995}Sm_{0.005}SbSe_{3.9}S_{0.1}$ and $Cu_{2.995}Sm_{0.005}SbSe_{3.85}S_{0.15}$ samples. **Figure 4-2** is temperature-dependent electrical resistivity for the specimens $Cu_{3-x}Sm_xSe_{3.95}S_{0.05}$ ($y = 0, 0.5, 0.1, 0.15$). From the figure, we can notice that the electrical resistivity of Sm substituted samples with low S content is smaller than that of the pristine sample.

We can explain the changing of the electrical resistivity according to the changing of the carrier concentration. Shown in **Table 4-1**, the carrier concentration of the only S-doped sample is lower than that of the pristine sample, which is consistent with others' report.[109] While the carrier concentration of the only Sm-doped sample is higher than that of the pristine sample. In the co-doped samples, if the doping content of S is higher than that of Sm, the carrier concentration will be lower than that of the pristine sample, for example, $Cu_{2.995}Sm_{0.005}SbSe_{3.0}S_{1.0}$, $Cu_{2.995}Sm_{0.005}SbSe_{2.5}S_{1.5}$ and $Cu_{2.9925}Sm_{0.0075}SbSe_{2.5}S_{1.5}$. The electrical resistivity of these three samples is obviously larger than that of the pristine sample due to the lower carrier concentration.

The temperature-dependent thermopower is presented in **Figure 4-3**. The thermopower of only S-doped Cu_3SbSe_4 is quite close to that of the pristine sample. However, the thermopower of the co-doped samples is significantly different from that of the pristine sample. Shown in **Figure 4-3**, the thermopower of the co-doped samples decreases from room temperature to ~450 K, and then increases slowly with the temperature increasing.

The power factor *PF* of all the samples is presented in **Figure 4-4**. The *PF* of doped samples is not elevated compared with that of Cu_3SbSe_4 in the entire studied temperature range because of the worse performance of the electrical resistivity and thermopower.

Figure 4-4. Temperature dependence of power factor of (a) $Cu_3SbSe_{4-y}S_y$ ($y = 0, 0.5, 0.1, 0.15$), (b) $Cu_{3-x}Sm_xSbSe_{4-y}S_y$ ($x = 0, 0.005, 0.0075$ and $y = 0, 0.5$), (c) $Cu_{3-x}Sm_xSbSe_{4-y}S_y$ ($x = 0, 0.005, 0.0075$ and $y = 0, 0.1$) and (d) $Cu_{3-x}Sm_xSbSe_{4-y}S_y$ ($x = 0, 0.005, 0.0075$ and $y = 0, 0.15$).
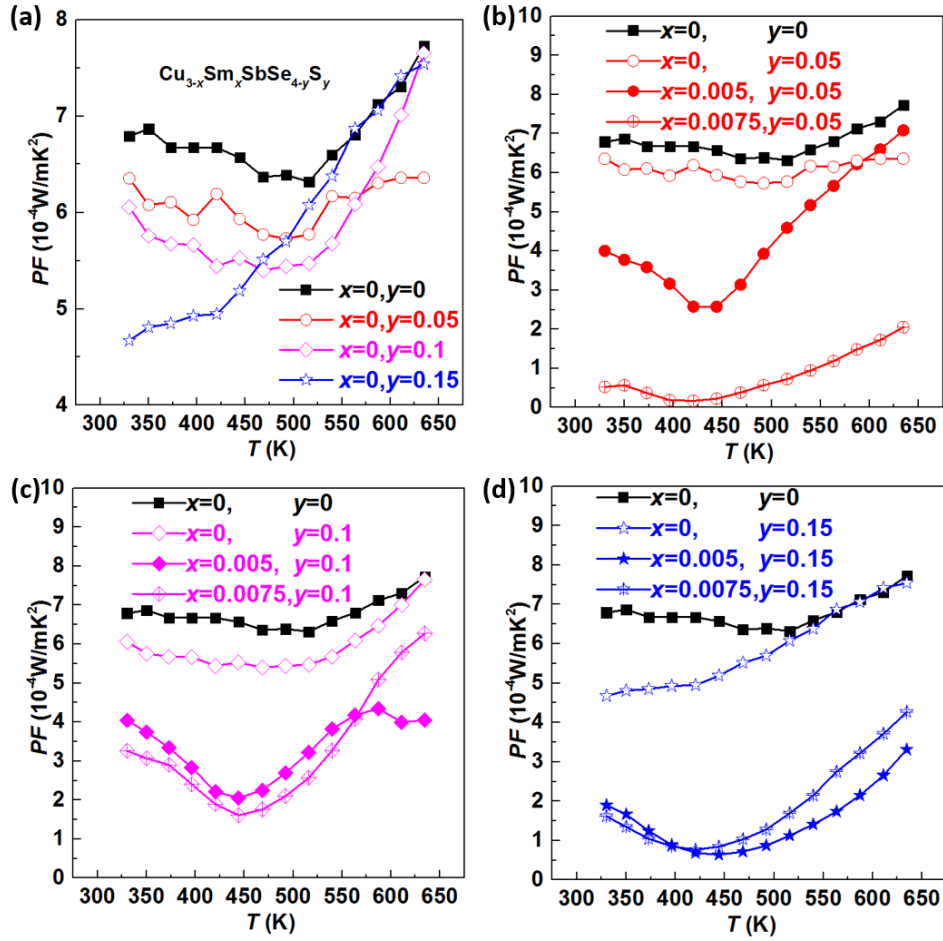
4.3.3 Ultralow lattice thermal conductivity and phonon scattering mechanisms

The temperature-dependent thermal conductivity κ is shown in **Figure 4-5a**. It can be seen that κ of all the specimens drops with increasing temperature. κ of the doped samples is lower than that of the pristine sample. The temperature-dependent thermal conductivity κ of the pristine and only S-doped samples is shown in **Figure 4-5c**. It can be seen that κ of all the S-doped samples is lower than that of the pristine sample and κ of all the S-doped specimens decreases with increasing S content.
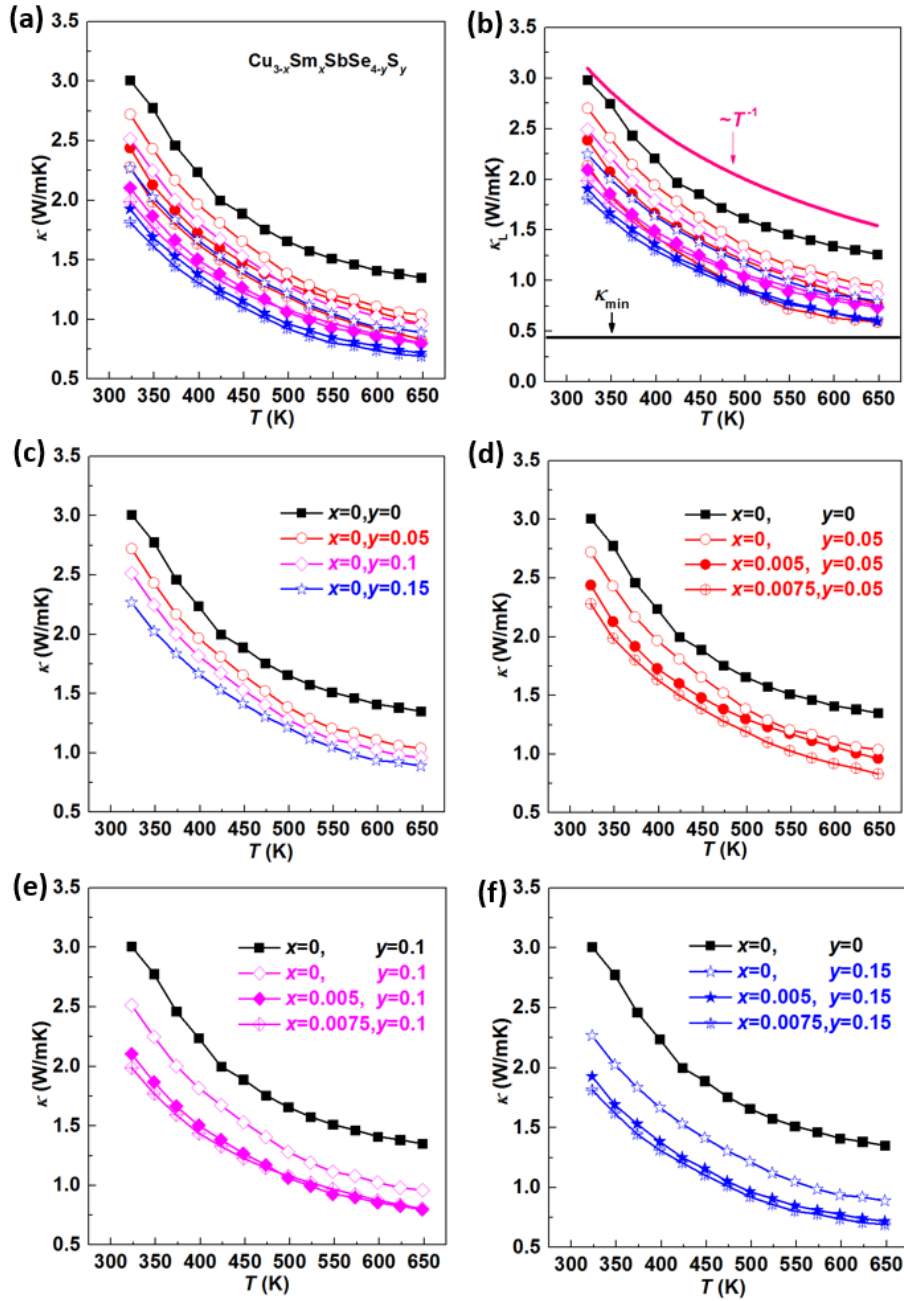
Figure 4-5. Temperature dependence of (a) total thermal conductivity and (b) lattice thermal conductivity for the pristine and doped Cu₃SbSe₄ specimens. (c) Temperature dependence of thermal conductivity for the specimens Cu₃SbSe₄₋ᵧSᵧ (y = 0, 0.5, 0.1, 0.15). (d) Temperature dependence of thermal conductivity for the specimens Cu₃₋ₓSmₓSbSe₄₋ᵧSᵧ (x = 0, 0.005, 0.0075 and y = 0, 0.5). (e) Temperature dependence of thermal conductivity for the specimens Cu₃₋ₓSmₓSbSe₄₋ᵧSᵧ (x = 0, 0.005, 0.0075 and y = 0, 0.1). (f) Temperature dependence of thermal conductivity for the specimens Cu₃₋ₓSmₓSbSe₄₋ᵧSᵧ (x = 0, 0.005, 0.0075 and y = 0, 0.15).

The temperature-dependent thermal conductivity κ is shown in **Figure 4-5a**. It can be seen that κ of all the specimens drops with increasing temperature. κ of the doped samples is lower than that of the pristine sample. The temperature-dependent thermal conductivity κ of the pristine and only S-doped samples is shown in **Figure 4-5c**. It can be seen that κ of all the S-doped samples is lower than that of the pristine sample and κ of all the S-doped specimens decreases with increasing S content.

The temperature-dependent κ of the pristine and Sm-doped $Cu_{3-x}Sm_xSbSe_{3.95}S_{0.05}$ ($x = 0$, 0.005 and 0.0075) samples is shown in **Figure 4-5d**. It can be seen that κ of all the Sm-doped $Cu_{3-x}Sm_xSbSe_{3.95}S_{0.05}$ samples is much lower than that of the pristine and $CuSbSe_{3.95}S_{0.05}$ samples, and κ of all the Sm-doped $Cu_{3-x}Sm_xSbSe_{3.95}S_{0.05}$ samples decreases with increasing Sm content. We can find the same trend in the Sm-doped $Cu_{3-x}Sm_xSbSe_{3.9}S_{0.1}$ ($x = 0$, 0.005 and 0.0075) samples and Sm-doped $Cu_{3-x}Sm_xSbSe_{3.85}S_{0.15}$ ($x = 0$, 0.005 and 0.0075) samples shown in **Figure 4-5e** and **Figure 4-5f**.

Normally, $\kappa = \kappa_L + \kappa_e$, where κ_L is the lattice thermal conductivity and κ_e is the carrier contribution. κ_e is assessed through the Wiedemann-Franz relation: $\kappa_e = L\sigma T$, where σ is the measured electrical conductivity and L is the Lorenz number. Lorenz number used is obtained by fitting the measured thermopower S data.[143] The κ_L of the doped samples is lower than that of the pristine sample, mainly resulting from the enhancement of phonon scattering, as revealed in **Figure 4-5b**. For instance, κ_L of the co-doped sample $Cu_{2.9925}Sm_{0.075}SbSe_{3.85}S_{0.15}$ is only 0.61 W/mK at 648 K, which is about 50 % smaller than that of the pristine sample. The κ_L of the Sm/S co-doped $Cu_{2.9925}Sm_{0.075}SbSe_{3.85}S_{0.15}$ sample at 648 K is very close to the theoretical minimum lattice thermal conductivity, κ_{Lmin} plotted in **Figure 4-5b** estimated through the Cahill's formula.[22]

74

We can get the phonon scattering information through the Callaway model, in which the phonon scattering can be estimated as [22, 155]:

$$\kappa = \frac{k_B}{2\pi^2 v}\left(\frac{k_B}{\hbar}\right)^3 T^3 \int_0^{\theta_D/T} \tau(x) \frac{x^4 e^x}{(e^x-1)^2} dx \qquad (4\text{-}1)$$

where x equals $\hbar\omega/k_B T$ (ω is the phonon frequency), v is the phonon velocity, θ_D is the Debye temperature and $\hbar$ is the reduced Planck constant. The Debye model gives the relationship between Debye temperature θ_D and Debye frequency ω_D as $k_B\theta_D = \omega_D$. The Debye temperature and the phonon velocity used here from Zhang $et~al.$'s work and Qiu $et~al.$'s work respectively are listed in **Table 4-2**.[77, 145]

TABLE 4-2. Average longitudinal acoustic velocity (LA), transverse acoustic velocity (TA/TA'), Gruneisen parameters (γTA/TA'/LA), Debye temperatures (θ_DTA/TA'/LA), and phonon velocities (vTA/TA'/LA) used in calculation from Zhang $et~al.$'s work and Qiu $et~al.$'s work respectively.

Parameter	Zhang $et~al.$'s work	Qiu $et~al.$'s work
γ_{TA}	1.27	0.85
$\gamma_{TA'}$	1.14	0.83
γ_{LA}	1.26	1.34
θ_{DTA} (K)	60	64
$\theta_{DTA'}$ (K)	65	67
θ_{DLA} (K)	78	77
v_{TA} (m/s)	1485	1806
$v_{TA'}$ (m/s)	1699	2096
v_{LA} (m/s)	3643	3859

According to the Matthiessen's rule,[22] the total combined relaxation time τ_C is estimated by the addition of the inverse relaxation times for the different scattering processes, $\tau_c^{-1} = \Sigma$ τ_i^{-1} , where τ_i is the phonon relaxation time in the ith scattering process. Normally above the room temperature, thermal conductivity is limited by Umklapp phonon-phonon scattering, point defect scattering and boundary scattering together. We will discuss the different scattering processes separately.
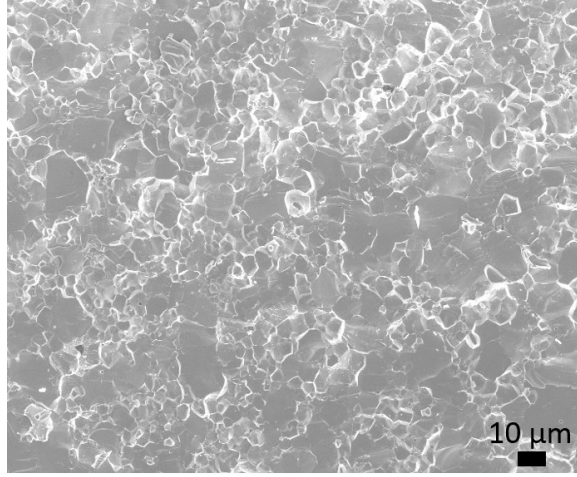
Figure 4-6. Typical scanning electron microscope image of Cu_3SbSe_4 sample.

In **Figure 4-5b**, we can see that the exponential fall follows T^{-1} relation, which means Umklapp phonon-phonon scattering mechanism is dominant. For the Umklapp phonon-phonon scattering mechanism, the inverse relaxation time τ_U can be described as:[146]

$$\tau_U^{-1} = \frac{\hbar\gamma^2\varpi^2 T}{Mv^2\theta_D}\exp(-\frac{\theta_D}{3T}) \qquad (4\text{-}2)$$

Here we choose γ in calculation 1.22 and 1.01 from Zhang *et al.*'s work and Qiu *et al.*'s work respectively listed in **Table 4-2**.[77, 145]

In the crystal lattice, point defects scattering originates from the mass difference and the strain fluctuations. For the point defects, τ_{PD} can be obtained through:

$$\tau_{PD}^{-1} = \tau_M^{-1} + \tau_S^{-1} = \frac{V\varpi^4}{4\pi v^3}(\Gamma_M + \Gamma_S) \qquad (4\text{-}3)$$

where Γ_M and Γ_S are the disorder scattering parameters due to mass difference and strain field fluctuations.[146, 147] The calculated disorder scattering parameters for the pristine and Co-doped Cu_3SbSe_4 according to the values from Zhang *et al.*'s work and Qiu *et al.*'s work are listed in **Table 4-3**.

We calculate the boundary scattering as well. The boundary scattering is estimated through $\tau_{BS} = d/v$.[148] **Figure 4-6** is the typical scanning electron microscope image of Cu_3SbSe_4 sample. From the scanning electron microscope observation, $d = 20 \pm 10$ μm is estimated.

Figure 4-7 combines thermal conductivities calculated on the assumption of different scattering mechanisms with experimental values. The calculated κ_L considering all these scattering mechanisms matches with the experimental values. The calculated κ_L considering all these scattering mechanisms according to the data from Zhang *et al.*'s work (top black line) is lower than the experimental values, while the calculated κ_L according to the data from Qiu *et al.*'s work (bottom red line) is higher than the experimental values. All experimental data is in the middle of the two calculated lines shown in **Figure 4-7**.

Figure 4-7a shows the room temperature thermal conductivities calculated via Callaway model on the assumption of combining scattering mechanisms (U, PD, and B) according to the data from Zhang *et al.*'s work. **Figure 4-7b** shows us the calculated phonon relaxation time versus frequency of point defect scattering according to from Zhang *et al.*'s work at 325 K for S-doped $Cu_3SbSe_{2.85}S_{0.15}$ and S/Sm co-doped $Cu_{2.9925}Sm_{0.0075}SbSe_{2.85}S_{0.15}$. As shown in **Figure 4-7a** and **Figure 4-7b**, considering the PD contribution, κ_L of the $Cu_3SbSe_{4-y}S_y$ ($y = 0$, 0.05, 0.1 and 0.15) samples decreases with increasing S content due to S doping induced point defect scattering, so the phonon relaxation time of S-doped $Cu_3SbSe_{2.85}S_{0.15}$ is much smaller than that of the pristine sample. Compared with the S-doped sample, in the S/Sm co-doped samples, the lattice thermal conductivity should be lower (the bottom line in **Figure4-7a**) and

the phonon relaxation time should be shorter (the bottom line in **Figure 4-7b**) due to enhanced point defect scattering by Sm doping.

TABLE 4-3. The calculated disorder scattering parameters for the pristine and Sm-doped Cu_3SbSe_4 specimens according to the values from Zhang *et al.*'s work and Qiu *et al.*'s work respectively.

Parameter ($\Gamma_M + \Gamma_S$)	According to Zhang *et al.*'s work	According to Qiu *et al.*'s work
Cu_3SbSe_4	0	0
$Cu_{2.995}Sm_{0.005}SbSe_{3.95}S_{0.0.05}$	0.0026(9)	0.0039(5)
$Cu_{2.9925}Sm_{0.075}SbSe_{3.95}S_{0.05}$	0.0046(9)	0.0069(2)
$Cu_{2.995}Sm_{0.005}SbSe_{3.9}S_{0.1}$	0.0051(3)	0.0075(5)
$Cu_{2.9925}Sm_{0.005}SbSe_{3.9}S_{0.1}$	0.0063(7)	0.0093(8)
$Cu_{2.995}Sm_{0.005}SbSe_{3.85}S_{0.15}$	0.0074(0)	0.0109(0)
$Cu_{2.9925}Sm_{0.075}SbSe_{3.85}S_{0.15}$	0.0089(7)	0.0132(1)
$Cu_3SbSe_{3.95}S_{0.05}$	0.0010(0)	0.0014(8)
$Cu_3SbSe_{3.9}S_{0.1}$	0.0020(5)	0.0030(1)
$Cu_3SbSe_{3.85}S_{0.15}$	0.0037(1)	0.0054(6)

The S content dependence of κ_L of the $Cu_3SbSe_{4-y}S_y$ ($y = 0$, 0.05, 0.1 and 0.15) samples and Sm content dependence of κ_L of $Cu_{3-x}Sm_xSbSe_{3.85}S_{0.15}$ ($x = 0$, 0.005, and 0.0075) samples are shown in **Figure 4-7c** and **Figure 4-7d**.
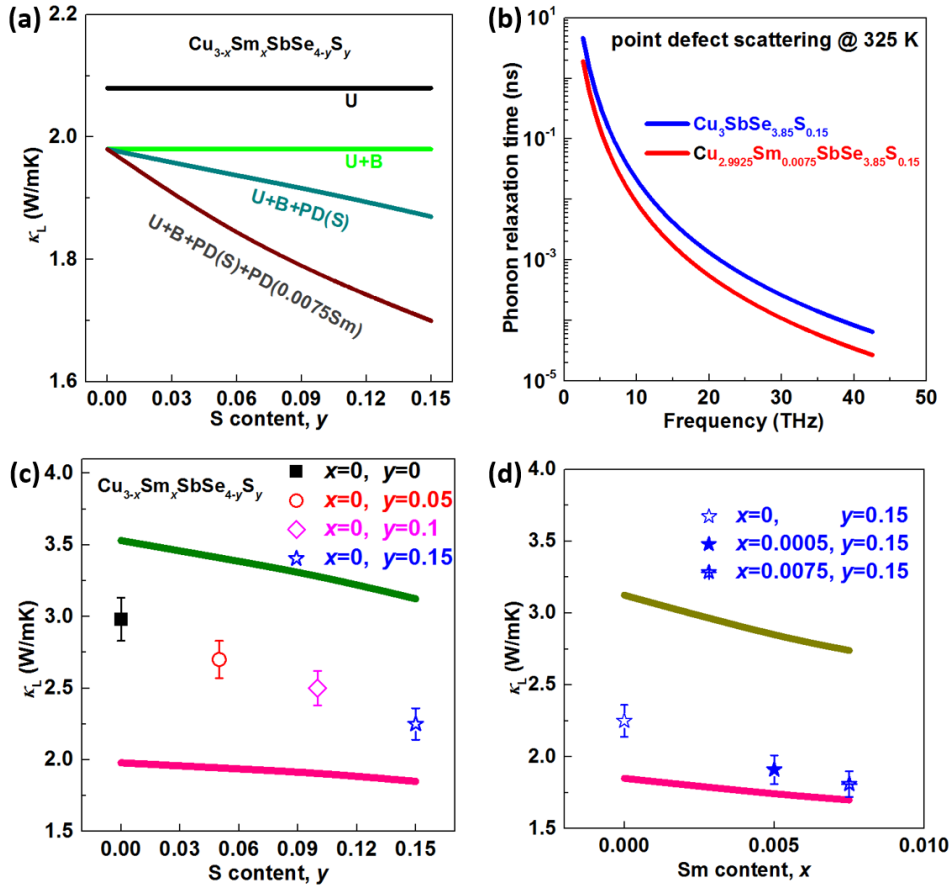
Figure 4-7. (a) Calculated lattice thermal conductivities on the assumption of different scattering mechanisms (U: Umklapp scattering, PD: point defect scattering, B: boundary scattering) for the specimens at 325 K according to reference 21. (b) Calculated phonon relaxation time versus frequency of point defect scattering according to reference 21 at 325 K for S-doped $Cu_3SbSe_{2.85}S_{0.15}$ and co-doped $Cu_{2.9925}Sm_{0.0075}SbSe_{2.85}S_{0.15}$. (c) Comparison of experimental and calculated lattice thermal conductivities for the specimens $Cu_3SbSe_{4-y}S_y$ ($y = 0$, 0.5, 0.1, 0.15) at 325 K. (d) Comparison of experimental and calculated lattice thermal conductivities for the specimens $Cu_{3-x}Sm_xSbSe_{4-y}S_y$ ($x = 0$, 0.005, 0.0075 and $y = 0.15$) at 325 K.

The experimental results are located between the top green line calculated according to the data from Zhang *et al.*'s work and the bottom pink line calculated according to the data from Qiu *et al.*'s work respectively. The experimental data does not match very well with both calculated results. One possible reason could be that the Debye temperature and sound velocity of as-prepared samples are different from these in Zhang *et al.*'s work and Qiu *et*

al.'s work. Nevertheless, the doping content dependence of κ_L for both experimental results and calculations is similar. It can be seen that κ_L of the $Cu_3SbSe_{4-y}S_y$ (y = 0, 0.05, 0.1 and 0.15) samples decreases with increasing S content due to the point defects contribution. We can find the same trend in Sm-doped $Cu_{3-x}Sm_xSbSe_{3.85}S_{0.15}$ (x = 0, 0.005, and 0.0075) samples.
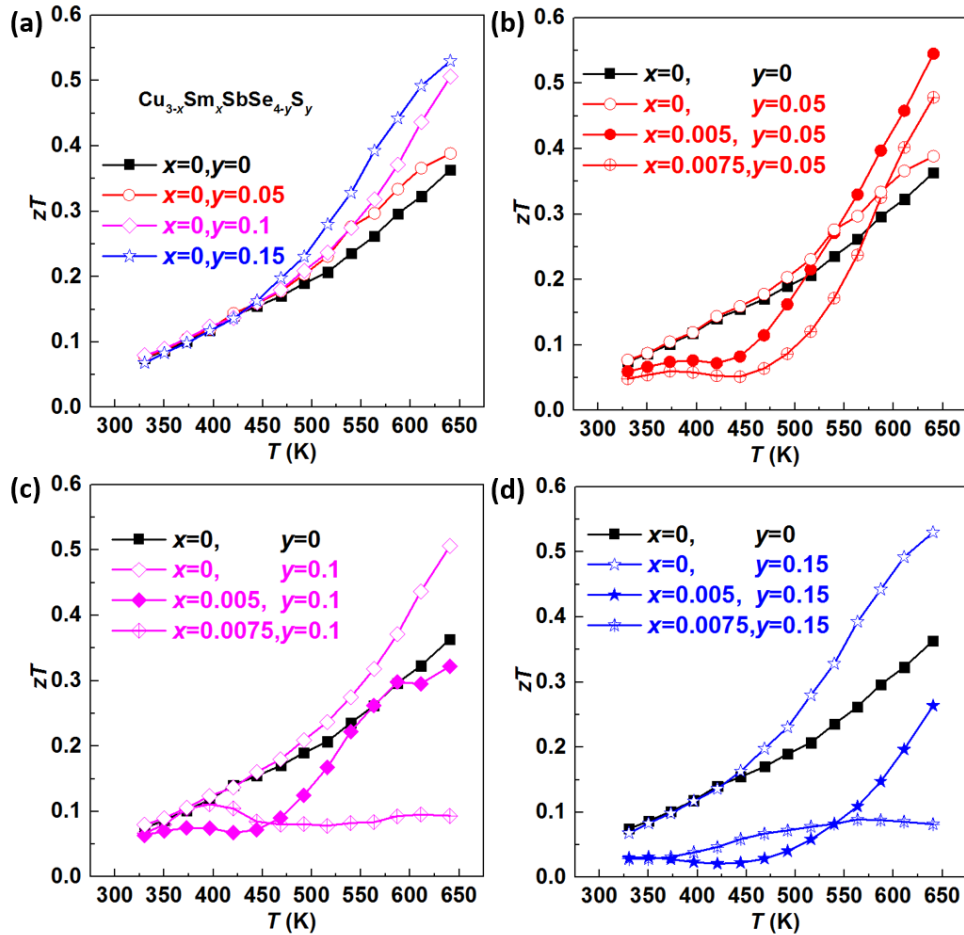
Figure 4-8. Temperature dependence of zT of (a) $Cu_3SbSe_{4-y}S_y$ (y = 0, 0.5, 0.1, 0.15), (b) $Cu_{3-x}Sm_xSbSe_{4-y}S_y$ (x = 0, 0.005, 0.0075 and y = 0, 0.5), (c) $Cu_{3-x}Sm_xSbSe_{4-y}S_y$ (x = 0, 0.005, 0.0075 and y = 0, 0.1) and (d) $Cu_{3-x}Sm_xSbSe_{4-y}S_y$ (x = 0, 0.005, 0.0075 and y = 0, 0.15).

The zT values of all samples are displayed in **Figure 4-8**. Although the PF values of doped samples are lower than that of pristine Cu_3SbSe_4, the zT values of most of the doped samples are higher than that of pristine Cu_3SbSe_4 due to the fact that S and/or Sm doping increases point defect scattering. Specifically, zT = 0.55 is obtained at 648 K for

$Cu_{2.995}Sm_{0.005}SbSe_{3.95}S_{0.05}$, amounting to a 55% increase compared to the pristine Cu_3SbSe_4 studied here.

4.4 Summary

The thermoelectric properties of $Cu_{3-x}Sm_xSbSe_{4-y}S_y$ ($x = 0$, 0.005, 0.0075 and $y = 0$, 0.5, 0.1, 0.15) are studied in the temperature range $300\,K < T < 650\,K$. The thermoelectric performance is increased as a result of a drastic reduction in the thermal conductivity attributed to an enhanced point-defect scattering of heat carrying phonons. Sm doping introduces additional mass and strain field fluctuations further reducing the low lattice thermal conductivity of the S-doped samples. As a result, we have attained a zT of ~0.55 at 648 K for $Cu_{2.995}Sm_{0.005}SbSe_{3.95}S_{0.05}$, which corresponds to an almost 55 % increase compared to the zT of the pristine Cu_3SbSe_4 studied here.

Chapter 5 Extraordinary Role of Cu in Enhancing the Thermoelectric Performance of n-type Half-Heusler

5.1 Abstract

Thermoelectric materials offer a promising solution of converting waste heat to the electrical power directly. Both high operating temperature and high figure of merit zT are desirable for high-efficiency thermoelectric power generation. Here we report a zT of ~1.3 at 875 K for the n-type $Zr_{0.4}Hf_{0.6}NiSn$ half-Heusler alloys. In the half-Heusler / full-Heusler nanocomposites, nanophase full-Heusler simultaneously optimizes the power factor and suppresses the thermal conductivity.

5.2 Introduction

Thermoelectric materials, which can directly convert waste heat into electricity, have received attention for promising application in energy harvesting. The conversion efficiency η of a thermoelectric device is limited by the Carnot efficiency η_c, and the figure of merit zT, $zT = S^2T/\rho(\kappa_e + \kappa_L)$, where S, ρ, T, κ_e and κ_L are the Seebeck coefficient, the electrical resistivity, the absolute temperature and the electronic and lattice thermal conductivity. However, the parameters ρ, S, and κ_e are interrelated.[125] Two main strategies have been adopted to decouple the thermal and electrical properties. One is to maximize the power factor through tuning carrier concentration and band engineering.[36, 37, 156] The other is to reduce the lattice thermal conductivity κ_L by nanostructuring.[65, 69, 157, 158]

The half-Heusler compounds have attracted more and more attentions due to their good electrical and mechanical properties as well as thermal stability at high temperatures.[76, 159] Makongo *et al.*[105] and Chai *et al.*[106, 107] use excess Ni in the Ni position to form the half-Heusler / full-Heusler (HH / FH) compounds, resulting in improving the thermoelectric performance. Besides, Cu, as the nearest neighbor of Ni in periodic table, is an effective dopant to adjust carrier concentration of ZrNiSn based half-Heusler compounds.[160] In consideration of the above results, Cu is chosen as excess metal in our investigated half-Heusler compound to achieve the HH / FH nanocomposites as well, which could be an effective strategy for simultaneously optimizing the power factor and reducing thermal conductivity. In nanostructured HH / FH thermoelectric materials, as the carrier concentration of full-Heusler is much higher than that of the half-Heusler, carriers in the full-Heusler nanoparticles will inject into the half-Heusler matrix (**Figures 5-1a, b**) to optimize power factor. Further scattering for phonons between the full-Heusler nanoprecipitates and half-Heusler matrix will be increased greatly, and results in reduced k_L (**Figure 5-1c**).
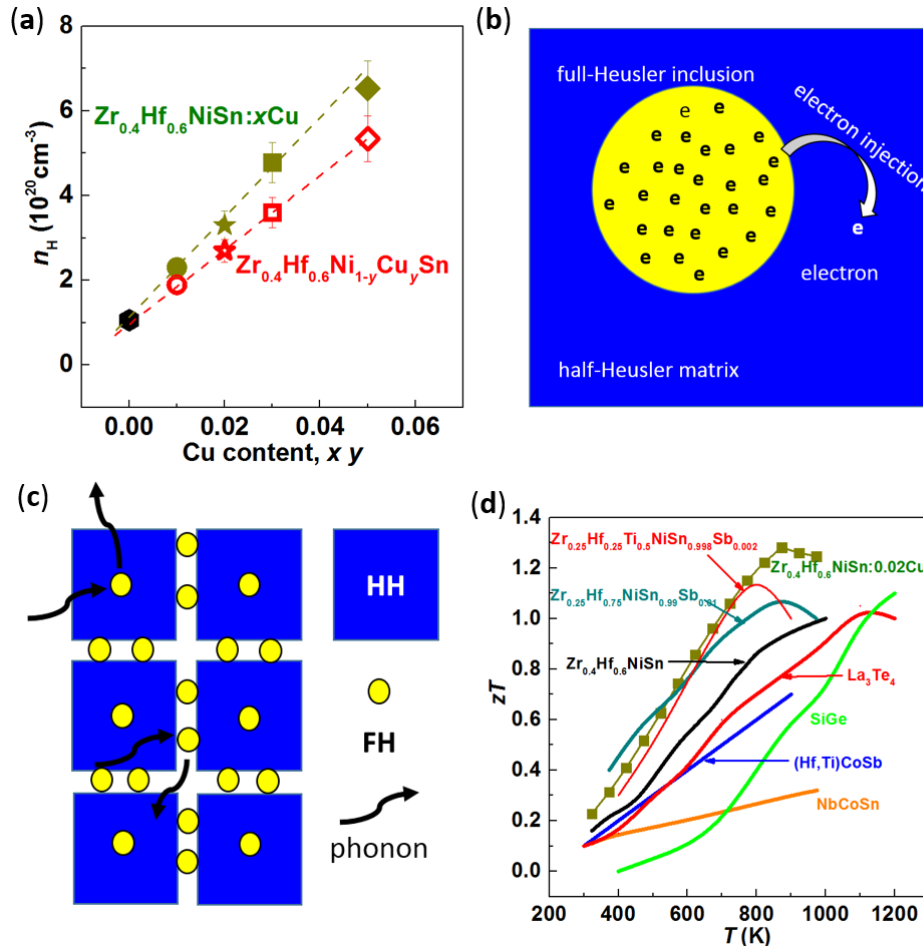
Figure 5-1. (a) Cu content dependence of carrier concentration of $Zr_{0.4}Hf_{0.6}NiSn:xCu$ and $Zr_{0.4}Hf_{0.6}Ni_{1-y}Cu_ySn$. (b) The schematic diagram shows carriers of the full-Heusler nanoparticles inject into the half-Heusler matrix. (c) The schematic diagram shows the full-Heusler nanoparticles in the half-Heusler matrix. (d) Temperature dependence of the figure of merit zT comparison of the typical high temperature materials. N-type half-Heusler compounds are comparable to the other advanced high temperature materials.

Here we demonstrate that the thermoelectric properties of n-type $Zr_{0.4}Hf_{0.6}NiSn$ half-Heusler compound can be significantly enhanced through forming the full-Heusler nanocomposites. **Figure 5-1d** shows the zT values of these samples. A peak zT of ~1.3 is reached at 875 K for $Zr_{0.4}Hf_{0.6}NiSn:2\%Cu$, which is ~100% higher than that of the pristine sample, and the zTs are remarkably higher than other well-known state-of-the-art n-type high-temperature thermoelectric materials over the whole temperature range.[100, 101, 103, 104,

161-163] As is well known, the average zT_{avg} is more important than the peak zT for thermoelectric device application. The zT_{avg} of $Zr_{0.4}Hf_{0.6}NiSn:2\%Cu$ sample is calculated to be ~0.7 and ~0.9 in the temperature range of 300 – 900 K and 500 – 900 K, respectively.

5.3 Results and discussion

5.3.1 Phase identification and Microstructure analysis.

Table 5-1. The nominal composition and carrier concentration at room temperature for the samples.

Nominal composition	carrier concentration (cm^{-3})
$Zr_{0.4}Hf_{0.6}NiSn$	1.0(6) e20
$Zr_{0.4}Hf_{0.6}NiSn:0.01Cu$	2.3(0) e20
$Zr_{0.4}Hf_{0.6}NiSn:0.02Cu$	3.3(0) e20
$Zr_{0.4}Hf_{0.6}NiSn:0.03Cu$	4.7(8) e20
$Zr_{0.4}Hf_{0.6}NiSn:0.05Cu$	6.5(3) e20
$Zr_{0.4}Hf_{0.6}Ni_{0.99}Cu_{0.01}Sn$	1.8(9) e20
$Zr_{0.4}Hf_{0.6}Ni_{0.98}Cu_{0.02}Sn$	2.7(2) e20
$Zr_{0.4}Hf_{0.61}Ni_{0.97}Cu_{0.03}Sn$	3.6(0) e20

Table 5-1 summarizes the nominal composition and carrier concentration of as prepared $Zr_{0.4}Hf_{0.6}NiSn:xCu$ and $Zr_{0.4}Hf_{0.6}Ni_{1-y}Cu_ySn$ samples. High-quality $Zr_{0.4}Hf_{0.6}NiSn:xCu$ and $Zr_{0.4}Hf_{0.6}Ni_{1-y}Cu_ySn$ compounds are fabricated by arc melting and spark plasma sintering. The XRD patterns of $Zr_{0.4}Hf_{0.6}NiSn:xCu$ after arc melting (**Figure 5-2a**) show a single phase that can be indexed to the half-Heusler phase with a cubic MgAgAs-type crystal structure. The XRD patterns of $Zr_{0.4}Hf_{0.6}NiSn:xCu$ after one week annealing are shown in **Figure 5-2b**. As comparison, the XRD patterns of Cu-doped $Zr_{0.4}Hf_{0.6}Ni_{1-y}Cu_ySn$ after arc melting and after annealing are shown in **Figure 5-3**, in which the XRD patterns both after arc melting and after one week annealing show a single phase that can be indexed to the half-Heusler phase with a cubic MgAgAs-type crystal structure.
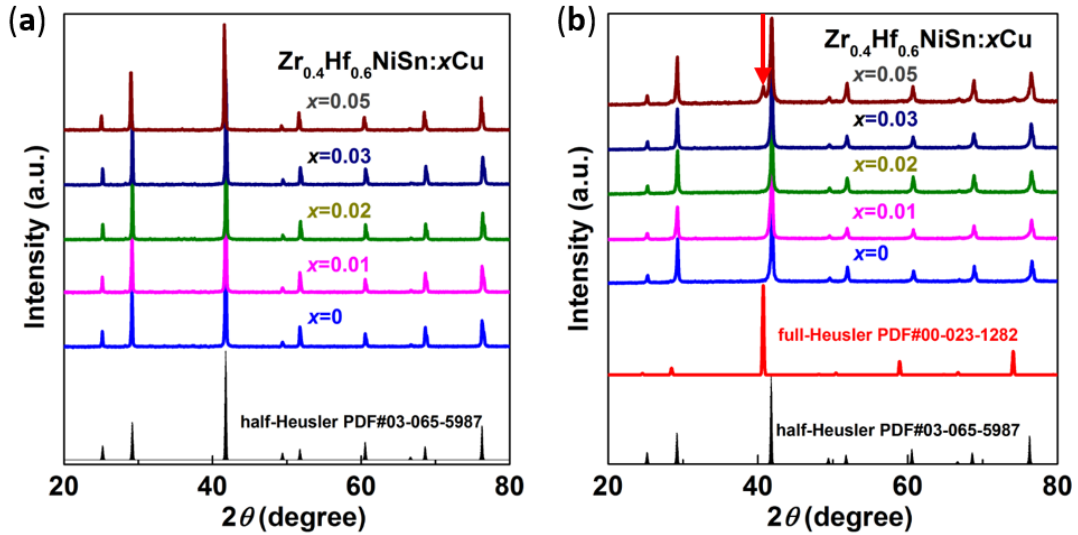
Figure 5-2. (a) XRD patterns of the samples $Zr_{0.4}Hf_{0.6}NiSn:x$Cu after arc melting. (b) XRD patterns of the samples $Zr_{0.4}Hf_{0.6}NiSn:x$Cu after arc melting and annealing.
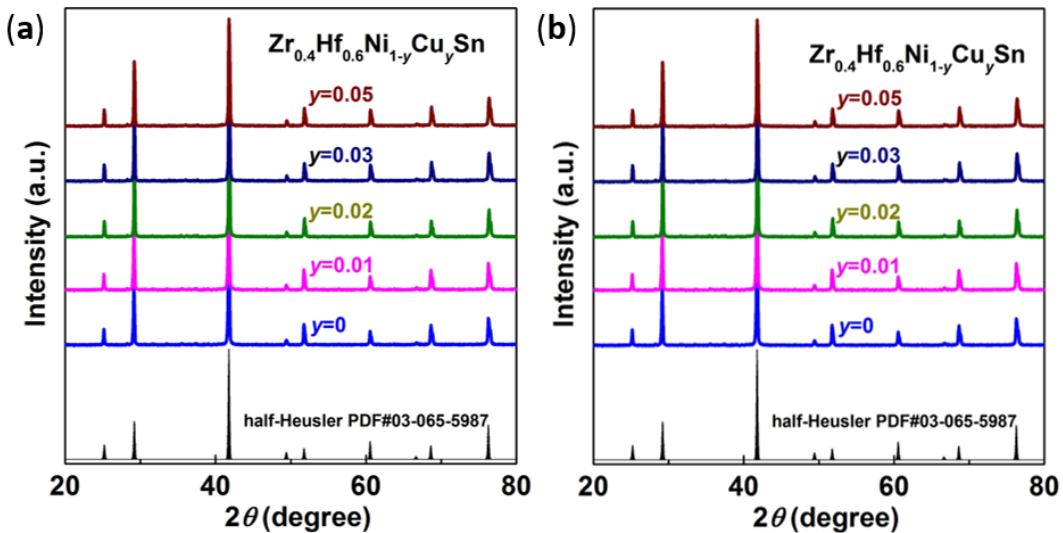
Figure 5-3. XRD patterns of the samples $Zr_{0.4}Hf_{0.6}Ni_{1-y}Cu_ySn$ (a) after arc melting and (b) after arc melting and one week annealing.

Moreover, in XRD patterns of $Zr_{0.4}Hf_{0.6}NiSn:5\%Cu$ other than reflections from half-Heusler, there is an additional small reflection at $2\theta \sim 41.5°$ that corresponds to the reflection of full-Heusler phase, indicating that there is full-Heusler forming in the matrix. For lower content, however, conclusive phase identification is unsatisfactory because of overlapping of

the x-ray interaction volumes of the nanoparticles and surrounding HH matrix. Therefore, further phase characterization of the nanoparticles is carried out using high-resolution TEM (**Figure 5-4**).
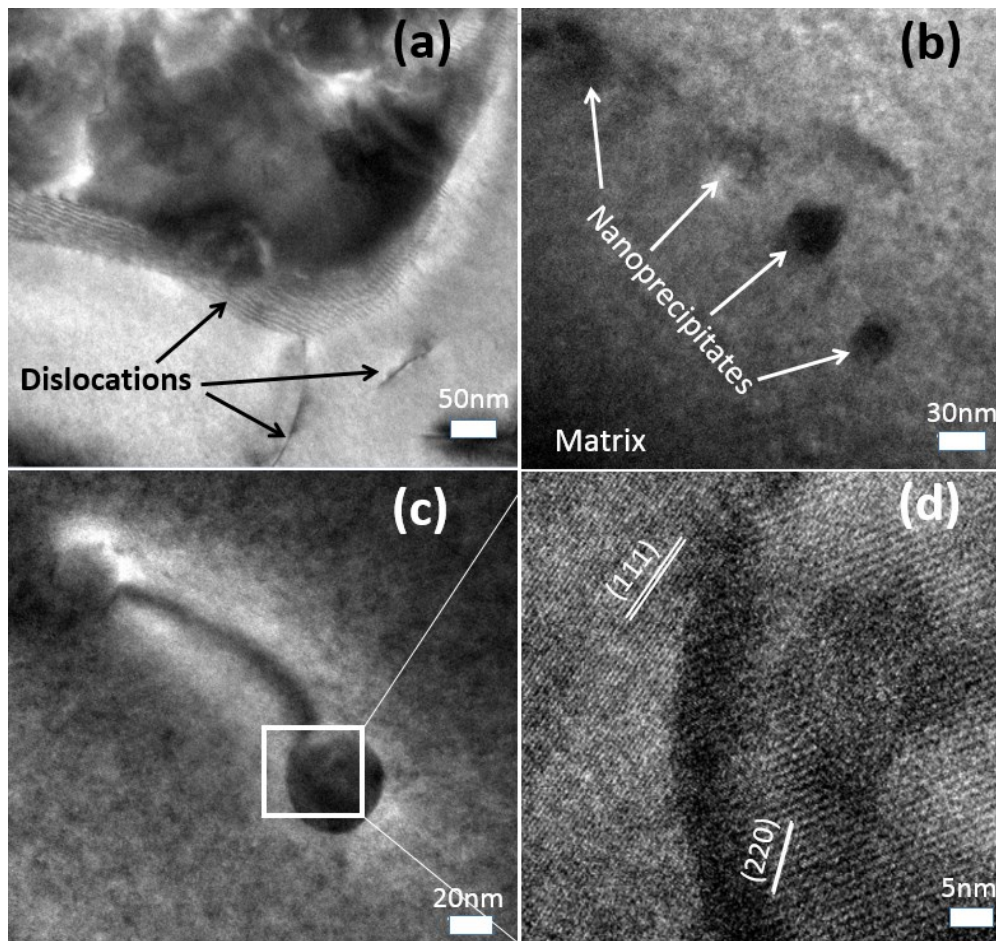
Figure 5-4. Bright field TEM images of a) some dislocations b)c)nano precipitates in $Zr_{0.4}Hf_{0.6}NiSn:0.02Cu$ after one week annealing. (d) The enlarged HRTEM picture of the corresponding square area in (c).

HRTEM analysis is carried out to characterize the sample $Zr_{0.4}Hf_{0.6}NiSn:0.02Cu$ in which nanoprecipitates may exert a significant influence on the thermoelectric performance, as depicted in **Figure 5-4**. From **Figure 5-4 a**, it is obvious that there are some dislocations in the matrix, which can strengthen the phonon scattering. **Figure 5-4 b** and **Figure 5-4 c** show some fine nanoparticles with sizes of around 20 nm in the matrix.

In **Figure 5-4 d**, the calculated interplanar distances of this region are 0.35 nm and 0.23 nm, which are consistent with interplanar spacing of the $(111)_{HH}$ and $(220)_{FH}$, respectively. The presence of FH nanoprecipitates and dislocations can provide a large number of scattering centers for phonons, which is responsible for the significantly low κ_L.
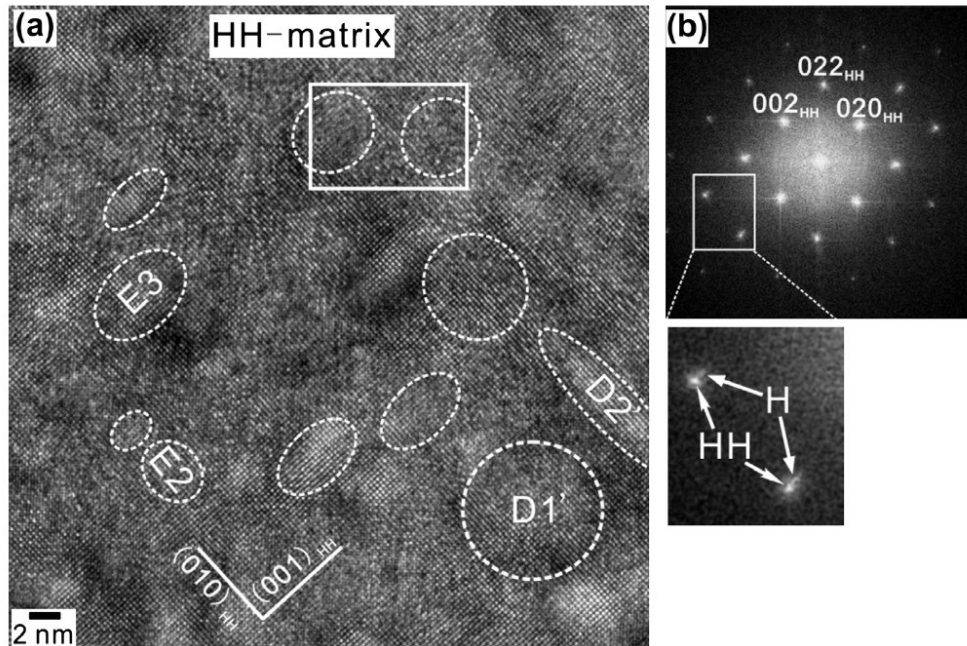
Figure 5-5. (a) HRTEM image depicting the lattice structure of the nanoparticles. Some of the nanoparticles have been highlighted by dashed lines. (b) Corresponding [1 0 0] half-Heusler fast-Fourier transform (FFT) diffraction pattern of (a). The inset shows enlarged diffraction spots from the half-Heusler matrix and Heusler phase nanoparticles.[164]

The microstructures of TiNiSn half-Heusler alloys with excess Ni have been studied by Chai *et al*.[164] In their work, they found full-Heusler nanoparticles are coherent with the half-Heusler matrix shown in **Figure 5-5**. Through the fast Fourier transform (FFT) image presented in **Figure 5-5b**, the enlarged inset reveals that there is splitting phenomenon originating from the full-Heusler nanoparticles due to the fact that the full-Heusler nanoparticles have a slightly larger lattice size than that of the half-Heusler matrix.
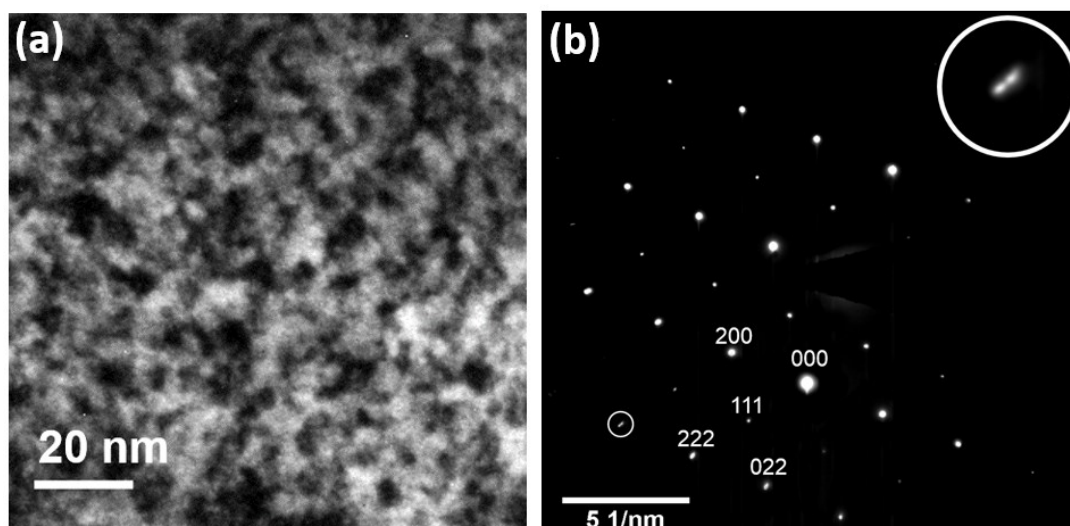
Figure 5-6. (a) Bright field TEM image of the $Zr_{0.4}Hf_{0.6}NiSn:0.02Cu$ sample. (b) Half-Heusler diffraction pattern of (a). The inset on the upright corner displays enlarged splitted diffraction spots.

In our experiment, we also observe the same phenomenon. **Figure 5-6a** is bright field TEM image showing the nanoprecipitates in the $Zr_{0.4}Hf_{0.6}NiSn:0.02Cu$ sample. The diffraction pattern along the [0 -1 1] zone axis of **Figure 5-6a** is presented in **Figure 5-6b**. The enlarged inset splitting pattern is shown in the upright corner of **Figure 5-6b** as well. The splitting pattern originates from the different lattice sizes between the full-Heusler nanoparticles and the half-Heusler matrix.

5.3.2 Decoupling of electrical and thermal properties.

To fit the parameters, we test the low temperature thermoelectric performance of the pristine sample as well, as shown in **Figure 5-7** and **Figure 5-8**. In these figures, the black line is the low temperature data from PPMS and the red line is the high temperature data from ZEM. The results of low temperature measurements roughly match with these of the high temperature measurements. The electric resistivity (shown in **Figure 5-7a**) and Seebeck coefficient (shown in **Figure 5-7b**) decrease with the temperature increases during the whole measurement range while the thermal conductivity (**Figure 5-8**) of the sample increases with a temperature increases up to ~50 K and then it decreases with the temperature increasing in the sample $Zr_{0.4}Hf_{0.6}NiSn$.

90
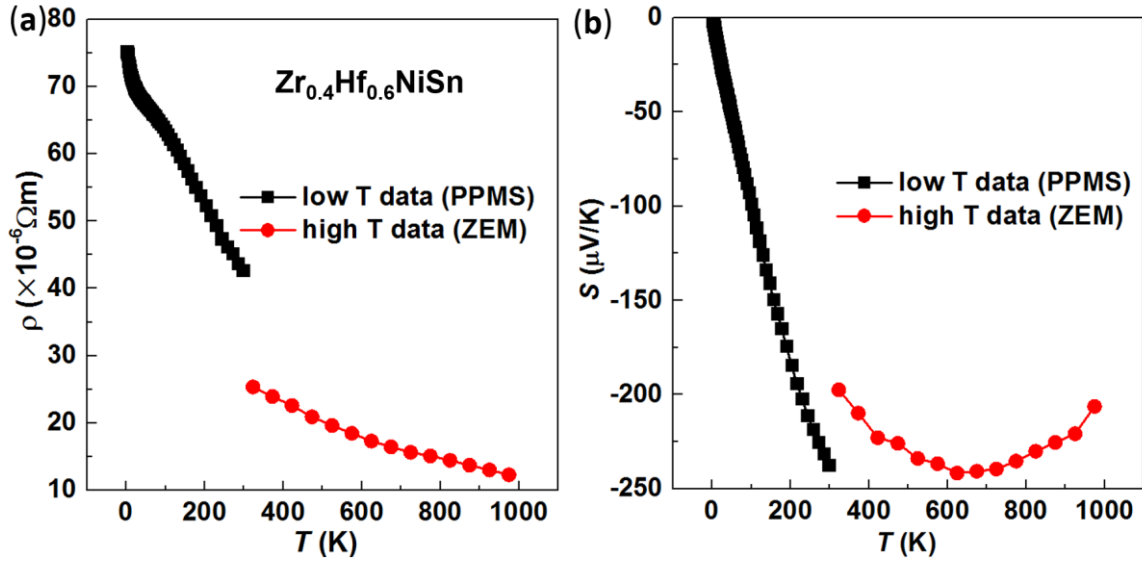
Figure 5-7. The electric resistivity (a) and Seebeck coefficient (b) of the pristine sample as a function of temperature.
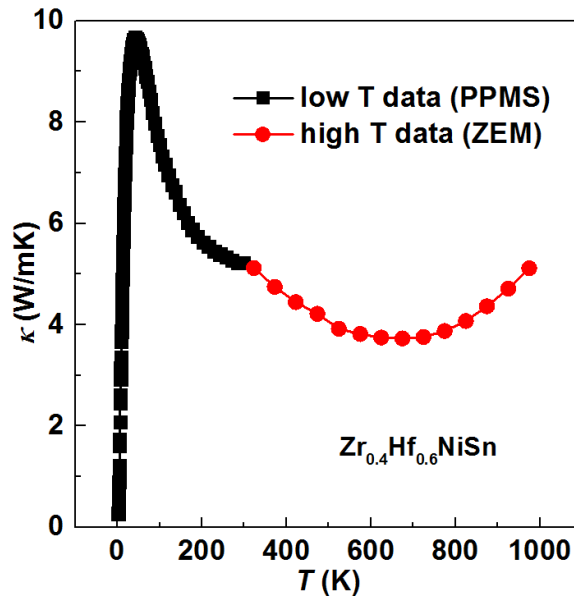
Figure 5-8. The thermal conductivity as a function of temperature of the sample $Zr_{0.4}Hf_{0.6}NiSn$.

In principle, the temperature-dependent resistivity gives us more information about the transport properties. To explain the resistivity behavior of the pristine sample, we need three different electrical conduction mechanisms.
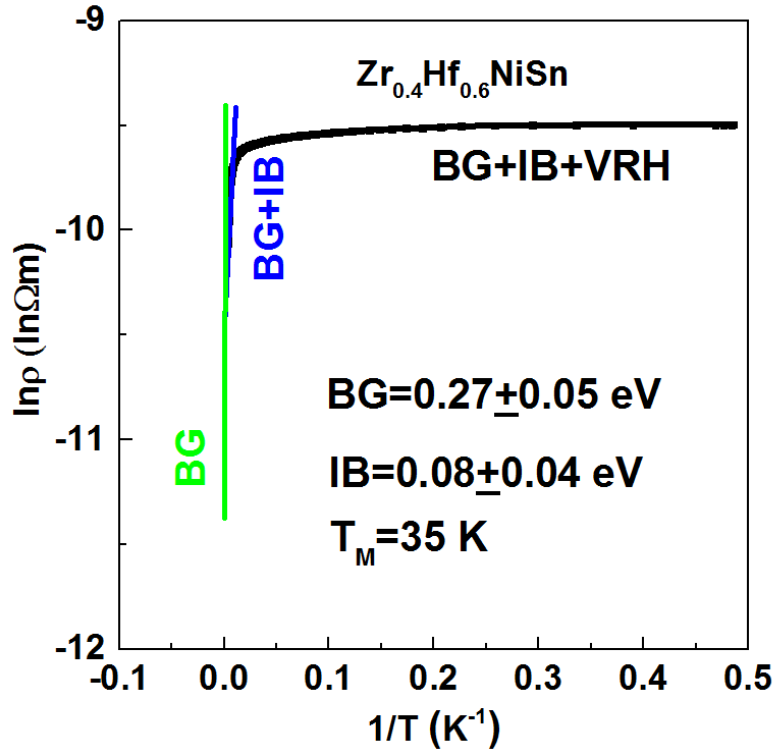
Figure 5-9. Arrhenius plot for the Zr$_{0.4}$Hf$_{0.6}$NiSn sample and numerical fit through combinations of three different conduction models: BG (energy band gap), IB (impurity band) and VRH (variable range hoping).

In the first model, there will be thermally activated conduction over an energy band gap (BG). In this model, the resistivity is characterized by the Arrhenius equation:

$$\frac{1}{\rho} = \sigma_0 \exp(-\frac{\Delta E_0}{2k_B T}) \tag{5-1}$$

where ΔE_0 means a thermal band gap, σ_0 a pre-exponential factor, and k_B the Boltzmann constant.

Normally this model is useful for the fitting during the high temperature range. As shown by the green line labeled as BG in **Figure 5-10**, the resistivity of the sample Zr$_{0.4}$Hf$_{0.6}$NiSn is described well at high temperature, while when in the temperature range $T < 550$ K, the BG model does not work anymore.

Then we need a more precise model to explain the resistivity in the temperature range $T <$ 550 K. In this model, it assumes that there is an impurity band (IB) in the band gap,

$$\frac{1}{\rho} = \sigma_0 \exp\left(-\frac{\Delta E_0}{2k_BT}\right) + \sigma_1 \exp\left(-\frac{\Delta E_1}{2k_BT}\right) \tag{5-2}$$

where ΔE_1 means an impurity activation energy and σ_1 is pre-exponential factor. In our experiment, the second model works in the temperature range 40 K $< T <$ 550 K. The fitting data labeled as BG + IB using this model is shown by the blue line in **Figure 5-10**.

In the temperature range $T <$ 40 K, to have a better description for the resistivity, we need to consider the variable range hoping (VRH) mechanism. The equation of the BG + IB + VRH model is following:

$$\frac{1}{\rho} = \sigma_0 \exp\left(-\frac{\Delta E_0}{2k_BT}\right) + \sigma_1 \exp\left(-\frac{\Delta E_1}{2k_BT}\right) + \sigma_M \exp\left[-\left(\frac{T_M}{T}\right)^{\frac{1}{4}}\right] \tag{5-3}$$

where T_M is the Mott temperature related to localization energy and σ_M is a pre-exponential factor. The BG + IB + VRH line is shown in **Figure 5-10**. The variable range hoping is related to the charge carrier localization at low temperature range. Normally at low temperatures VRH originates from a smaller overlap of the electron wave functions of impurity atoms when there is an impurity band. In our experiment, a $T_M = 35$ K is obtained. In others' works, $T_M = 87$ K for NbFeSb,[165] $T_M = 0.6$ K for YPdSb,[166] $T_M = 0.26$ K for TbNiSb,[167] $T_M = 0.24$ K for HoNiSb[167] and $T_M = 17$ K for $Zr_{0.3}Hf_{0.7}NiSn$[168] are reported.

Low temperature Hall carrier concentrations of the samples are shown in **Figure 5-10**. In **Figure 5-10**, we notice an interesting phenomenon: in the low temperature range $0 < T < 300$ K, carrier concentration of the excess Cu sample is independent of the temperature while that of the pristine sample is dependent of temperature. For the Cu-excess samples, all of them show metallic-like transport behavior in the low temperature range. The temperature-independent carrier concentration indicates a heavily doped semiconductor character in the excess Cu samples.[169]
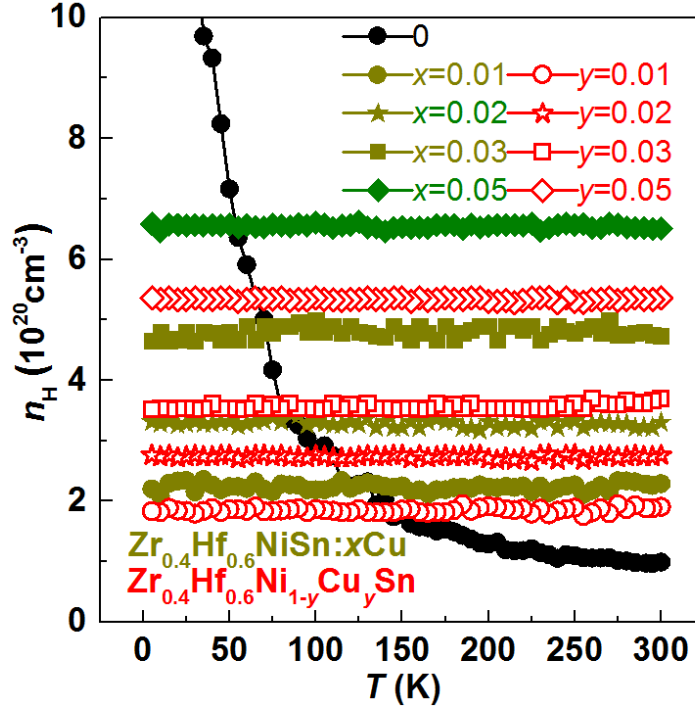
Figure 5-10. Low temperature Hall carrier density as a function of temperature.

For the $Zr_{0.4}Hf_{0.6}NiSn$ sample, the similar behavior is observed by Gałązka K, *et al.*[168] Following we will try to explain the phenomenon. At the low temperature range $T < 50$ K, for the $Zr_{0.4}Hf_{0.6}NiSn$ sample, the carrier concentration is very large. It decreases dramatically with the temperature increasing at the temperature range $T < 150$ K, and then decreases slowly with increasing temperature. In a mixed semiconductor, the Hall coefficient can be expressed as:

$$\frac{1}{en_H} = R_H = \frac{r_H(p\mu_h^2 - n\mu_e^2)}{e(p\mu_h + n\mu_e)^2} \tag{5-4}$$

where p is the hole concentration in the valence band, n_H the electron concentration in the conduction band, r_H Hall factor, and μ_h and μ_e electron mobility and hole mobility. If the band gap is large, the Fermi level is far from the edge of the valence band. In this condition, $n \gg p$ and R_H is negative, so $n_H \sim -n$. However, if the band gap is small, in the low temperature range the contribution from p will be comparable to n and then n_H has a non-monotonous behavior.
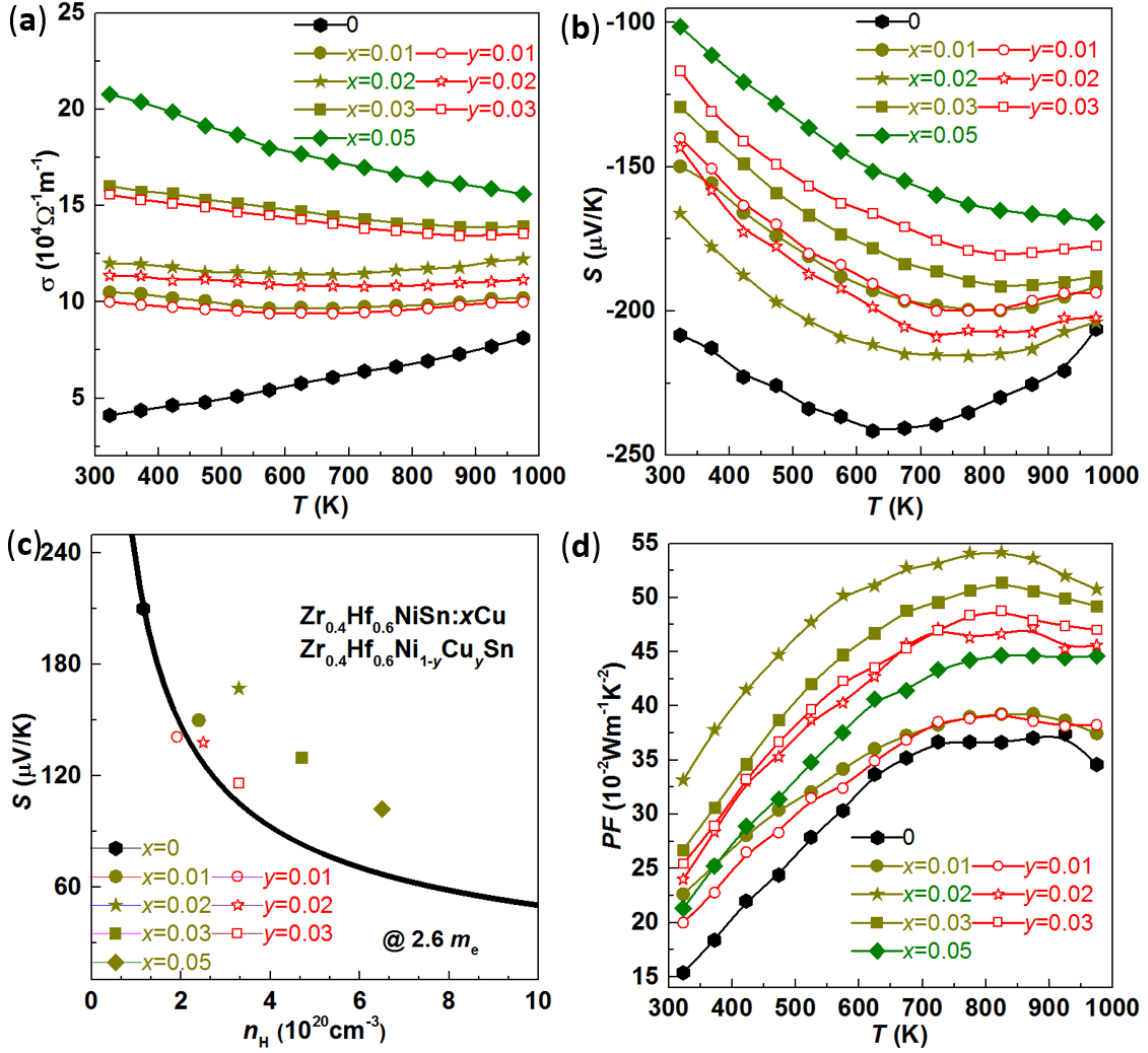
Figure 5-11. (a) Temperature dependence of electrical conductivity. (b) Temperature dependence of thermopower. (c) Pisarenko plot at room temperature and the black solid line represents the $Zr_{0.4}Hf_{0.6}NiSn$ with $m_d^* = 2.6m_e$. (d) Power factor as a function of temperature.

The thermoelectric properties of $Zr_{0.4}Hf_{0.6}NiSn:xCu$ and $Zr_{0.4}Hf_{0.6}Ni_{1-y}Cu_ySn$ compounds are presented in **Figure 5-11**, and analyzed by using the single parabolic band (SPB) model.[170] The slope of temperature-dependent electrical conductivity has a transition from positive to negative as shown in **Figure 5-11a**. The electrical conductivity σ of the $Zr_{0.4}Hf_{0.6}NiSn:xCu$ and $Zr_{0.4}Hf_{0.6}Ni_{1-y}Cu_ySn$ samples shows a transition from semi-conducting behavior to metal-like behavior. The calculated S of the $Zr_{0.4}Hf_{0.6}Ni_{1-y}Cu_ySn$ compounds by the SPB model agrees roughly with the experimental data at room temperature.

The m^* of $Zr_{0.4}Hf_{0.6}NiSn$ is estimated to be ~$2.6m_e$, as shown in the Pisarenko plot of **Figure 5-11c**. However the S of $Zr_{0.4}Hf_{0.6}NiSn:xCu$ is far away from the Pisarenko plot obviously. **Figure 5-11d** indicates that the power factors of $Zr_{0.4}Hf_{0.6}NiSn:xCu$ are higher than that of $Zr_{0.4}Hf_{0.6}Ni_{1-y}Cu_ySn$ samples. The carrier concentration of full-Heusler is much larger than that of the half-Heusler, so there is carrier injection effect in the $Zr_{0.4}Hf_{0.6}NiSn:xCu$ samples.

5.3.3 Reduced lattice thermal conductivity and mechanisms
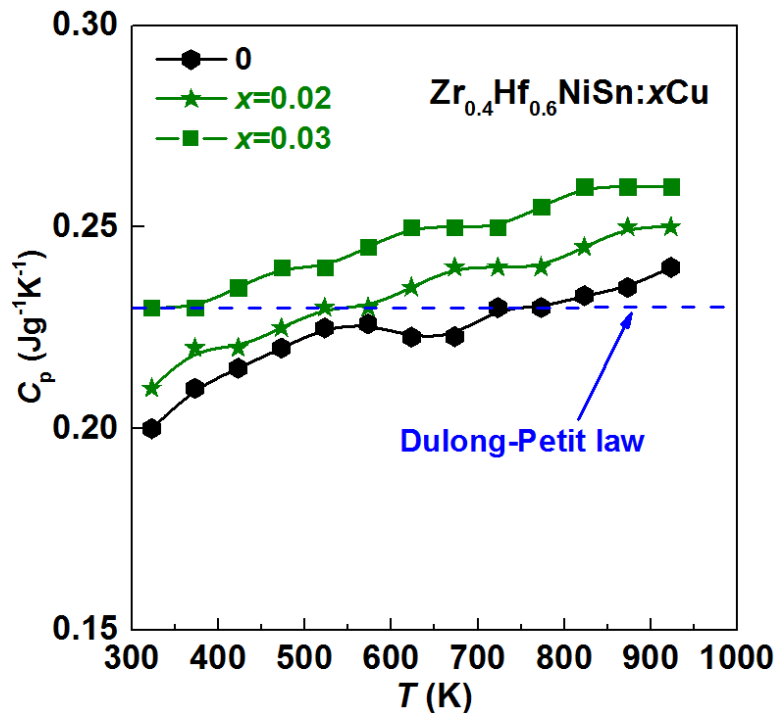
Figure 5-12. C_p as a function of temperature from DSC.

To get the thermal conductivity, we measure the thermal diffusivity from LFA and heat capacity obtained by DSC (shown in **Figure 5-12**). **Figure 5-13** shows the electron thermal conductivity as a function of temperature. κ_e is normally assessed by using the measured electrical conductivity σ through the Wiedemann-Franz relation: $\kappa_e = L\sigma T$, where L is the Lorenz number. In this work, the Lorenz number is calculated by fitting the S data of **Figure 5-11b** [143] and results are shown in **Figure 5-14**.
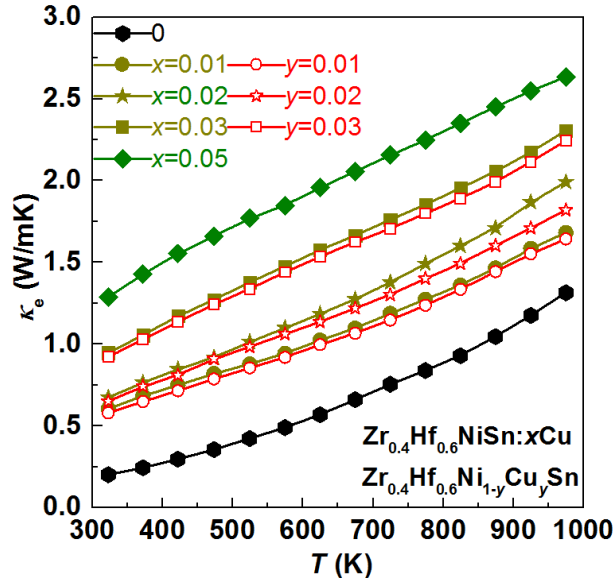
Figure 5-13. Electron thermal conductivity as a function of temperature.
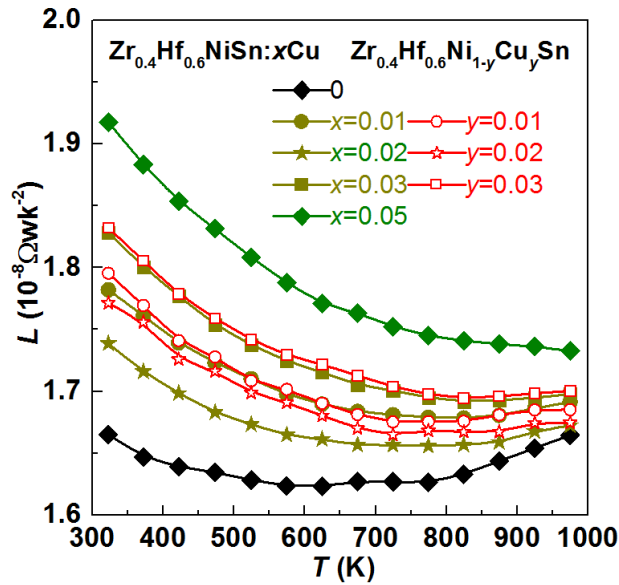
Figure 5-14. Temperature dependence of calculated Lorenz number L.

The temperature-dependent thermal conductivity and lattice thermal conductivity of $Zr_{0.4}Hf_{0.6}NiSn{:}x$Cu and $Zr_{0.4}Hf_{0.6}Ni_{1-y}Cu_ySn$ are presented in **Figures 5-15 a, b**. The κ_L is obtained by subtracting the electronic component κ_e from the total thermal conductivity κ.
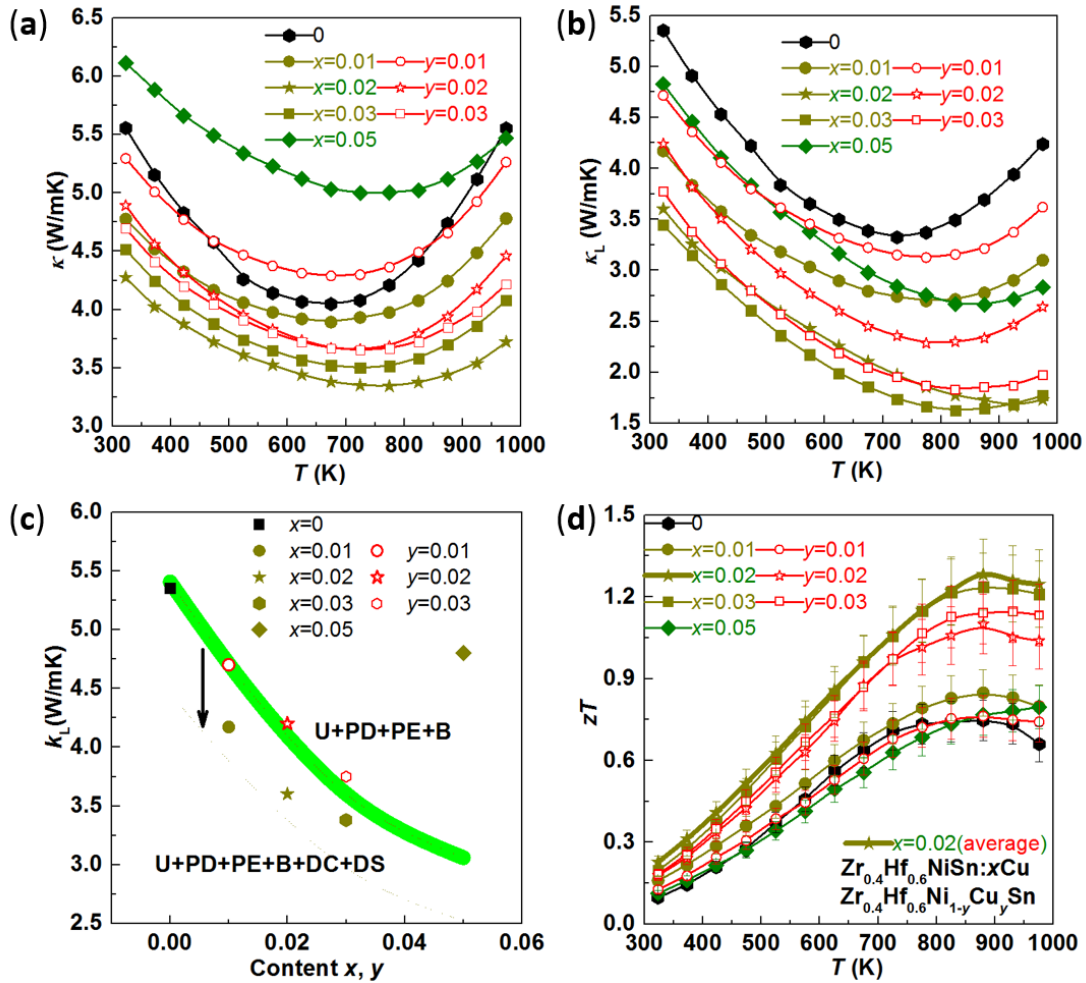
Figure 5-15. (a) Temperature dependence of total thermal conductivity. (b) Temperature dependence of lattice thermal conductivity. (c) Comparison of experimental and calculated lattice thermal conductivities at 325 K. (d) Temperature dependence of the figure of merit zT of $Zr_{0.4}Hf_{0.6}NiSn:xCu$ and $Zr_{0.4}Hf_{0.6}Ni_{1-y}Cu_ySn$.

Figure 5-15a shows that the κ of $Zr_{0.4}Hf_{0.6}NiSn:xCu$ and $Zr_{0.4}Hf_{0.6}Ni_{1-y}Cu_ySn$ compounds are lower than that of $Zr_{0.4}Hf_{0.6}NiSn$. The decrease in κ mainly results from the greatly suppressed κ_L. As shown in **Figure 5-15b**, especially, at 300 K and 875 K the κ_L of $Zr_{0.4}Hf_{0.6}NiSn:0.02Cu$ has 35% and 63% reduction respectively, compared with that of $Zr_{0.4}Hf_{0.6}NiSn$. With the same doping content, the κ_L of $Zr_{0.4}Hf_{0.6}NiSn:xCu$ is lower than that of $Zr_{0.4}Hf_{0.6}Ni_{1-y}Cu_ySn$ samples. As aforementioned, excess Cu creates full-Heusler

98

nanoparticles, which can scatter phonons, leading to the suppressed κ_L. For comparison, **Figure 5-15c** presents the experimental κ_L and calculated κ_L by the Callaway model,[22, 144] in which Phonon–phonon Umklapp process (U),[171] point-defect scattering (PD) of phonons,[147] electron-phonon scattering (EP),[146] grain boundary (B)[148] and dislocation scattering (DC+DS)[172] are considered. The equations used for the Callaway model are the same as those used in chapter 3. In order to calculate the contribution of boundary scattering, the average grain size of sample is needed. In this calculation we use an average grain size of $d = 30 \pm 10$ μm which is estimated from a typical scanning electron microscope image as shown in **Figure 5-16**. The fitting parameters used in calculation are summarized in **Table 5-2**.
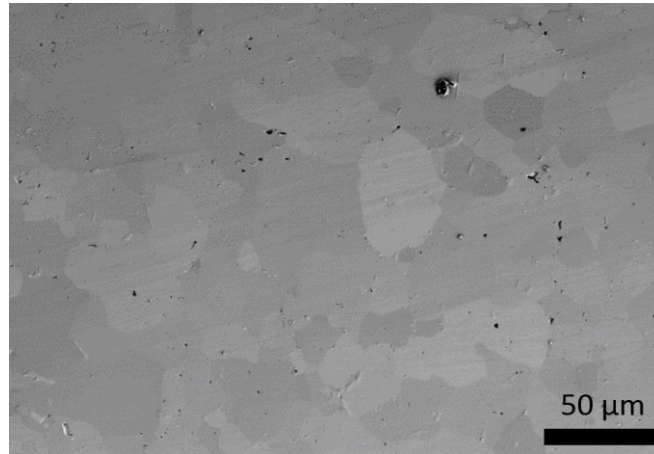
Figure 5-16. Typical scanning electron microscope image of the sample.

Table 5-2. Gruneisen parameters γ, Debye temperatures θ_D, and phonon velocities v used in calculation from Xie *et al.*'s work.

Parameter	Xie *et al.*'s work
γ	0.92
θ (K)	366
v (m/s)	3242

From **Figure 5-12c**, we can see that the $Zr_{0.4}Hf_{0.6}NiSn:xCu$ creates stronger boundary scattering and dislocation scattering than that of $Zr_{0.4}Hf_{0.6}Ni_{1-y}Cu_ySn$, leading to lower κ_L. At low content, the calculated κ_L has a good agreement with the experimental results (**Figure 5-12c**). However, at high excess Cu content (5%), the calculated κ_L significantly deviates from the experimental values, suggesting full-Heusler should also contribute to the κ_L at high Cu contents.

Temperature-dependent figure of merit zT of samples $Zr_{0.4}Hf_{0.6}NiSn:xCu$ and $Zr_{0.4}Hf_{0.6}Ni_{1-y}Cu_ySn$ are shown in **Figure 5-12d**. The zT values of the samples $Zr_{0.4}Hf_{0.6}NiSn:xCu$ except for $x = 0.05$ are higher than that of $Zr_{0.4}Hf_{0.6}NiSn$ while the zT values of samples $Zr_{0.4}Hf_{0.6}Ni_{1-y}Cu_ySn$ except for $y = 0.01$ are higher than that of $Zr_{0.4}Hf_{0.6}NiSn$ in the whole temperature range of measurement. The highest $zT \sim 1.3$ at 875 K is achieved for the sample $Zr_{0.4}Hf_{0.6}NiSn:0.02Cu$, which is around 100 % larger than that of the pristine sample studied here shown in **Figure 5-12d**. The best zT value of the sample $Zr_{0.4}Hf_{0.6}NiSn:0.02Cu$ shown in **Figure 5-12d** is average data of three times measurement values. In the experiment, we repeat the measurements of the thermoelectric properties of the sample $Zr_{0.4}Hf_{0.6}NiSn:0.02Cu$ for three times as discussed below.

5.3.4 Repeat measurements of the thermoelectric properties.

Three times measurement results of temperature-dependent electrical conductivity, thermopower, thermal conductivity and zT are shown in **Figure 5-17**. The three times measurement values are a little bit different due to the uncertainties of the experimental measurement. Considering the final zT, the difference is not so obvious. At 875 K the best zT is ~1.4 and the worse one is ~1.2, so the average value is ~1.3.
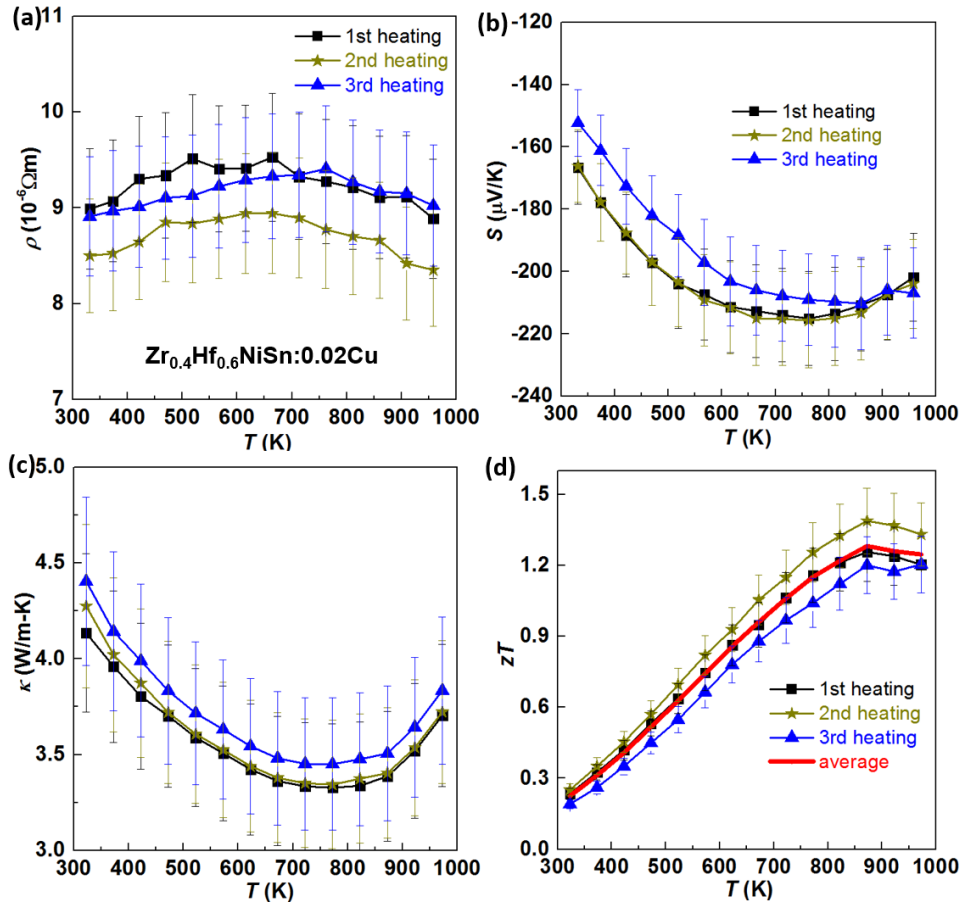
Figure 5-17. Three times heating values of (a) temperature dependence of electrical conductivity, (b) temperature dependence of thermopower, (c) temperature dependence of thermal conductivity and (d) *zT* as a function of temperature.

5.4 Summary

In the work, by rationally putting the excess Cu into the half-Heusler, forming the nanoparticles, the interrelated thermoelectric parameters can be decoupled and the simultaneous optimization of electrical power factor and significant reduction in thermal conductivity can be achieved.

Chapter 6 Thermoelectric Performance Investigation in n-type Half-Heusler $Zr_{0.4}Hf_{0.6}NiSn:x$Co

6.1 Abstract

The thermoelectric performances of $Zr_{0.4}Hf_{0.6}NiSn:x$Co (x = 0, 0.01, 0.02, 0.03 and 0.05) samples are investigated in the temperature range of 300 K < T < 975 K. In Co-excess experiment, we can also achieve similar half-Heusler (HH) / full-Heusler (FH) nanocomposites shown in chapter 5. However, in Co-excess experiment, it is found that Co-excess has negative contribution to the thermoelectric transport properties. Although the thermal conductivity is decreased by enhanced scattering between the nanoprecipitates and matrix, the electric transport performance of obtained nanocomposite is worse than that of pristine sample.

6.2 Introduction

As discussed in the last chapter, half-Heusler is a very good candidate for the thermoelectric application.[161, 173-176] According to the references, others [105-107, 164, 177, 178] use excess Ni in the Ni position to form the half-Heusler / full-Heusler (HH / FH) compounds to reduce the lattice thermal conductivity and enhance the *zT*. In the last chapter, we design the Cu-excess experiment to improve the thermoelectric performance. According to the results shown in the last chapter, excess Cu is an effective approach to increase the power factor and reduce thermal conductivity simultaneously. Based on the works in the references and last chapter, we decide to choose Co as excess metal in this experiment. In the periodic table Co, Cu and Ni are in the adjacent column and same rows. We wonder whether excess Co can offer similar functions as excess Cu and Ni did. This is the motivation for this work.

In the excess Co experiment, we achieve the half-Heusler / full-Heusler nanocomposites successfully as well, so the lattice thermal conductivity is depressed at the low temperature range. However, the electric experimental results of $Zr_{0.4}Hf_{0.6}NiSn{:}x$Co (x = 0, 0.01, 0.02, 0.03 and 0.05) are different from those of $Zr_{0.4}Hf_{0.6}NiSn{:}x$Cu (x = 0, 0.01, 0.02, 0.03 and 0.05). In the excess Co experiment, it is found that Co has negative contribution to the electric transport properties. The roles of excess Cu and excess Co in the electric transport are quite different. Here we demonstrate that the thermoelectric properties of n-type $Zr_{0.4}Hf_{0.6}NiSn$ half-Heusler compound cannot be improved through forming the full-Heusler nanocomposites by adding excess Co.

6.3 Results and discussion

6.3.1 Phase identification
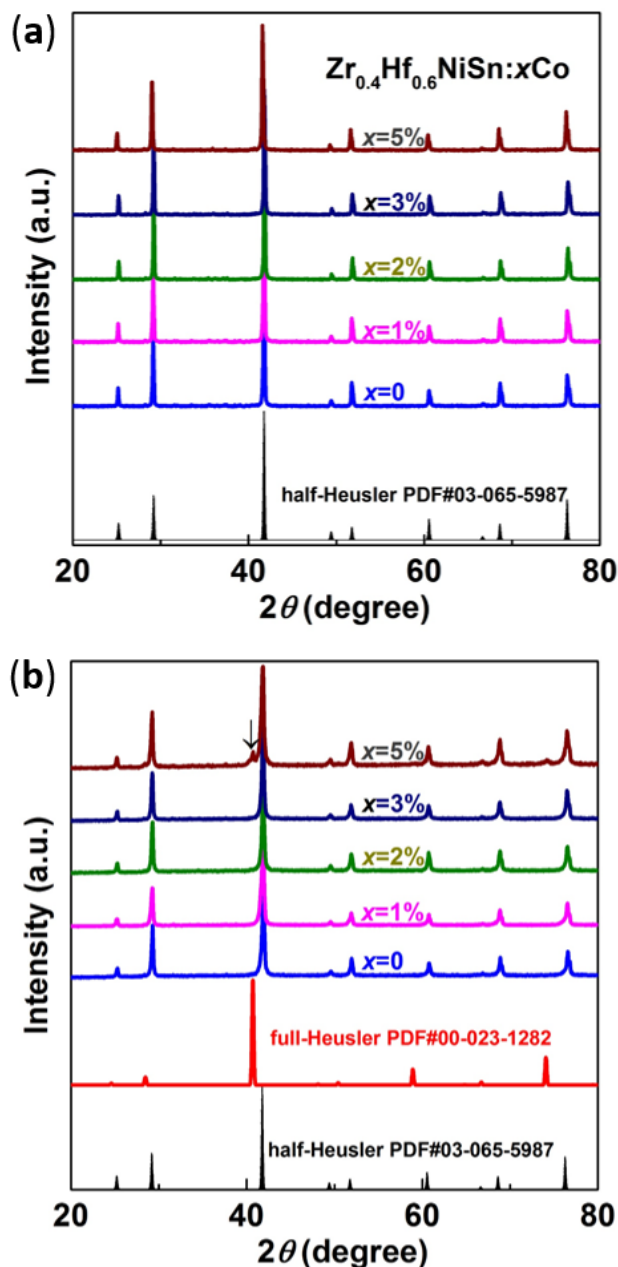
Figure 6-1. (a) XRD patterns of the samples $Zr_{0.4}Hf_{0.6}NiSn:xCo$ (x = 0, 0.01, 0.02, 0.03 and 0.05) compounds after arc melting at room temperature. (b) XRD patterns of the samples $Zr_{0.4}Hf_{0.6}NiSn:xCo$ (x = 0, 0.01, 0.02, 0.03 and 0.05) compounds after are melting and one week annealing.

In the Co-excess experiment, it is found that excess Co can form the full-Heusler as well. **Figure 6-1a** shows X-ray diffraction (XRD) patterns of $Zr_{0.4}Hf_{0.6}NiSn:xCo$ after arc melting without annealing. The XRD patterns after arc melting show a single phase, and can be indexed to the half-Heusler phase. **Figure 6-1b** shows XRD patterns of $Zr_{0.4}Hf_{0.6}NiSn:xCo$

105

after arc melting and one week annealing. In the XRD patterns after arc melting and one week annealing, we find the similar phenomenon shown in the XRD patterns of $Zr_{0.4}Hf_{0.6}NiSn:xCu$ after arc melting and one week annealing in chapter 5. It is found that there is an additional small reflection at $2\theta \sim 41.5°$, which corresponds to the reflection of full-Heusler phase, especially in pattern of $Zr_{0.4}Hf_{0.6}NiSn:0.05Co$ sample. The additional small reflection indicates that we achieve full-Heusler in the half-Heusler matrix in the Co-excess experiment as well.

6.3.2 Electrical properties

The temperature-dependent electrical conductivity of $Zr_{0.4}Hf_{0.6}NiSn:xCo$ ($x = 0$, 0.01, 0.02, 0.03 and 0.05) compounds are presented in **Figure 6-2a**. In the figure, the electrical conductivity of all the excess Co samples is much larger than that of the pristine sample. According to the position of Co in the periodic table, Co should give more holes while Cu can give more electrons.

The temperature-dependent carrier concentration of $Zr_{0.4}Hf_{0.6}NiSn:xCo$ ($x = 0$, 0.01, 0.02, 0.03 and 0.05) compounds is shown in **Figure 6-2b**. As the $Zr_{0.4}Hf_{0.6}NiSn$ sample in the experiment is n-type semiconductor, the resistivity of the excess Co samples will be larger than that of the pristine sample while the resistivity of excess Cu samples will be smaller than that of the pristine sample in chapter 5. At room temperature, carrier mobilities of $Zr_{0.4}Hf_{0.6}NiSn:xCo$ ($x = 0.01$, 0.02, 0.03 and 0.05) compounds are $0.18 cm^2V^{-1}s^{-1}$, $0.16 cm^2V^{-1}s^{-1}$, $0.68 cm^2V^{-1}s^{-1}$ and $0.47 cm^2V^{-1}s^{-1}$ respectively, which is much lower than that of $Zr_{0.4}Hf_{0.6}NiSn$.

The temperature-dependent Seebeck coefficient of $Zr_{0.4}Hf_{0.6}NiSn:xCo$ ($x = 0$, 0.01, 0.02, 0.03 and 0.05) compounds are presented in **Figure 6-2c**. From the figure, the Seebeck coefficient of all the excess Co samples is smaller than that of the pristine sample. If we compare the data of Seebeck coefficient with the resistivity, we can confirm that Co has the negative contribution to the carrier concentration in the experiment. Especially in the

$Zr_{0.4}Hf_{0.6}NiSn:0.05Co$ sample, the Seebeck coefficient is positive, which means the carrier charge is hole. Due to the negative contribution to the carrier concentration from excess Co, the Seebeck coefficient in $Zr_{0.4}Hf_{0.6}NiSn:xCo$ (x = 0.01, 0.02, 0.03 and 0.05) compounds is damaged greatly.
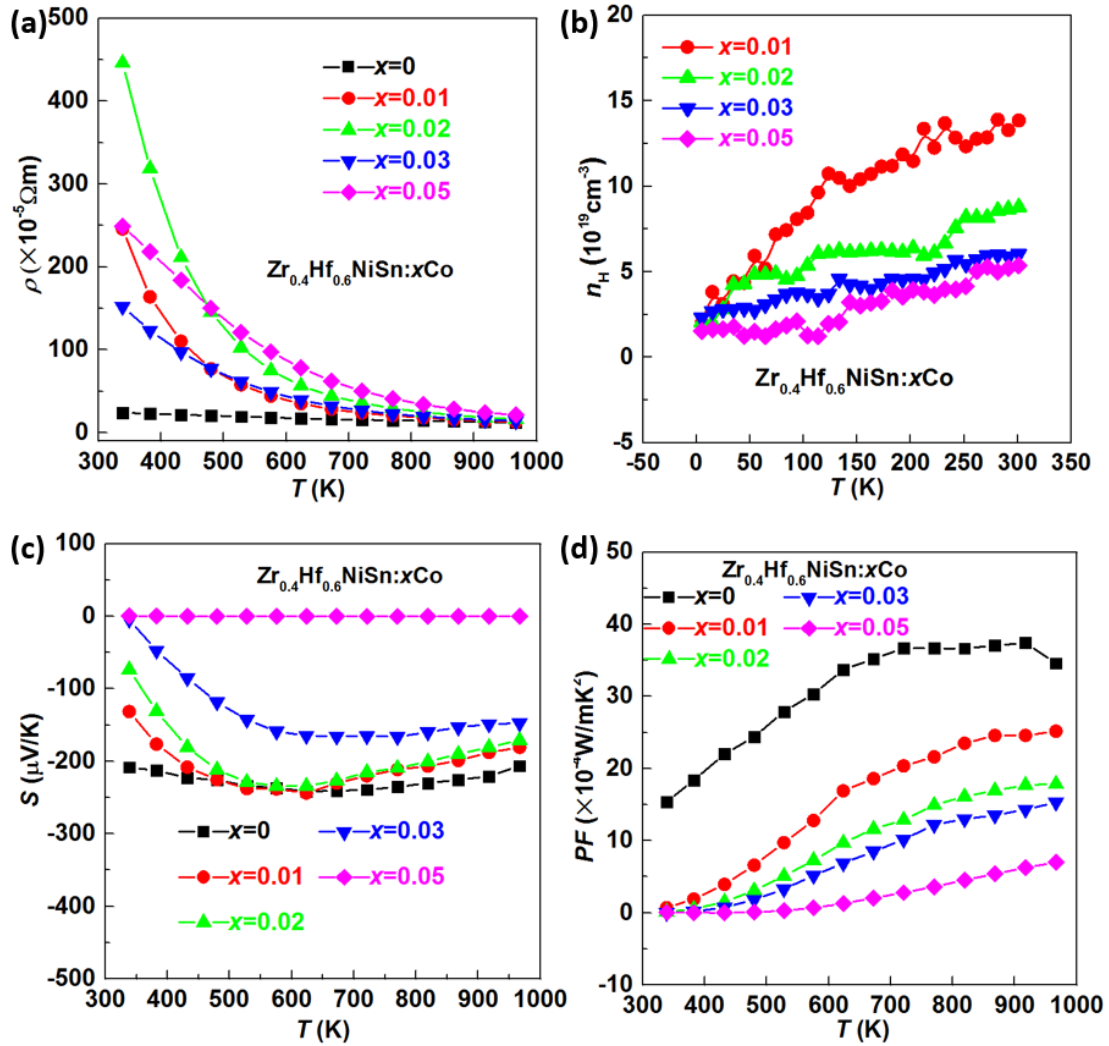
Figure 6-5. Temperature dependence of (a) electric resistivity, (b) carrier concentration, (c) Seebeck coefficient and (d) power factor as a function of temperature of $Zr_{0.4}Hf_{0.6}NiSn:xCo$ (x = 0, 0.01, 0.02, 0.03 and 0.05) compounds.

The power factor as a function of temperature of $Zr_{0.4}Hf_{0.6}NiSn:xCo$ (x = 0, 0.01, 0.02, 0.03 and 0.05) compounds are presented in **Figure 6-2d**. The power factor gives us the overall

information of the electric transport properties. **Figure 6-2d** indicates that the power factors of $Zr_{0.4}Hf_{0.6}NiSn:xCo$ are smaller than that of the pristine samples. Because of the bad performance in both electrical conductivity and Seebeck coefficient, the power factor of Co-excess samples decreases significantly.

6.3.3 Reduced lattice thermal conductivity and mechanisms

The temperature-dependent thermal conductivity of $Zr_{0.4}Hf_{0.6}NiSn:xCo$ ($x = 0$, 0.01, 0.02, 0.03 and 0.05) compounds is shown in **Figure 6-3a**. It can be seen that κ of the pristine sample decreases with increasing temperature from 300 K to 700-750 K, and then it gradually increases as the temperature is further increased.

For the $Zr_{0.4}Hf_{0.6}NiSn:xCo$ ($x = 0.01$, 0.02, 0.03 and 0.05) compounds, it can be seen that κ decreases with increasing temperature from 300 K to 500 K, and then it gradually increases as the temperature is further increased. So in the excess Co samples, bipolar effect comes out earlier because of the negative contribution of Co to the carrier concentrations. The total thermal conductivity of excess Co samples $Zr_{0.4}Hf_{0.6}NiSn:xCo$ ($x = 0.01$, 0.02, 0.03 and 0.05) is lower than that of the pristine sample $Zr_{0.4}Hf_{0.6}NiSn$, especially in the low temperature range. At the high temperature range $T > 800$ K, the thermal conductivities of all the samples $Zr_{0.4}Hf_{0.6}NiSn:xCo$ ($x = 0$, 0.01, 0.02, 0.03 and 0.05) are close to each other.

The total thermal conductivity includes the lattice thermal conductivity κ_L and the carrier contribution κ_e: $\kappa = \kappa_L + \kappa_e$. Thus, κ_L can be obtained by subtracting κ_e that can be evaluated using the Wiedemann-Franz law: $\kappa_e = LT/\rho$, where L is the Lorenz number. It is known that L is dependent on reduced chemical potential ξ_F, the band structure and details of the scattering process. Here we choose $L_0 = 2.45 \times 10^{-8}$ ΩWK^{-2}.

The electron thermal conductivity as a function of temperature of $Zr_{0.4}Hf_{0.6}NiSn:xCo$ ($x = 0$, 0.01, 0.02, 0.03 and 0.05) compounds is shown in **Figure 6-3b**. The electron thermal

108

conductivity of excess Co sample is lower than that of the pristine sample in the testing temperature range.

Figure 6-3. Temperature dependence of (a) total thermal conductivity, (b) electron thermal conductivity, (c) lattice thermal conductivity and (d) figure of merit zT of Zr$_{0.4}$Hf$_{0.6}$NiSn:xCo (x = 0, 0.01, 0.02, 0.03 and 0.05) compounds.
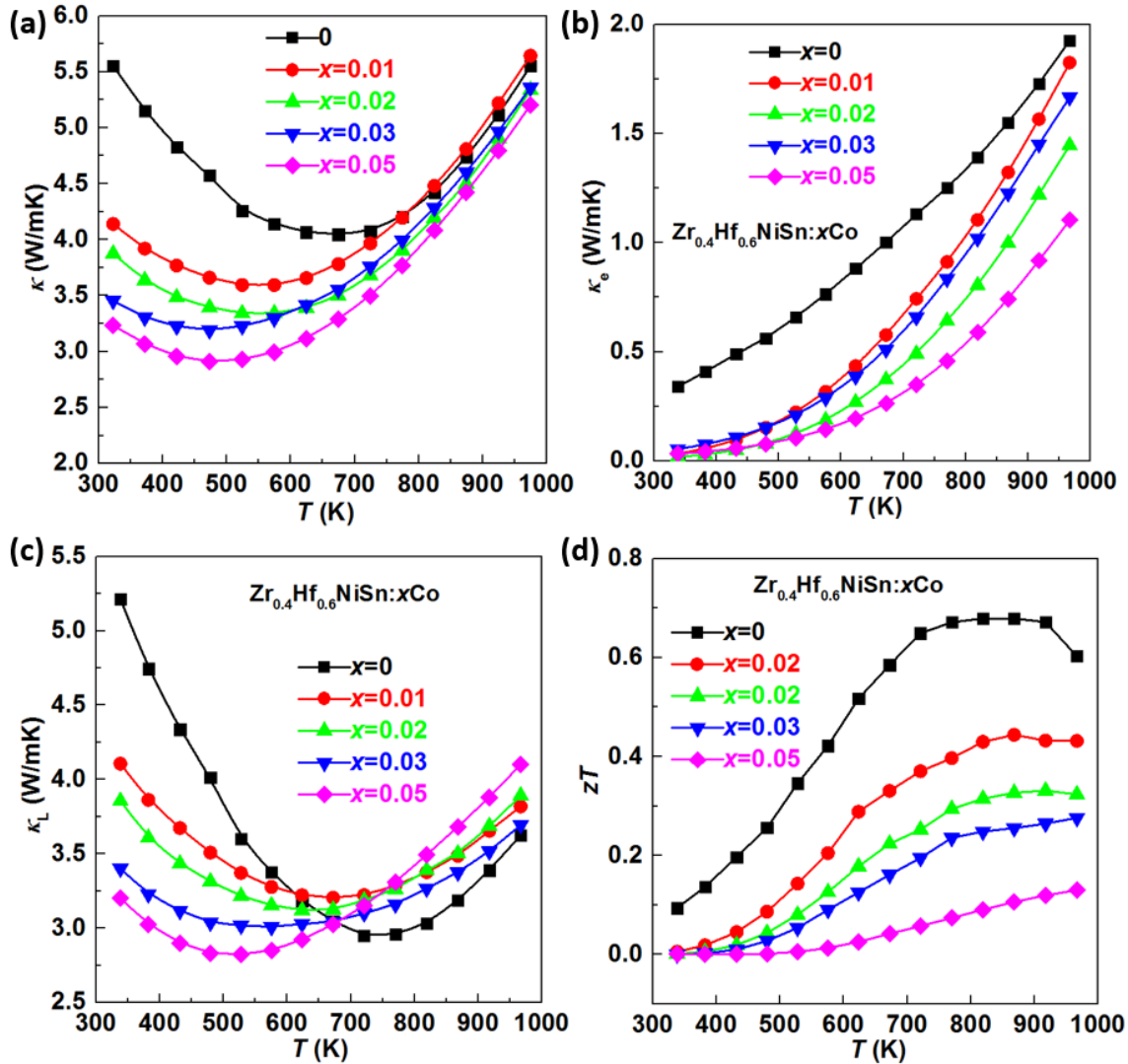
The temperature-dependent lattice thermal conductivity of Zr$_{0.4}$Hf$_{0.6}$NiSn:xCo (x = 0, 0.01, 0.02, 0.03 and 0.05) compounds is shown in **Figure 6-3c**. It can be seen that lattice thermal conductivity of the pristine sample decreases with increasing temperature from 300 K to 700 - 750 K, and then it gradually increases as the temperature is further increased. For the excess

Co $Zr_{0.4}Hf_{0.6}NiSn:xCo$ compounds, it can be seen that κ decreases with increasing temperature from 300 K to 550 K, and then it gradually increases as the temperature is further increased.

The lattice thermal conductivity of Co-excess sample is lower than that of the pristine sample in the low temperature range $T < 600$ K. Especially, at 300 K the k_L of $Zr_{0.4}Hf_{0.6}NiSn:0.03Co$ and $Zr_{0.4}Hf_{0.6}NiSn:0.05Co$ has 35% and 38% reduction respectively, compared with that of $Zr_{0.4}Hf_{0.6}NiSn$. In the excess Co experiment, we achieve the half-Heusler / full-Heusler nanocomposites successfully as well. The scattering between the nanoparticles and the matrix is increased, and finally the lattice thermal conductivity is depressed at the low temperature range. At the high temperature range $T > 600$ K, lattice thermal conductivity of excess Co sample is larger than that of the pristine sample.

Figure 6-3d shows the temperature-dependent figure of merit zT of $Zr_{0.4}Hf_{0.6}NiSn:xCo$ ($x = 0$, 0.01, 0.02, 0.03 and 0.05) compounds. In this figure, figure of merit zT of $Zr_{0.4}Hf_{0.6}NiSn:xCo$ ($x = 0$, 0.01, 0.02, 0.03 and 0.05) compounds increases with the temperature increasing. Due to obviously decreased PF in the excess Co samples $Zr_{0.4}Hf_{0.6}NiSn:xCo$ ($x = 0.01$, 0.02, 0.03 and 0.05), zT of the excess Co sample is smaller than that of the pristine sample in the whole measurement range.

6.4 Conclusions

In summary, the thermoelectric properties of $Zr_{0.4}Hf_{0.6}NiSn:xCo$ ($x = 0$, 0.01, 0.02, 0.03 and 0.05) compounds have been studied at temperature from 300 K to 975 K. The figure of merit zT for all the excess Co samples is worse than that of pristine sample due to significant reduction of power factor.

Chapter 7 Summary and Outlook

7.1 Summary

In this thesis, two potential thermoelectric candidates with diamond-like structure, chalcogenide and half-Heusler, are chosen as investigated subjects, and their thermoelectric performances have been improved via substitution induced band structure engineering and incorporation of Heusler nanoprecipitations into half-Heusler matrix respectively. The main conclusions of this thesis are listed below:

The thermoelectric performances of $Cu_{3-x}Sm_xSbSe_4$ ($x \leq 0.025$) samples are investigated. In Cu_3SbSe_4, from density functional theory calculations with spin-orbit coupling, it is determined that in the valence band, there are a rather flat band and a relatively lighter band. In our experiment, through Sm doping, the lighter band is activated to contribute to the transport, consequently, the carrier concentration and mobility can be increased simultaneously. Because of the increased carrier mobility, the electrical conductivity is enhanced greatly. At the same time, the thermal conductivity is decreased due to the strengthened point-defect scattering of heat carrying phonons. This work reveals that slight Sm doping in Cu_3SbSe_4 can improve the zT values and thermoelectric properties.

Based on the previous only Sm-doped Cu_3SbSe_4 work, we decide to choose S to form Cu_3SbSe_4-Cu_3SbS_4 solid solution to further decrease lattice thermal conductivity. S and Se are in the same column and adjacent rows in the periodic table. Through Callaway model, we demonstrate that the Sm and S co-substitution induces a stronger mass fluctuations and strain field fluctuations. Finally through S and Sm co-substitution in the Cu_3SbSe_4, we achieve a large decrease in the lattice thermal conductivity due to the improved point defects, resulting an evident improvement in the thermoelectric performance.

The thermoelectric performances of Cu-excess $Zr_{0.4}Hf_{0.6}NiSn{:}xCu$ ($x \leq 0.05$) and Cu-doped $Zr_{0.4}Hf_{0.6}Ni_{1-y}Cu_ySn$ ($y \leq 0.05$) and Co-excess$_{.4}Hf_{0.6}NiSn{:}zCo$ ($z \leq 0.05$) samples are

111

investigated. In the excess Cu experiment, we achieve the half-Heusler / full-Heusler nanocomposites successfully, which is an effective strategy for optimizing power factor and reducing thermal conductivity simultaneously. In the nanostructured half-Heusler / full-Heusler thermoelectric materials $Zr_{0.4}Hf_{0.6}NiSn:x$Cu, because the carrier concentration in the full-Heusler is much higher than that of the half-Heusler, some electrons in the full-Heusler nanoparticles will inject into the matrix half-Heusler. At the same time, phonons scattering at the interfaces between full-Heusler nanoparticles and half-Heusler matrix is enlarged significantly, resulting in reducing lattice thermal conductivity. A good zT value is obtained in $Zr_{0.4}Hf_{0.6}NiSn:2\%$Cu, which is much higher than that of the pristine sample, and the value is comparable to that of other well-known state-of-the-art n-type high-temperature thermoelectric materials.

However, in the excess Co experiment it is found that Co has negative contribution to the thermoelectric transport properties. Considering the position of Co in the periodic table, Co will give more holes while Cu can give more electrons. As $Zr_{0.4}Hf_{0.6}NiSn$ is a n-type semiconductor, the resistivity of the excess Co samples will be larger than that of the pristine sample while the Seebeck coefficient of excess Co samples will be smaller than that of the pristine sample. So the electric properties are damaged obviously. The roles of Cu and Co in the electric transport are quite different. Here we demonstrate that the thermoelectric properties of n-type $Zr_{0.4}Hf_{0.6}NiSn$ half-Heusler compound cannot be improved through forming the full-Heusler nanocomposites by excess Co.

7.2 Outlook of the future work

For the chalcogenide, Cu_3SbS_4 has similar crystal structure as Cu_3SbSe_4. Compared with selenium, sulfur has many advantages. Sulfur is 1,000 times more abundant than selenium in the earth's crust, and in the point view of commercial application S possesses lower cost and less toxicity as compared to Se. Cu_3SbS_4 has rarely been investigated as thermoelectric materials due to the bad electric performance. However, the thermal conductivity of Cu_3SbS_4 is much lower than that of Cu_3SbSe_4. In the $Cu_{3-x}Sm_xSbSe_4$ ($x \leq 0.025$) experiment, the

112

resistivity is decreased obviously via engaging the light valence band, so we could design the similar experiment. Though appropriate substitution, it is possible to improve the electric performance of Cu_3SbS_4 as well as zT.

For half-Heusler, $Zr_{0.4}Hf_{0.6}NiSn$ contains Hf. Hf is quite expensive, so it is not so good for the commercial applications. Considering the price, ZrNiSn has no Hf and it is much cheaper than that of $Zr_{0.4}Hf_{0.6}NiSn$. Compared with $Zr_{0.4}Hf_{0.6}NiSn$, ZrNiSn has larger thermal conductivity due to the weaker alloying scattering of phonons. In the Cu-excess $Zr_{0.4}Hf_{0.6}NiSn{:}x$Cu ($x \leq 0.05$) experiment, the thermal conductivity is decreased obviously. Therefore, it is necessary to investigate the thermoelectric performance of ZrNiSn$:x$Cu. Through forming the half-Heusler / full-Heusler nanocomposites by excess Cu, it is highly possible to improve the thermal performance of ZrNiSn.

Appendix A Thermoelectric Performance Investigation in n-type Full-Heusler $Zr_{0.4}Hf_{0.6}Ni_{2-x}Cu_xSn$ and $TiFe_2Sn$

A.1 Abstract

The thermoelectric performances of full-Heusler $Zr_{0.4}Hf_{0.6}Ni_2Sn$ and $Zr_{0.4}Hf_{0.6}Ni_{1.98}Cu_{0.02}Sn$ samples are investigated in the temperature range of 300 K $< T <$ 775 K. It is found that the trend of experimental results of electric resistivity of $Zr_{0.4}Hf_{0.6}Ni_2Sn$ and $Zr_{0.4}Hf_{0.6}Ni_{1.98}Cu_{0.02}Sn$ is the same with that of $Zr_{0.4}Hf_{0.6}NiSn{:}xCu$ (x = 0, 0.01, 0.02, 0.03 and 0.05). Considering the experimental results from both $Zr_{0.4}Hf_{0.6}Ni_2Sn$ and $TiFe_2Sn$, full-Heusler is not a good candidate for thermoelectric applications.

This work discussed in this chapter is in preparation for publication.

A.2 Introduction

According to the discussion in the chapter 5, we design the Cu-excess experiment to improve the thermoelectric performance. In the excess Cu experiment, half-Heusler $Zr_{0.4}Hf_{0.6}NiSn{:}xCu$, the resistivity is enhanced due to the increase of carrier concentration. According to the results in the chapter 5, excess Cu can form full-Heusler phase $Zr_{0.4}Hf_{0.6}Ni_{2-x}Cu_xSn$, and then we want to know the function of Cu in the substituted full-Heusler sample. So we decide to choose full-Heusler $Zr_{0.4}Hf_{0.6}Ni_2Sn$ as the research goal in this experiment.

In the experiment, the trend of electric resistivity results of $Zr_{0.4}Hf_{0.6}Ni_2Sn$ and $Zr_{0.4}Hf_{0.6}Ni_{1.98}Cu_{0.02}Sn$ is the same with that of $Zr_{0.4}Hf_{0.6}NiSn{:}xCu$ ($x = 0$, 0.01, 0.02, 0.03 and 0.05) in the chapter 5. Here we demonstrate that Cu has positive contribution to the electric conductivity in n-type $Zr_{0.4}Hf_{0.6}Ni_2Sn$ full-Heusler compound.

A.3 Results and discussion

A.3.1 Phase identification and analysis

Figure A-1 shows the XRD patterns of the $Zr_{0.4}Hf_{0.6}Ni_2Sn$ and $Zr_{0.4}Hf_{0.6}Ni_{1.98}Cu_{0.02}Sn$ samples after arc melting and one week annealing. In the **Figure A-1**, the main reflections can be indexed to the $ZrNi_2Sn$ structure (standard JCPDS number: 00-023-1282; space group $Fm\bar{3}m$) and there is no obvious structural change observed here. However, from the figure a tiny amount of $Zr_{0.4}Hf_{0.6}Ni_4Sn$ can be found in all the samples. As the content of impurities are found to be roughly the same for all samples, it is plausible to treat the impurities as part of the Heusler matrix.
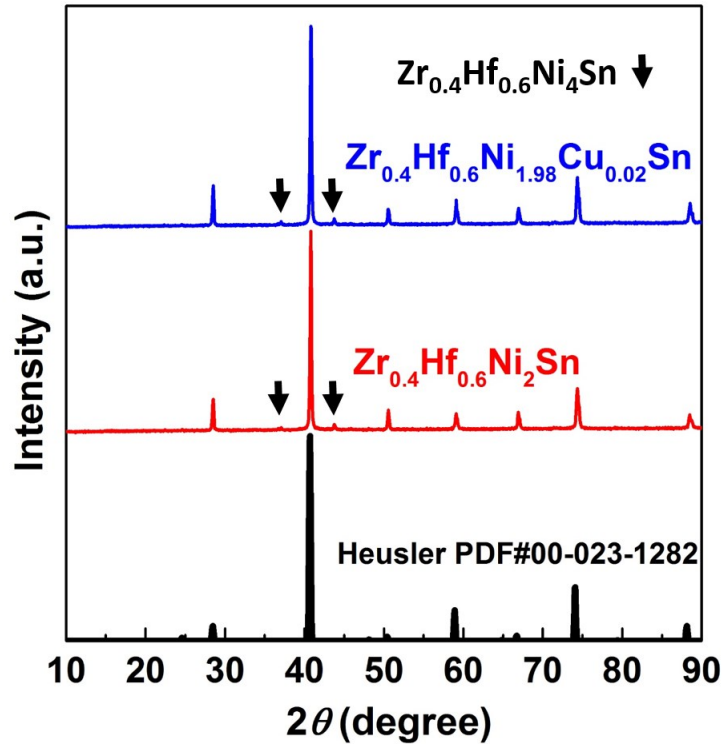
Figure A-1. XRD patterns of the samples of $Zr_{0.4}Hf_{0.6}Ni_2Sn$ and $Zr_{0.4}Hf_{0.6}Ni_{1.98}Cu_{0.02}Sn$ after arc melting and one week annealing.

A.3.2 Electrical and thermal properties

Figure A-2 shows the temperature-dependent electrical conductivity of $Zr_{0.4}Hf_{0.6}Ni_2Sn$ and $Zr_{0.4}Hf_{0.6}Ni_{1.98}Cu_{0.02}Sn$. It is found that the trend of electric experimental result of $Zr_{0.4}Hf_{0.6}Ni_2Sn$ and $Zr_{0.4}Hf_{0.6}Ni_{1.98}Cu_{0.02}Sn$ is the same with that of $Zr_{0.4}Hf_{0.6}NiSn:xCu$. In this figure, the resistivity of $Zr_{0.4}Hf_{0.6}Ni_{1.98}Cu_{0.02}Sn$ is smaller than that of $Zr_{0.4}Hf_{0.6}Ni_2Sn$. It is because that the carrier concentration in the Cu substitution sample $Zr_{0.4}Hf_{0.6}Ni_{1.98}Cu_{0.02}Sn$ is larger than that of $Zr_{0.4}Hf_{0.6}Ni_2Sn$. We try to measure the carrier concentration in the sample through PPMS, however the carrier concentration is too large to get the signal.
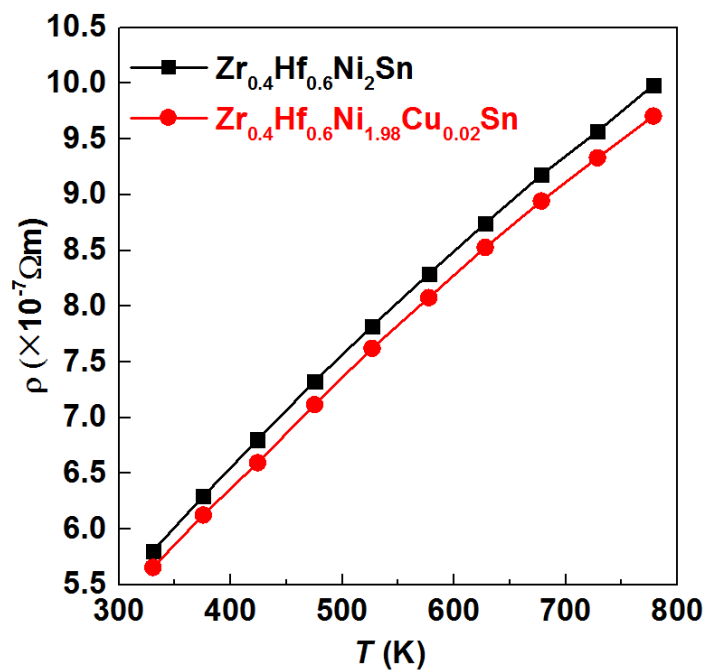
Figure A-2. Temperature dependence of electrical resistivity of $Zr_{0.4}Hf_{0.6}Ni_2Sn$ and $Zr_{0.4}Hf_{0.6}Ni_{1.98}Cu_{0.02}Sn$.
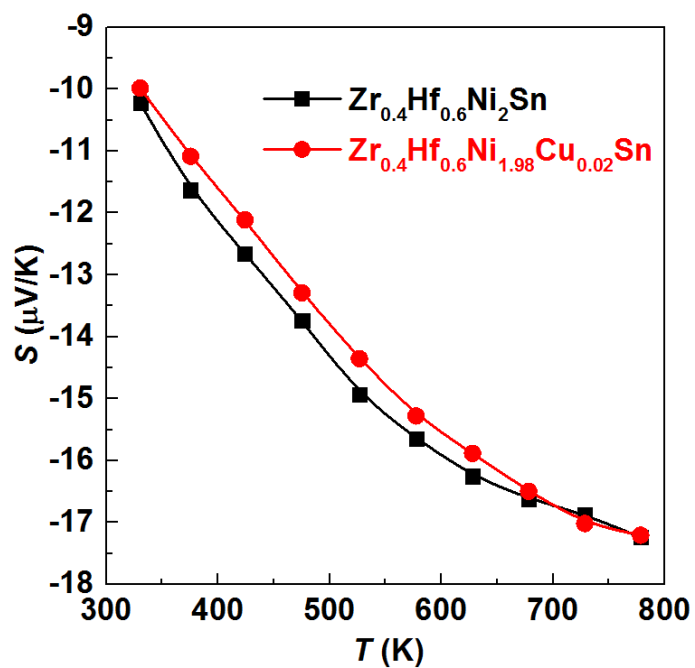
Figure A-3. Temperature dependence of Seebeck coefficient of $Zr_{0.4}Hf_{0.6}Ni_2Sn$ and $Zr_{0.4}Hf_{0.6}Ni_{1.98}Cu_{0.02}Sn$.

Figure A-3 shows the temperature-dependent Seebeck coefficient of $Zr_{0.4}Hf_{0.6}Ni_2Sn$ and $Zr_{0.4}Hf_{0.6}Ni_{1.98}Cu_{0.02}Sn$. In this figure, the Seebeck coefficient of $Zr_{0.4}Hf_{0.6}Ni_{1.98}Cu_{0.02}Sn$ is smaller than that of $Zr_{0.4}Hf_{0.6}Ni_2Sn$. The phenomenon is normal. According to the Pisarenko relation, if the carrier concentration is bigger, the Seebeck coefficient will be smaller.

Figure A-4. Power factor as a function of temperature of $Zr_{0.4}Hf_{0.6}Ni_2Sn$ and $Zr_{0.4}Hf_{0.6}Ni_{1.98}Cu_{0.02}Sn$.

Figure A-4 shows the temperature-dependent power factor of $Zr_{0.4}Hf_{0.6}Ni_2Sn$ and $Zr_{0.4}Hf_{0.6}Ni_{1.98}Cu_{0.02}Sn$. In this figure, the power factor of $Zr_{0.4}Hf_{0.6}Ni_{1.98}Cu_{0.02}Sn$ is smaller than that of $Zr_{0.4}Hf_{0.6}Ni_2Sn$ in the temperature range $300\ K < T < 650\ K$ while it is larger than that of $Zr_{0.4}Hf_{0.6}Ni_2Sn$ in the temperature range $650\ K < T < 775\ K$.

Figure A-5. Temperature dependence of thermal diffusivity of $Zr_{0.4}Hf_{0.6}Ni_2Sn$ and $Zr_{0.4}Hf_{0.6}Ni_{1.98}Cu_{0.02}Sn$ specimens.

Figure A-5 shows the temperature-dependent thermal diffusivity of $Zr_{0.4}Hf_{0.6}Ni_2Sn$ and $Zr_{0.4}Hf_{0.6}Ni_{1.98}Cu_{0.02}Sn$ from LFA. In this figure, the thermal diffusivity of $Zr_{0.4}Hf_{0.6}Ni_{1.98}Cu_{0.02}Sn$ is larger than that of $Zr_{0.4}Hf_{0.6}Ni_2Sn$.

According to Dulong-Petit law, the specific heat of $Zr_{0.4}Hf_{0.6}Ni_2Sn$ and $Zr_{0.4}Hf_{0.6}Ni_{1.98}Cu_{0.02}Sn$ is around 0.26 J / (g K). By the Archimedes method, the density of the sample is around 10.2 g / cm^3. According to the values of thermal diffusivity, specific heat and density, we obtain the thermal conductivity shown in **Figure A-6**. In this figure, the thermal conductivity of $Zr_{0.4}Hf_{0.6}Ni_{1.98}Cu_{0.02}Sn$ is larger than that of $Zr_{0.4}Hf_{0.6}Ni_2Sn$ due to the electron thermal conductivity contribution in $Zr_{0.4}Hf_{0.6}Ni_{1.98}Cu_{0.02}Sn$ is larger than that in $Zr_{0.4}Hf_{0.6}Ni_2Sn$.
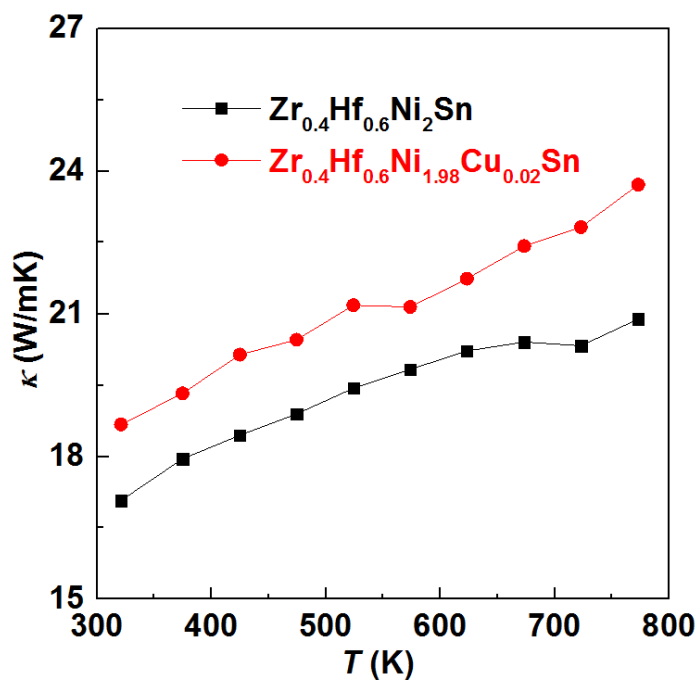
Figure A-6. Temperature dependence of the thermal conductivity κ of $Zr_{0.4}Hf_{0.6}Ni_2Sn$ and $Zr_{0.4}Hf_{0.6}Ni_{1.98}Cu_{0.02}Sn$ specimens.
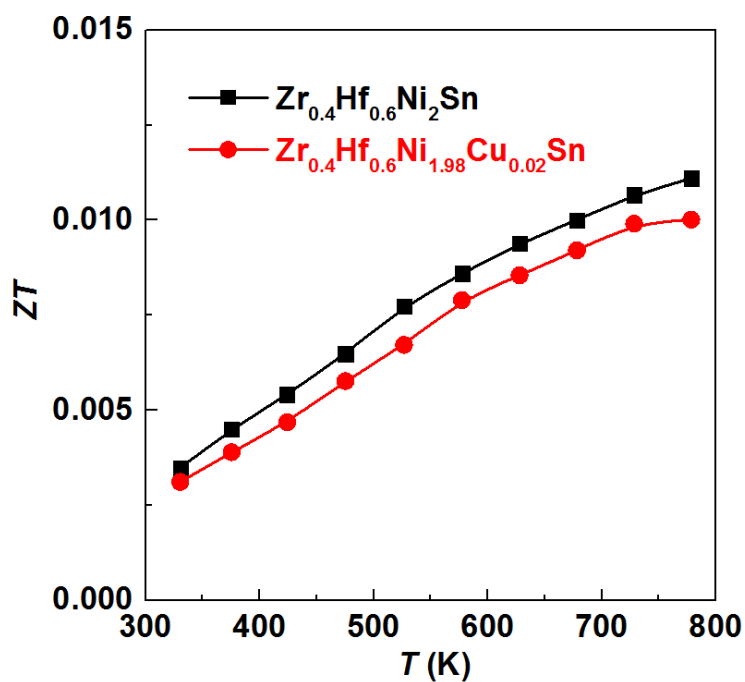
Figure A-7. Temperature dependence of the zT of $Zr_{0.4}Hf_{0.6}Ni_2Sn$ and $Zr_{0.4}Hf_{0.6}Ni_{1.98}Cu_{0.02}Sn$ specimens.

Figure A-7 shows the temperature-dependent figure of merit zT of $Zr_{0.4}Hf_{0.6}Ni_2Sn$ and $Zr_{0.4}Hf_{0.6}Ni_{1.98}Cu_{0.02}Sn$ compounds. From the figure, zT of the Cu doped $Zr_{0.4}Hf_{0.6}Ni_{1.98}Cu_{0.02}Sn$ sample is smaller than that of the undoped sample $Zr_{0.4}Hf_{0.6}Ni_2Sn$ in the whole measurement range.

A.3.3 Is full-Heusler a good candidate for thermoelectric application?
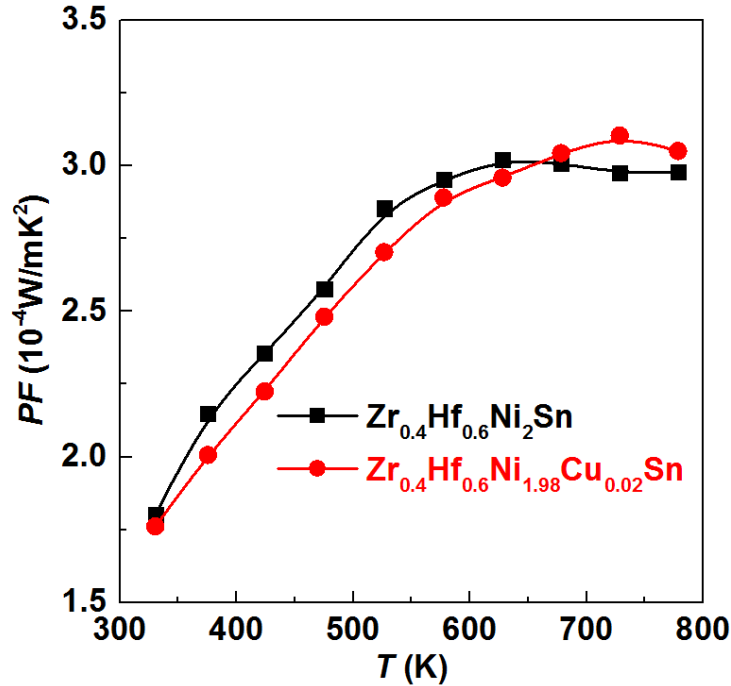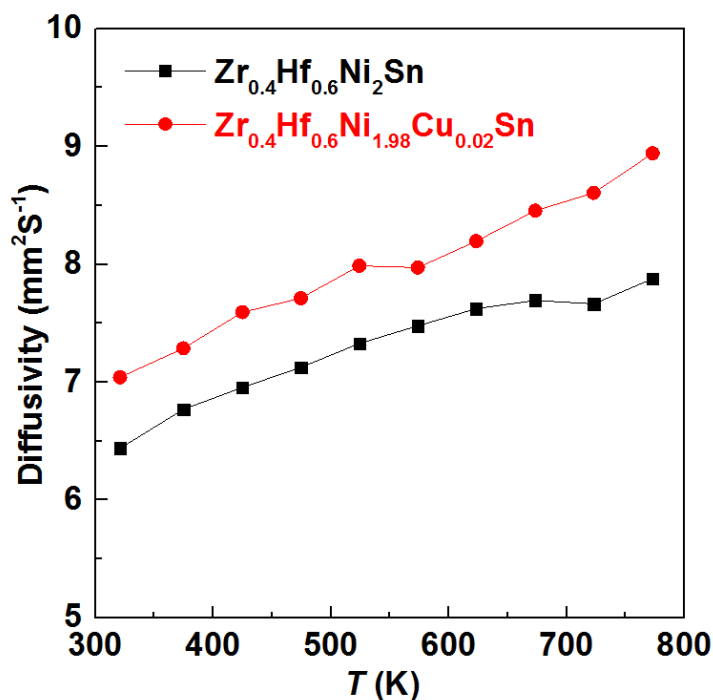
From the zT of $Zr_{0.4}Hf_{0.6}Ni_2Sn$ and $Zr_{0.4}Hf_{0.6}Ni_{1.98}Cu_{0.02}Sn$ compounds, we notice full-Heusler $Zr_{0.4}Hf_{0.6}Ni_2Sn$ is not good candidate for thermoelectric applications.

Unlike half-Heusler compounds, only few Heusler compounds have been studied in respect of thermoelectric application due to the fact that their metallic band structure is usually associated with poor thermoelectric performance.[179-182] Nevertheless, Heusler compounds have attracted a lot of attention due to their unusual magnetic and transport properties.[183][184] Recently, Yabuuchi *et al.*[185] and Bilc *et al.*[186] have concluded from first principle calculations that bulk $TiFe_2Sn$, a Heusler compound with uncritical elements, may possess a large thermoelectric power factor at certain charge carrier concentrations. Ślebarski *et al.*[187] and Lue *et al.*[188] study the electrical transport properties of $TiFe_2Sn$ compounds below 400 K and measured power factors of 1-2 $\times 10^{-4}$ $Wm^{-1}K^{-2}$ at 300 K, which is close to that of the well-researched TiNiSn half-Heusler compound.[189]

To the best of our knowledge, the transport properties of $TiFe_2Sn$ compounds in the medium temperature range (above 400 K) have not been reported yet. Besides, the Seebeck coefficient of $TiFe_2Sn$ compounds is only about 20 - 30 μVK^{-1}, which is much lower than that of good half-Heusler thermoelectrics (c.f. TiCoSb, ZrNiSn, NbFeSb[100, 152, 190, 191]). Thus, we try to understand the structure–property relation of $TiFe_2Sn$ to tune the Seebeck coefficient. We prepare Mn-doped $TiFe_{2-x}Mn_xSn$ compounds ($x = 0$, 0.01, 0.0156, 0.0185, 0.02, 0.03, and 0.05) by substituting Mn for Fe in $TiFe_2Sn$, and measure their high temperature transport properties and perform band structure calculations. Both density-functional theory

calculations and the measurement results suggest that appropriate Mn doping increases the power factor. This can be attributed to an increased electrical density of states by electronic structure modifications, benefiting both the electronic conductivity and the Seebeck coefficient.
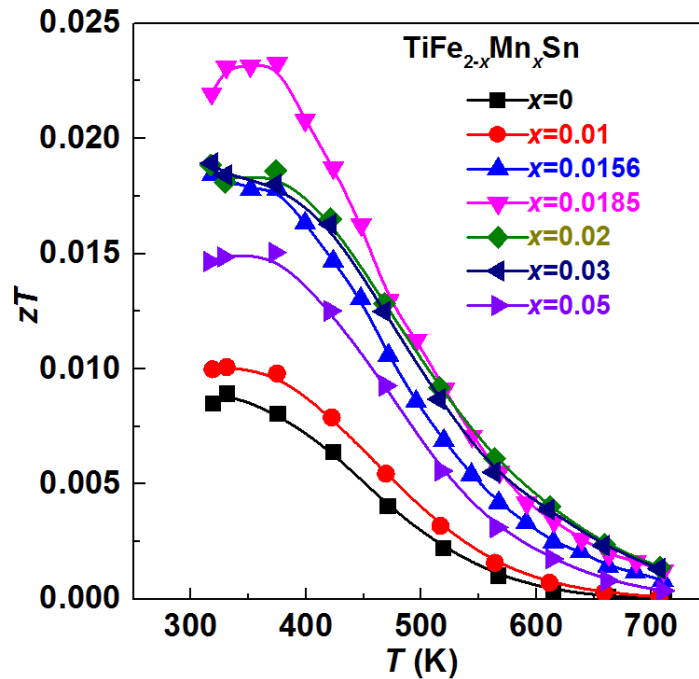
Figure A-8. Temperature dependence of zT of $TiFe_{2-x}Mn_xSn$ specimens.[192]

Because of both increased power factor and decreased thermal conductivity, zT values of all the samples are enhanced compared to pristine $TiFe_2Sn$ shown in **Figure A-8**. Specifically, a $zT = 0.022$ at 375 K is achieved for the sample with 1.85 % manganese doping on the Fe position, which is about 2.6 times larger than that of $TiFe_2Sn$. Although the zT value is improve obviously, the absolute value is still very low.

According to our experiment in full-Heusler $Zr_{0.4}Hf_{0.6}Ni_2Sn$ and $TiFe_{2-x}Mn_xSn$, we can get the conclusion that full-Heusler is not a good candidate for thermoelectric applications.

A.4 Conclusions

In summary, the thermoelectric properties of $Zr_{0.4}Hf_{0.6}Ni_2Sn$ and $Zr_{0.4}Hf_{0.6}Ni_{1.98}Cu_{0.02}Sn$ have been studied at temperature range 300 K $< T <$ 775 K. The figure of merit zT for Cu doped sample is worse than that of the pristine sample. The thermoelectric properties of Mn-doped $TiFe_{2-x}Mn_xSn$ compounds ($x = 0$, 0.01, 0.0156, 0.0185, 0.02, 0.03, and 0.05) have been studied as well. The experimental results from both $Zr_{0.4}Hf_{0.6}Ni_2Sn$ and $TiFe_2Sn$ show that full-Heusler is not a good candidate for thermoelectric applications.

Appendix B X-ray Photoelectron Spectroscopy Measurement of

$Zr_{0.4}Hf_{0.6}NiSn$:xCu
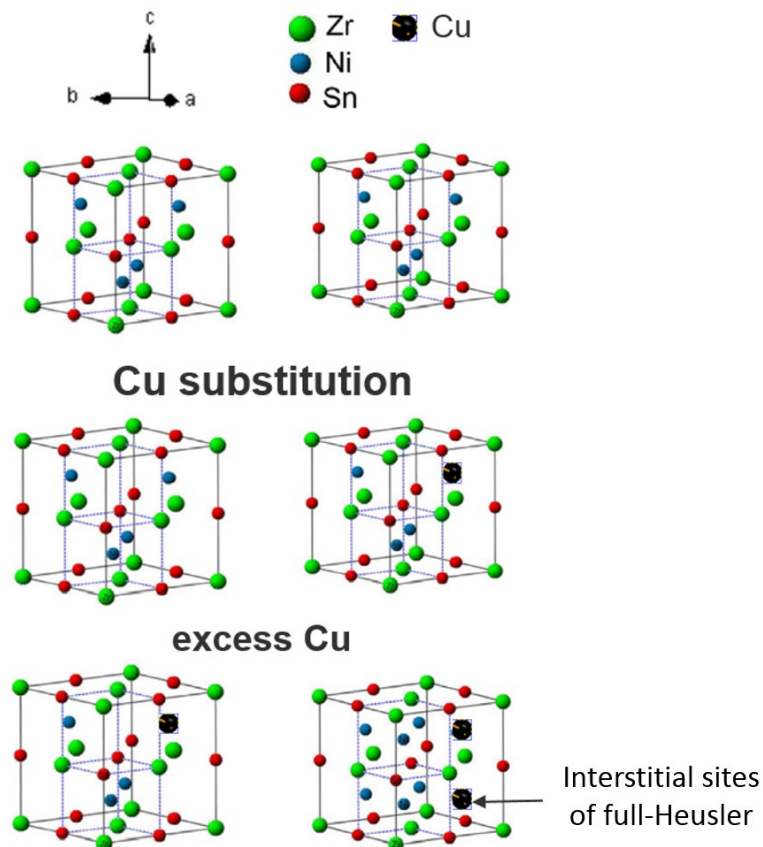
Figure B-1. The possible positions of Cu in the Cu substitution and excess Cu experiments.

To get more information about Cu in the compounds $Zr_{0.4}Hf_{0.6}NiSn$:xCu, we do the X-ray photoelectron spectroscopy (XPS) experiment to determine the chemical state of the Cu element in the compounds.

As shown in **Figure B-1**, for the Cu substitution samples $Zr_{0.4}Hf_{0.6}Ni_{1-x}Cu_xSn$, normally Cu atoms will substitute the Ni atoms in this experiment. In the excess Cu experiments, there are three possibilities. One possibility is Cu will substitute Ni, and the excess Ni will occupy the interstitial sites of the full-Heusler. Another possibility is Cu will occupy the interstitial sites of the full-Heusler. The third possibility is the most normal case, some Cu will substitute the

Ni while some Cu and the excess Ni will occupy the interstitial sites of the full-Heusler phases. In the most normal case, the expression can be written as $Zr_{0.4}Hf_{0.6}Ni_{1-x}Cu_{x+y}Sn$.
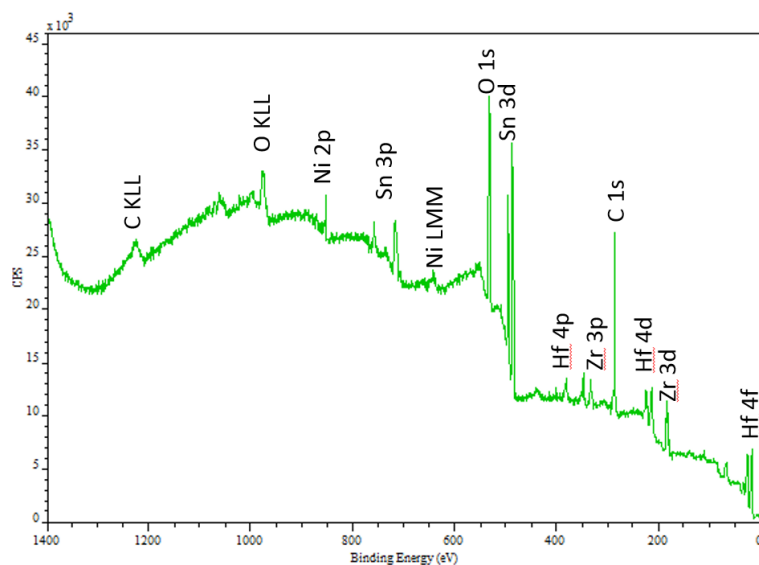
Figure B-2. Counts per second as a function of binding energy in the sample $Zr_{0.4}Hf_{0.6}NiSn$.
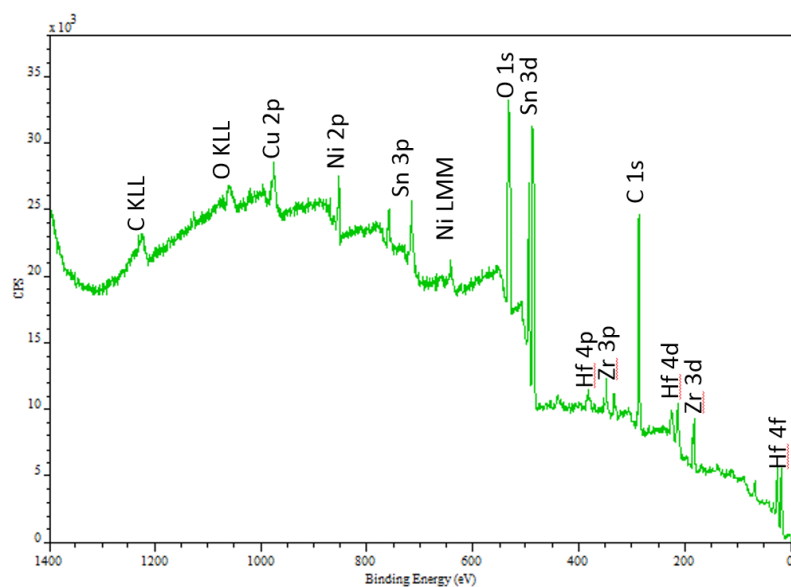
Figure B-3. Counts per second as a function of binding energy in the sample $Zr_{0.4}Hf_{0.6}NiSn:0.02Cu$.

126
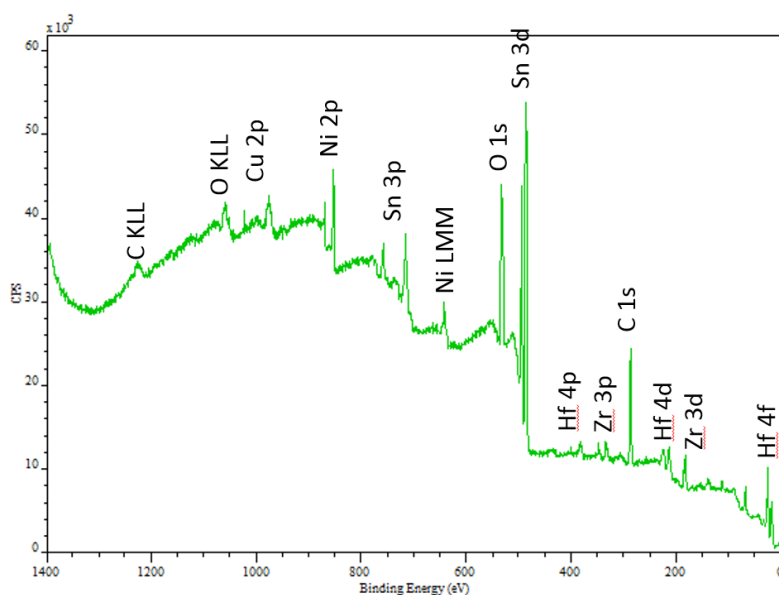
Figure B-4. Counts per second as a function of binding energy in the sample $Zr_{0.4}Hf_{0.6}NiSn:0.05Cu$.

The overall information of counts per second as a function of binding energy in the samples $Zr_{0.4}Hf_{0.6}NiSn$, $Zr_{0.4}Hf_{0.6}NiSn:0.02Cu$ and $Zr_{0.4}Hf_{0.6}NiSn:0.05Cu$ are shown in **Figures B-2, B-3** and **B-4** respectively. From the spectra, there is a significant amount of oxidized material in all the samples. This can be checked by the two different components visible in all spectra. Following we will discuss the information about all the elements in details:

For Sn, the peaks at 484.88 eV and 493.31 eV are metallic Sn and the peaks at 486.64 eV and 495.05 eV are oxidized Sn. For Zr, the peaks at 179.54 eV and 181.97 eV are metallic and the ones at 182.56 eV and 184.93 eV are oxides. For Hf, the peak at 15.05 eV and 16.73 eV are metallic Hf and the ones at 17.14 eV and 18.79 eV are oxidized Hf. For transition metals like Ni and Cu, the determination of the oxidation state by the chemical shift is not so easy.
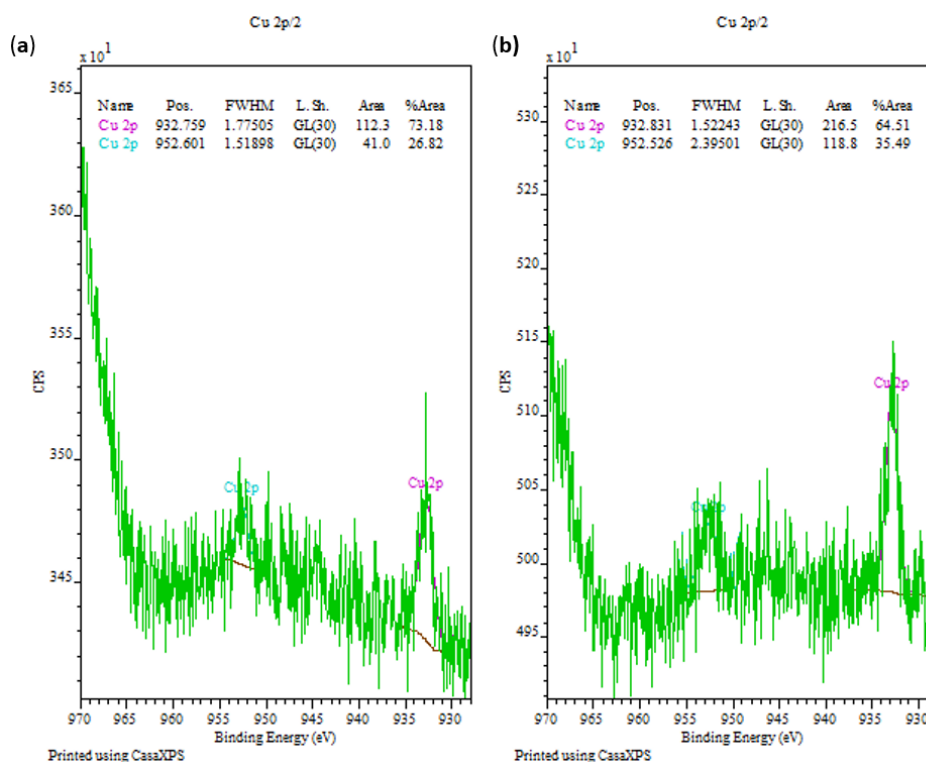
Figure B-5. Counts per second of Cu as a function of binding energy in the samples $Zr_{0.4}Hf_{0.6}NiSn:0.02Cu$ and $Zr_{0.4}Hf_{0.6}NiSn:0.05Cu$.

There is very little copper in the $Zr_{0.4}Hf_{0.6}NiSn:0.02Cu$ and $Zr_{0.4}Hf_{0.6}NiSn:0.05Cu$ samples. However it is impossible to determine the chemical state of the Cu element in the compounds through XPS. The detailed results are shown in **Figure B-5**. The binding energies of metallic copper (932.6 eV), CuO (933.5 eV) and Cu_2O (932.6 eV) are quite similar and it is not possible to distinguish the oxidation state / chemical environment of the copper in the experiment. Usually the chemical states of copper are different in the different chemical components. The chemical state of copper can be determined by satellite peaks which are at high binding energy. However in this experiment, maybe due to small amount of copper these satellites are not visible.

Appendix C List of Publications

C.1 Manuscript in preparation

1. **T. H. Zou**, W. J. Xie, and A. Weidenkaff *et al. Engaging light valence band and phonon scattering via Sm doping in Cu_3SbSe_4*, Manuscript in preparation.

2. **T. H. Zou**, W. J. Xie, and A. Weidenkaff *et al. Enhanced point defects scattering in $(CuSm)_3Sb(SeS)_4$ via Sm and S co-doping*, Manuscript in preparation.

3. **T. H. Zou**, W. J. Xie, and A. Weidenkaff *et al. Extraordinary role of Cu in enhancing the thermoelectric performance of n-type half-Heusler*, Manuscript in preparation.

4. **T. H. Zou**, W. J. Xie, and A. Weidenkaff *et al. Thermoelectric properties enhancement in Heusler-phase $TiFe_2Sn$ via nano-micro-porous structure*, Manuscript in preparation.

C.2 Peer-reviewed papers

1. **T. H. Zou**, T. T. Jia, W. J. Xie, Y. S. Zhang, M. Widenmeyer, X. X. Xiao, and A. Weidenkaff, *Band structure modification of the thermoelectric Heusler-phase $TiFe_2Sn$ via Mn substitution.* Physical Chemistry Chemical Physics, 2017. **19**(28): p. 18273-18278. **(Hot paper)**

2. **T. H. Zou**, X. Y. Qin, Y. S. Zhang, X. G. Li, Z. Zeng, D. Li, J. Zhang, H. X. Xin, W. J. Xie, and A. Weidenkaff, *Enhanced thermoelectric performance of β-Zn_4Sb_3 based nanocomposites through combined effects of density of states resonance and carrier energy filtering.* Scientific Reports, 2015. **5**: p. 17803.

3. **T. H. Zou**, W. J. Xie, X. Y. Qin, M. H. Zhou, M. Widenmeyer, J. J. Xu, J. He, and A. Weidenkaff, *Synergistic effects of Lanthanum substitution on enhancing the thermoelectric properties of β-Zn_4Sb_3.* Journal of Materiomics, 2016. **2**(3): p. 273-279.

4. **T. H. Zou**, W. J. Xie, J. Feng, X. Y. Qin, and A. Weidenkaff, *Recent developments in β-Zn_4Sb_3 based thermoelectric compounds.* Journal of Nanomaterials, 2015. **16**(1): p. 348.

5. **T. H. Zou**, X. Y. Qin, D. Li, G. L. Sun, Y. C. Dou, Q. Q. Wang, B. J. Ren, J. Zhang, H.

X. Xin, and Y. Y. Li, *Simultaneous enhancement in thermoelectric power factor and phonon blocking in hierarchical nanostructured β-Zn₄Sb₃-Cu₃SbSe₄.* Applied Physics Letters, 2014. **104**(1): p. 013904.

6. **T. H. Zou**, X. Y. Qin, D. Li, B. J. Ren, G. L. Sun, Y. C. Dou, Y. Y. Li, L. L. Li, J. Zhang, and H. X. Xin, *Enhanced thermoelectric performance via carrier energy filtering effect in β-Zn₄Sb₃ alloy bulk embedded with (Bi₂Te₃)₀.₂(Sb₂Te₃)₀.₈.* Journal of Applied Physics, 2014. **115**(5): p. 053710.

7. **T. H. Zou**, X. Y. Qin, D. Li, L. L. Li, G. L. Sun, Q. Q. Wang, J. Zhang, H. X. Xin, Y. F. Liu, and C. J. Song, *Enhanced thermoelectric performance of β-Zn₄Sb₃ based composites incorporated with large proportion of nanophase Cu₃SbSe₄.* Journal of Alloys and Compounds, 2014. **588**: p. 568-572.

8. X. X. Xiao, M. Widenmeyer, W. J. Xie, **T. H. Zou**, S. H. Yoon, M. Scavini, S. Checchia, Z. C. Zhong, P. Hansmann, and S. Kilper, *Tailoring the structure and thermoelectric properties of BaTiO₃ via Eu²⁺ substitution.* Physical Chemistry Chemical Physics, 2017. **19**: p. 13469-13480. **(Frontier paper)**

9. Y. Y. Li, Y. C. Dou, X. Y. Qin, J. Zhang, H. X. Xin, D. Li, C. J. Song, **T. H. Zou**, Y. F. Liu, and C. Li, *Enhanced thermoelectric figure of merit in p-type β-Zn₄Sb₃/Bi₀.₄Sb₁.₆Te₃ nanocomposites.* RSC Advances, 2016. **6**(15): p. 12243-12248.

10. B. J. Ren, M. Liu, X. G. Li, X. Y. Qin, D. Li, **T. H. Zou**, G. L. Sun, Y. Y. Li, H. X. Xin, and J. Zhang, *Enhancement of thermoelectric performance of β-Zn₄Sb₃ through resonant distortion of electronic density of states doped with Gd.* Journal of Materials Chemistry A, 2015. **3**(22): p. 11768-11772.

11. J. Zhang, X. Y. Qin, D. Li, C. J. Song, X. G. Zhu, Y. F. Liu, H. X. Xin, L. Chen, and **T. H. Zou**, *Enhanced thermoelectric performance of CuGaTe₂ by Gd-doping and Te incorporation.* Intermetallics, 2015. **60**: p. 45-49.

12. J. Zhang, X. Y. Qin, D. Li, C. J. Song, Y. F. Liu, H. X. Xin, **T. H. Zou**, and Y. Y. Li, *Optimized thermoelectric properties of AgSbTe₂ through adjustment of fabrication parameters.* Electronic Materials Letters, 2015. **11**(1): p. 133-137.

13. G. L. Sun, X. Y. Qin, D. Li, J. Zhang, B. J. Ren, **T. H. Zou**, H. X. Xin, S. B. Paschen,

and X. L. Yan, *Enhanced thermoelectric performance of n-type Bi₂Se₃ doped with Cu.* Journal of Alloys and Compounds, 2015. **639**: p. 9-14.

14. G. L. Sun, L. L. Li, X. Y. Qin, D. Li, **T. H. Zou**, H. X. Xin, B. J. Ren, J. Zhang, Y. Y. Li, and X. J. Li, *Enhanced thermoelectric performance of nanostructured topological insulator Bi₂Se₃.* Applied Physics Letters, 2015. **106**(5): p. 053102.

15. D. Li, X. Y. Qin, **T. H. Zou**, J. Zhang, B. J. Ren, C. J. Song, Y. F. Liu, L. Wang, H. X. Xin, and J. C. Li, *High thermoelectric properties for Sn-doped AgSbSe₂.* Journal of Alloys and Compounds, 2015. **635**: p. 87-91.

16. D. Li, X. Y. Qin, Y. F. Liu, C. J. Song, L. Wang, J. Zhang, H. X. Xin, G. L. Guo, **T. H. Zou**, and G. L. Sun, *Chemical synthesis of nanostructured Cu₂Se with high thermoelectric performance.* RSC Advances, 2014. **4**(17): p. 8638-8644.

17. D. Li, R. Li, X. Y. Qin, C. J. Song, H. X. Xin, L. Wang, J. Zhang, G. l. Guo, **T. H. Zou**, and Y. F. Liu, *Co-precipitation synthesis of nanostructured Cu₃SbSe₄ and its Sn-doped sample with high thermoelectric performance.* Dalton Trans, 2014. **43**(4): p. 1888-1896.

18. L. L. Li, X. Y. Qin, Y. F. Liu, H. X. Xin, J. Zhang, D. Li, C. J. Song, G. L. Guo, Y. C. Dou, and **T. H. Zou**, *Fabrication and thermoelectric properties of n-type (Sr₀.₉Gd₀.₁)TiO₃ oxides.* Functional Materials Letters, 2014. **7**(02): p. 1450014.

19. Q. Q. Wang, X. Y. Qin, D. Li, and **T. H. Zou**, *Enhancement of thermopower and thermoelectric performance through resonant distortion of electronic density of states of β-Zn₄Sb₃ doped with Sm.* Applied Physics Letters, 2013. **102**(15): p. 154101.

20. Q. Q. Wang, X. Y. Qin, D. Li, R. R. Sun, **T. H. Zou**, and N. N. Wang, *Resonant distortion of electronic density of states and enhancement of thermoelectric properties of β-Zn₄Sb₃ by Pr doping.* Journal of Applied Physics, 2013. **113**(12): p. 124901.

21. Y. C. Dou, X. Y. Qin, D. Li, L. L. Li, **T. H. Zou**, and Q. Q. Wang, *Enhanced thermopower and thermoelectric performance through energy filtering of carriers in (Bi₂Te₃)₀.₂(Sb₂Te₃)₀.₈ bulk alloy embedded with amorphous SiO₂ nanoparticles.* Journal of Applied Physics, 2013. **114**(4): p. 044906.

Bibliography

1.   L. E. Bell, *Cooling, heating, generating power, and recovering waste heat with thermoelectric systems.* Science, 2008. **321**(5895): p. 1457-1461.

2.   X. Zhang and L. D. Zhao, *Thermoelectric materials: energy conversion between heat and electricity.* Journal of Materiomics, 2015. **1**(2): p. 92-105.

3.   C. Wood, *Materials for thermoelectric energy conversion.* Reports on Progress in Physics, 1988. **51**(4): p. 459.

4.   H. Lee, *The Thomson effect and the ideal equation on thermoelectric coolers.* Energy, 2013. **56**: p. 61-69.

5.   B. C. Sales, *Smaller is cooler.* Science, 2002. **295**(5558): p. 1248-1249.

6.   T. M. Tritt, *Thermoelectric phenomena, materials, and applications.* Annual Review of Materials Research, 2011. **41**: p. 433-448.

7.   H. J. Goldsmid, *Introduction to thermoelectricity*. Vol. 121. 2010: Springer. p. 46.

8.   T. J. Zhu, C. G. Fu, H. H. Xie, Y. T. Liu, and X. B. Zhao, *High efficiency half‐Heusler thermoelectric materials for energy harvesting.* Advanced Energy Materials, 2015. **5**(19): p. 1500588.

9.   A. Weidenkaff, *Thermoelectrics: Better half found.* Nature Energy, 2017. **2**: p. 17010.

10.   L. D. Zhao, G. J. Tan, S. Q. Hao, J. Q. He, Y. L. Pei, H. Chi, H. Wang, S. K. Gong, H. B. Xu, and V. P. Dravid, *Ultrahigh power factor and thermoelectric performance in hole-doped single-crystal SnSe.* Science, 2015: p. aad3749.

11.   Y. T. Qiu, L. L. Xi, X. Shi, P. F. Qiu, W. Q. Zhang, L. D. Chen, J. R. Salvador, J. Y. Cho, J. H. Yang, and Y. C. Chien, *Charge‐compensated compound defects in Ga‐containing thermoelectric skutterudites.* Advanced Functional Materials, 2013. **23**(25): p. 3194-3203.

12.   S. Q. Bai, Y. Z. Pei, L. D. Chen, W. Q. Zhang, X. Y. Zhao, and J. Yang, *Enhanced thermoelectric performance of dual-element-filled skutterudites $Ba_xCe_yCo_4Sb_{12}$.* Acta Materialia, 2009. **57**(11): p. 3135-3139.

13. C. G. Fu, T. J. Zhu, Y. Z. Pei, H. H. Xie, H. Wang, G. J. Snyder, Y. Liu, Y. T. Liu, and X. B. Zhao, *High band degeneracy contributes to high thermoelectric performance in p‑type half‑Heusler compounds.* Advanced Energy Materials, 2014. **4**(18): p. 1400600.

14. S. Bajaj, H. Wang, J. W. Doak, C. Wolverton, and G. J. Snyder, *Calculation of dopant solubilities and phase diagrams of X–Pb–Se (X= Br, Na) limited to defects with localized charge.* Journal of Materials Chemistry C, 2016. **4**(9): p. 1769-1775.

15. Y. L. Tang, Y. T. Qiu, L. L. Xi, X. Shi, W. Q. Zhang, L. D. Chen, S. M. Tseng, S. W. Chen, and G. J. Snyder, *Phase diagram of In–Co–Sb system and thermoelectric properties of In-containing skutterudites.* Energy & Environmental Science, 2014. **7**(2): p. 812-819.

16. Z. Starý, J. Horak, M. Stordeur, and M. Stölzer, *Antisite defects in $Sb_{2-x}Bi_xTe_3$ mixed crystals.* Journal of Physics and Chemistry of Solids, 1988. **49**(1): p. 29-34.

17. J. Horak, Z. Stary, P. Lošťák, and J. Pancíř, *Antisite defects in n-Bi_2Se_3 crystals.* Journal of Physics and Chemistry of Solids, 1990. **51**(12): p. 1353-1360.

18. L. Ivanova and Y. V. Granatkina, *Properties of single crystals in the Sb_2Te_3-Bi_2Te_3 solid-solution system.* Inorganic Materials, 1995. **31**(6): p. 678-681.

19. Z. Starý, J. Horak, M. Stordeur, and M. Stölzer, *Antisite defects in $Sb_{2-x}Bi_xTe_3$ mixed crystals.* Journal of Physics and Chemistry of Solids, 1988. **49**(1): p. 29-34.

20. U. Birkholz, *Untersuchung der intermetallischen Verbindung Bi_2Te_3 sowie der festen Lösungen $Bi_{2-x}Sb_xTe_3$ und $Bi_2Te_{3-x}Se_x$ hinsichtlich ihrer Eignung als Material für Halbleiter-Thermoelemente.* Zeitschrift für Naturforschung A, 1958. **13**(9): p. 780-792.

21. V. I. Fistul, *Transport phenomena in heavily doped semiconductors*, in *Heavily Doped Semiconductors*. 1969, Springer. p. 77-205.

22. D. G. Cahill, S. K. Watson, and R. O. Pohl, *Lower limit to the thermal conductivity of disordered crystals.* Physical Review B, 1992. **46**(10): p. 6131.

23. I. I. Ravich, *Semiconducting lead chalcogenides.* Vol. 5. 2013: Springer Science & Business Media. p. 122.

24. D. K. Ferry, *Semiconductors: Bonds and bands*. 2013: IOP Publishing Ltd. p. 54.

25. H. J. Goldsmid, *Electronic refrigeration*. 1986: Pion. p. 22.

26. B. Yu, M. Zebarjadi, H. Wang, K. Lukas, H. Z. Wang, D. Z. Wang, C. Opeil, M. Dresselhaus, G. Chen, and Z. F. Ren, *Enhancement of thermoelectric properties by modulation-doping in silicon germanium alloy nanocomposites*. Nano Letters, 2012. **12**(4): p. 2077-2082.

27. M. Zebarjadi, G. Joshi, G. H. Zhu, B. Yu, A. Minnich, Y. C. Lan, X. W. Wang, M. Dresselhaus, Z. F. Ren, and G. Chen, *Power factor enhancement by modulation doping in bulk nanocomposites*. Nano Letters, 2011. **11**(6): p. 2225-2230.

28. M. S. Dresselhaus, G. Chen, M. Y. Tang, R. G. Yang, H. Lee, D. Z. Wang, Z. F. Ren, J. P. Fleurial, and P. Gogna, *New directions for low‐dimensional thermoelectric materials*. Advanced Materials, 2007. **19**(8): p. 1043-1053.

29. R. Delves, A. Bowley, D. Hazelden, and H. Goldsmid, *Anisotropy of the electrical conductivity in bismuth telluride*. Proceedings of the Physical Society, 1961. **78**(5): p. 838.

30. J. J. Shen, L. P. Hu, T. J. Zhu, and X. B. Zhao, *The texture related anisotropy of thermoelectric properties in bismuth telluride based polycrystalline alloys*. Applied Physics Letters, 2011. **99**(12): p. 124102.

31. L. P. Hu, T. J. Zhu, Y. G. Wang, H. H. Xie, Z. J. Xu, and X. B. Zhao, *Shifting up the optimum figure of merit of p-type bismuth telluride-based thermoelectric materials for power generation by suppressing intrinsic conduction*. NPG Asia Materials, 2014. **6**: p. e88.

32. J. H. Sui, J. Li, J. Q. He, Y. L. Pei, D. Berardan, H. J. Wu, N. Dragoe, W. Cai, and L. D. Zhao, *Texturation boosts the thermoelectric performance of BiCuSeO oxyselenides*. Energy & Environmental Science, 2013. **6**(10): p. 2916-2920.

33. J. P. Heremans, C. M. Thrush, and D. T. Morelli, *Thermopower enhancement in PbTe with pb precipitates*. Journal of Applied Physics, 2005. **98**(6): p. 063703.

34. J. P. Heremans, C. M. Thrush, and D. T. Morelli, *Thermopower enhancement in lead*

telluride nanostructures. Physical Review B, 2004. **70**(11): p. 115334.

35. J. P. Heremans, V. Jovovic, E. S. Toberer, A. Saramat, K. Kurosaki, A. Charoenphakdee, S. Yamanaka, and G. J. Snyder, *Enhancement of thermoelectric efficiency in PbTe by distortion of the electronic density of states.* Science, 2008. **321**(5888): p. 554-7.

36. Y. Z. Pei, X. Shi, A. LaLonde, H. Wang, L. Chen, and G. J. Snyder, *Convergence of electronic bands for high performance bulk thermoelectrics.* Nature, 2011. **473**(7345): p. 66-9.

37. Y. Z. Pei, H. Wang, and G. J. Snyder, *Band engineering of thermoelectric materials.* Advanced Materials, 2012. **24**(46): p. 6125-35.

38. Y. L. Tang, Z. M. Gibbs, L. A. Agapito, G. D. Li, H. S. Kim, M. B. Nardelli, S. Curtarolo, and G. J. Snyder, *Convergence of multi-valley bands as the electronic origin of high thermoelectric performance in $CoSb_3$ skutterudites.* Nature Materials, 2015. **14**(12): p. 1223-8.

39. M. F. O'Dwyer, R. Lewis, C. Zhang, and T. Humphrey, *Electronic efficiency in nanostructured thermionic and thermoelectric devices.* Physical Review B, 2005. **72**(20): p. 205330.

40. D. Medlin and G. Snyder, *Interfaces in bulk thermoelectric materials: a review for current opinion in colloid and interface science.* Current Opinion in Colloid & Interface Science, 2009. **14**(4): p. 226-235.

41. Y. Nishio and T. Hirano, *Improvement of the efficiency of thermoelectric energy conversion by utilizing potential barriers.* Japanese Journal of Applied Physics, 1997. **36**(1R): p. 170.

42. A. Shakouri, *Recent developments in semiconductor thermoelectric physics and materials.* Annual Review of Materials Research, 2011. **41**: p. 399-431.

43. M. Zebarjadi, K. Esfarjani, A. Shakouri, J.H. Bahk, Z. Bian, G. Zeng, J. Bowers, H. Lu, J. Zide, and A. Gossard, *Effect of nanoparticle scattering on thermoelectric power factor.* Applied Physics Letters, 2009. **94**(20): p. 202105.

44. S. Wang and N. Mingo, *Tailoring interface roughness and superlattice period length*

in electron-filtering thermoelectric materials. Physical Review B, 2009. **79**(11): p. 115316.

45. A. J. Minnich, M. S. Dresselhaus, Z. F. Ren, and G. Chen, *Bulk nanostructured thermoelectric materials: current research and future prospects.* Energy & Environmental Science, 2009. **2**(5): p. 466.

46. M. Ohtaki and R. Hayashi. *Enhanced thermoelectric performance of nanostructured ZnO: a possibility of selective phonon scattering and carrier energy filtering by nanovoid structure.* in *25th International Conference on Thermoelectrics.* 2006. IEEE: p. 276-279.

47. J. H. Bahk, Z. X. Bian, and A. Shakouri, *Electron energy filtering by a nonplanar potential to enhance the thermoelectric power factor in bulk materials.* Physical Review B, 2013. **87**(7): p. 075204.

48. M. Zebarjadi, Z. X. Bian, R. Singh, A. Shakouri, R. Wortman, V. Rawat, and T. Sands, *Thermoelectric transport in a ZrN/ScN superlattice.* Journal of Electronic Materials, 2009. **38**(7): p. 960-963.

49. Z. Xiong, X. H. Chen, X. Y. Huang, S. Q. Bai, and L. D. Chen, *High thermoelectric performance of $Yb_{0.26}Co_4Sb_{12}/yGaSb$ nanocomposites originating from scattering electrons of low energy.* Acta Materialia, 2010. **58**(11): p. 3995-4002.

50. Z. Xiong, X. H. Chen, X. Y. Zhao, S. Q. Bai, X. Y. Huang, and L. D. Chen, *Effects of nano-TiO_2 dispersion on the thermoelectric properties offilled-skutterudite $Ba_{0.22}Co_4Sb_{12}$.* Solid State Sciences, 2009. **11**(9): p. 1612-1616.

51. D. Vashaee and A. Shakouri, *Improved thermoelectric power factor in metal-based superlattices.* Physical Review Letters, 2004. **92**(10): p. 106103.

52. S. V. Faleev and F. Léonard, *Theory of enhancement of thermoelectric properties of materials with nanoinclusions.* Physical Review B, 2008. **77**(21): p. 214304.

53. E. Gratz and M. Zuckermann, *Transport properties (electrical resistivity, thermoelectric power and thermal conductivity) of rare earth intermetallic compounds.* Handbook on the physics and chemistry of rare earths, 1982. **5**: p. 117-216.

54. J. Korringa and A. Gerritsen, *The cooperative electron phenomenon in dilute alloys.*

Physica, 1953. **19**(1): p. 457-507.

55. P. De Gennes and J. Friedel, *Anomalies de résistivité dans certains métaux magníques.* Journal of Physics and Chemistry of Solids, 1958. **4**(1): p. 71-77.

56. T. Moriya, *Recent progress in the theory of itinerant electron magnetism.* Journal of Magnetism and Magnetic Materials, 1979. **14**(1): p. 1-46.

57. L. Hicks and M. Dresselhaus, *Thermoelectric figure of merit of a one-dimensional conductor.* Physical Review B, 1993. **47**(24): p. 16631.

58. G. Mahan and J. Sofo, *The best thermoelectric.* Proceedings of the National Academy of Sciences, 1996. **93**(15): p. 7436-7439.

59. J. P. Heremans, B. Wiendlocha, and A. M. Chamoire, *Resonant levels in bulk thermoelectric semiconductors.* Energy & Environmental Science, 2012. **5**(2): p. 5510.

60. M. Liu, X. Y. Qin, C. S. Liu, and Z. Zeng, *Enhanced thermoelectric power factor with impurity-induced resonant level.* Applied Physics Letters, 2011. **99**(6): p. 062112.

61. C. M. Jaworski, B. Wiendlocha, V. Jovovic, and J. P. Heremans, *Combining alloy scattering of phonons and resonant electronic levels to reach a high thermoelectric figure of merit in PbTeSe and PbTS alloys.* Energy & Environmental Science, 2011. **4**(10): p. 4155-4162.

62. J. Androulakis, I. Todorov, D. Y. Chung, S. Ballikaya, G. Wang, C. Uher, and M. Kanatzidis, *Thermoelectric enhancement in PbTe with K or Na codoping from tuning the interaction of the light-and heavy-hole valence bands.* Physical Review B, 2010. **82**(11): p. 115209.

63. M. G. Kanatzidis, *Nanostructured thermoelectrics: the new paradigm?* Chemistry of Materials, 2009. **22**(3): p. 648-659.

64. T. J. Zhu, Y. T. Liu, C. G. Fu, J. P. Heremans, J. G. Snyder, and X. B. Zhao, *Compromise and synergy in high‐efficiency thermoelectric materials.* Advanced Materials, 2017: p. 1605884.

65. K. Biswas, J. He, I. D. Blum, C. I. Wu, T. P. Hogan, D. N. Seidman, V. P. Dravid, and M. G. Kanatzidis, *High-performance bulk thermoelectrics with all-scale hierarchical*

architectures. Nature, 2012. **489**(7416): p. 414-8.

66. Z. H. Liu, Y. M. Wang, J. Mao, H. Y. Geng, J. Shuai, Y. X. Wang, R. He, W. Cai, J. H. Sui, and Z. F. Ren, *Lithium doping to enhance thermoelectric performance of MgAgSb with weak electron-phonon coupling.* Advanced Energy Materials, 2016. **6**(7): p. 1502269.

67. H. Wang, A. D. LaLonde, Y. Pei, and G. J. Snyder, *The criteria for beneficial disorder in thermoelectric solid solutions.* Advanced Functional Materials, 2013. **23**(12): p. 1586-1596.

68. L. P. Hu, T. J. Zhu, X. H. Liu, and X. B. Zhao, *Point defect engineering of high‐performance Bismuth‐Telluride‐based thermoelectric materials.* Advanced Functional Materials, 2014. **24**(33): p. 5211-5218.

69. W. J. Xie, J. He, H. J. Kang, X. F. Tang, S. Zhu, M. Laver, S. Y. Wang, J. R. Copley, C. M. Brown, and Q. J. Zhang, *Identifying the specific nanostructures responsible for the high thermoelectric performance of (Bi, Sb)$_2$Te$_3$ nanocomposites.* NanoLetters, 2010. **10**(9): p. 3283-3289.

70. B. Poudel, Q. Hao, Y. Ma, Y. C. Lan, A. Minnich, B. Yu, X. Yan, D. Z. Wang, A. Muto, and D. Vashaee, *High-thermoelectric performance of nanostructured bismuth antimony telluride bulk alloys.* Science, 2008. **320**(5876): p. 634-638.

71. J. Q. He, S. N. Girard, M. G. Kanatzidis, and V. P. Dravid, *Microstructure‐lattice thermal conductivity correlation in nanostructured PbTe$_{0.7}$S$_{0.3}$ thermoelectric Materials.* Advanced Functional Materials, 2010. **20**(5): p. 764-772.

72. L. P. Hu, H. J. Wu, T. J. Zhu, C. G. Fu, J. Q. He, P. J. Ying, and X. B. Zhao, *Tuning multiscale microstructures to enhance thermoelectric performance of n‐type Bismuth‐Telluride‐based solid solutions.* Advanced Energy Materials, 2015. **5**(17): p. 1500411.

73. S. I. Kim, K. H. Lee, H. A. Mun, H. S. Kim, S. W. Hwang, J. W. Roh, D. J. Yang, W. H. Shin, X. S. Li, and Y. H. Lee, *Dense dislocation arrays embedded in grain*

boundaries for high-performance bulk thermoelectrics. Science, 2015. **348**(6230): p. 109-114.

74.   C. Y. Yang, F. Q. Huang, L. M. Wu, and K. Xu, *New stannite-like p-type thermoelectric material Cu₃SbSe₄.* Journal of Physics D: Applied Physics, 2011. **44**(29): p. 295404.

75.   F. Casper, T. Graf, S. Chadov, B. Balke, and C. Felser, *Half-Heusler compounds: novel materials for energy and spintronic applications.* Semiconductor Science and Technology, 2012. **27**(6): p. 063001.

76.   W. J. Xie, A. Weidenkaff, X. F. Tang, Q. J. Zhang, J. Poon, and T. M. Tritt, *Recent advances in nanostructured thermoelectric half-Heusler compounds.* Nanomaterials, 2012. **2**(4): p. 379-412.

77.   Y. S. Zhang, E. Skoug, J. Cain, V. Ozoliņš, D. Morelli, and C. Wolverton, *First-principles description of anomalously low lattice thermal conductivity in thermoelectric Cu-Sb-Se ternary semiconductors.* Physical Review B, 2012. **85**(5): p. 054306.

78.   E. J. Skoug, J. D. Cain, and D. T. Morelli, *High thermoelectric figure of merit in the Cu₃SbSe₄-Cu₃SbS₄ solid solution.* Applied Physics Letters, 2011. **98**(26): p. 261911.

79.   Y. Y. Li, X. Y. Qin, D. Li, X. Y. Li, Y. F. Liu, J. Zhang, C. J. Song, and H. X. Xin, *Transport properties and enhanced thermoelectric performance of aluminum doped Cu₃SbSe₄.* RSC Advances, 2015. **5**(40): p. 31399-31403.

80.   T. R. Wei, H. Wang, Z. M. Gibbs, C. F. Wu, G. J. Snyder, and J. F. Li, *Thermoelectric properties of Sn-doped p-type Cu₃SbSe₄: a compound with large effective mass and small band gap.* Journal of Materials Chemistry A, 2014. **2**(33): p. 13527.

81.   X. Y. Li, D. Li, H. X. Xin, J. Zhang, C. J. Song, and X. Y. Qin, *Effects of bismuth doping on the thermoelectric properties of Cu₃SbSe₄ at moderate temperatures.* Journal of Alloys and Compounds, 2013. **561**: p. 105-108.

82.   D. Zhang, J. Y. Yang, Q. H. Jiang, L. W. Fu, Y. Xiao, Y. B. Luo, and Z. W. Zhou, *Improvement of thermoelectric properties of Cu₃SbSe₄ compound by In doping.* Materials & Design, 2016. **98**: p. 150-154.

83.   A. Kumar, P. Dhama, D. S. Saini, and P. Banerji, *Effect of Zn substitution at a Cu site*

on the transport behavior and thermoelectric properties in Cu_3SbSe_4. RSC Advances, 2016. **6**(7): p. 5528-5534.

84.   D. T. Do and S. Mahanti, *Theoretical study of defects Cu_3SbSe_4: Search for optimum dopants for enhancing thermoelectric properties.* Journal of Alloys and Compounds, 2015. **625**: p. 346-354.

85.   H. C. Kandpal, C. Felser, and R. Seshadri, *Covalent bonding and the nature of band gaps in some half-Heusler compounds.* Journal of Physics D: Applied Physics, 2006. **39**(5): p. 776-785.

86.   C. Lee, M. Whangbo, and J. Köhler, *Stuffed graphite-like vs. stuffed diamond-like structures of the 18 valence electron compounds REAuSn (RE = Sc, Y, La-Nd, Sm, Gd-Lu).* Zeitschrift fur Anorganische und Allgemeine Chemie, 2007. **633**(15): p. 2631-2634.

87.   W. Klemm, *Unusual oxidation states.* Angewandte Chemie, 1951. **63**: p. 133-142.

88.   T. Graf, C. Felser, and S. S. P. Parkin, *Simple rules for the understanding of Heusler compounds.* Progress in Solid State Chemistry, 2011. **39**(1): p. 1-50.

89.   W. G. Zeier, J. Schmitt, G. Hautier, U. Aydemir, Z. M. Gibbs, C. Felser, and G. J. Snyder, *Engineering half-Heusler thermoelectric materials using Zintl chemistry.* Nature Reviews Materials, 2016. **1**: p. 16032.

90.   J. Köhler, S. Q. Deng, C. H. Lee, and M. H. Whangbo, *On the origin of a band gap in compounds of diamond-like structures.* Inorganic Chemistry, 2007. **46**(6): p. 1957-1959.

91.   H. H. Xie, C. Yu, B. He, T. J. Zhu, and X. B. Zhao, *Thermoelectric properties and n-to p-type conversion of Co-doped ZrNiSn-based half-Heusler alloys.* Journal of Electronic Materials, 2012. **41**(6): p. 1826.

92.   G. Joshi, X. Yan, H. Z. Wang, W. S. Liu, G. Chen, and Z. F. Ren, *Enhancement in thermoelectric figure of merit of an n‑type half‑Heusler compound by the nanocomposite approach.* Advanced Energy Materials, 2011. **1**(4): p. 643-647.

93.   P. Larson, S. D. Mahanti, and M. G. Kanatzidis, *Structural stability of Ni-containing*

half-Heusler compounds. Physical Review B, 2000. **62**(19): p. 12754.

94. J. Yang, H. M. Li, T. Wu, W. Q. Zhang, L. D. Chen, and J. H. Yang, *Evaluation of half‑Heusler compounds as thermoelectric materials based on the calculated electrical transport properties.* Advanced Functional Materials, 2008. **18**(19): p. 2880-2888.

95. J. H. Ma, V. I. Hegde, K. Munira, Y. K. Xie, S. Keshavarz, D. T. Mildebrath, C. Wolverton, A. W. Ghosh, and W. Butler, *Computational investigation of half-Heusler compounds for spintronics applications.* Physical Review B, 2017. **95**(2): p. 024411.

96. C. Uher, J. H. Yang, S. Hu, D. T. Morelli, and G. P. Meisner, *Transport properties of pure and doped MNiSn (M = Zr, Hf).* Physical Review B, 1999. **59**(13): p. 8615.

97. S. Bhattacharya, A. Pope, R. Littleton IV, T. M. Tritt, V. Ponnambalam, Y. Xia, and S. Poon, *Effect of Sb doping on the thermoelectric properties of Ti-based half-Heusler compounds $TiNiSn_{1−x}Sb_x$.* Applied Physics Letters, 2000. **77**(16): p. 2476-2478.

98. Q. Shen, L. D. Chen, T. Goto, T. Hirai, J. H. Yang, G. Meisner, and C. Uher, *Effects of partial substitution of Ni by Pd on the thermoelectric properties of ZrNiSn-based half-Heusler compounds.* Applied Physics Letters, 2001. **79**(25): p. 4165-4167.

99. S. Sakurada and N. Shutoh, *Effect of Ti substitution on the thermoelectric properties of (Zr,Hf)NiSn half-Heusler compounds.* Applied Physics Letters, 2005. **86**(8): p. 082105.

100. C. Yu, T. J. Zhu, R. Z. Shi, Y. Zhang, X. B. Zhao, and J. He, *High-performance half-Heusler thermoelectric materials $Hf_{1−x}Zr_xNiSn_{1−y}Sb_y$ prepared by levitation melting and spark plasma sintering.* Acta Materialia, 2009. **57**(9): p. 2757-2764.

101. M. Schwall and B. Balke, *Phase separation as a key to a thermoelectric high efficiency.* Physical Chemistry Chemical Physics, 2013. **15**(6): p. 1868-1872.

102. E. Rausch, B. Balke, J. M. Stahlhofen, S. Ouardi, U. Burkhardt, and C. Felser, *Fine tuning of thermoelectric performance in phase-separated half-Heusler compounds.* Journal of Materials Chemistry C, 2015. **3**(40): p. 10409-10414.

103. Y. Kimura, Y. Tamura, and T. Kita, *Thermoelectric properties of directionally*

solidified half-Heusler compound NbCoSn alloys. Applied Physics Letters, 2008. **92**(1): p. 012105.

104. P. F. Qiu, X. Y. Huang, X. H. Chen, and L. D. Chen, *Enhanced thermoelectric performance by the combination of alloying and doping in TiCoSb-based half-Heusler compounds.* Journal of Applied Physics, 2009. **106**(10): p. 103703.

105. J. P. Makongo, D. K. Misra, X. Zhou, A. Pant, M. R. Shabetai, X. Su, C. Uher, K. L. Stokes, and P. F. Poudeu, *Simultaneous large enhancements in thermopower and electrical conductivity of bulk nanostructured half-Heusler alloys.* Journal of the American Chemical Society, 2011. **133**(46): p. 18843-52.

106. Y. W. Chai, T. Oniki, and Y. Kimura, *Microstructure and thermoelectric properties of a ZrNi$_{1.1}$Sn half-Heusler alloy.* Acta Materialia, 2015. **85**: p. 290-300.

107. Y. Wang Chai and Y. Kimura, *Nanosized precipitates in half-Heusler TiNiSn alloy.* Applied Physics Letters, 2012. **100**(3): p. 033114.

108. D. Errandonea, R. Boehler, and M. Ross, *Melting of the rare earth metals and f-electron delocalization.* Physical Review Letters, 2000. **85**(16): p. 3444.

109. E. J. Skoug, J. D. Cain, D. T. Morelli, M. Kirkham, P. Majsztrik, and E. Lara-Curzio, *Lattice thermal conductivity of the Cu$_3$SbSe$_4$-Cu$_3$SbS$_4$ solid solution.* Journal of Applied Physics, 2011. **110**(2): p. 023501.

110. A. Le Bail, H. Duroy, and J. Fourquet, *Ab-initio structure determination of LiSbWO$_6$ by X-ray powder diffraction.* Materials Research Bulletin, 1988. **23**(3): p. 447-452.

111. J. Rodriguez-Carvajal, FULLPROF 2.k, version 5.30, March2012-ILL-JRC, 2012. **22**.

112. W. C. Oliver and G. M. Pharr, *An improved technique for determining hardness and elastic modulus using load and displacement sensing indentation experiments.* Journal of Materials Research, 1992. **7**(06): p. 1564-1583.

113. R. C. Campbell and S. E. Smith, *Flash diffusivity method: a survey of capabilities.* Electronics Cooling, 2002. **8**: p. 34-41.

114. J. Martin, T. M. Tritt, and C. Uher, *High temperature Seebeck coefficient metrology.* Journal of Applied Physics, 2010. **108**(12): p. 14.

115. A. Weidenkaff, *Master of science laboratory course materials science* University of

Stuttgart, 2016: p. 1-5.

116. A. Harris, *Analysis of primer residue from CCI Blazer® lead free ammunition by scanning electron microscopy/energy dispersive X-ray.* Journal of Forensic Science, 1995. **40**(1): p. 27-30.

117. B. Hafner, *Scanning electron microscopy primer.* Characterization Facility, University of Minnesota-Twin Cities, 2007: p. 1-29.

118. *https://www.qdusa.com/products/ppms.html.*

119. *http://www.hk-phy.org/atomic_world/tem/tem02_e.html.*

120. D. B. Williams and C. B. Carter, *The transmission electron microscope*, in *Transmission Electron Microscopy*. 1996, Springer. p. 3-17.

121. *https://www.ifw-dresden.de/institutes/ikm/research-teams-and-topics/micro-and-nanostructures/available-methods/xps/.*

122. W. K. Istone, *X-ray photoelectron spectroscopy (XPS).* 1995: CRC Press. p. 154.

123. J. D. Andrade, *X-ray photoelectron spectroscopy (XPS)*, in *Surface and interfacial aspects of biomedical polymers*. 1985, Springer. p. 105-195.

124. W. S. Liu, J. W. Zhou, Q. Jie, Y. Li, H. S. Kim, J. M. Bao, G. Chen, and Z. F. Ren, *New insight into the material parameter B to understand the enhanced thermoelectric performance of $Mg_2Sn_{1-x-y}Ge_xSb_y$.* Energy & Environmental Science, 2016. **9**(2): p. 530-539.

125. G. A. Slack, *Handbook of thermoelectrics.* CRC Press, Boca Raton, 1995(ed. by M. Rowe): p. 407.

126. A. F. Ioffe, *Physics of semiconductors*. 1960: Infosearch. p. 243.

127. J. Q. He, S. N. Girard, J. C. Zheng, L. D. Zhao, M. G. Kanatzidis, and V. P. Dravid, *Strong phonon scattering by layer structured PbSnS(2) in PbTe based thermoelectric materials.* Advanced Materials, 2012. **24**(32): p. 4440-4.

128. G. Joshi, H. Lee, Y. C. Lan, X. W. Wang, G. H. Zhu, D. Z. Wang, R. W. Gould, D. C. Cuff, M. Y. Tang, and M. S. Dresselhaus, *Enhanced thermoelectric figure-of-merit in nanostructured p-type silicon germanium bulk alloys.* Nano Letters, 2008. **8**(12): p. 4670-4674.

129. H. Liu, X. Shi, F. Xu, L. Zhang, W. Zhang, L. Chen, Q. Li, C. Uher, T. Day, and G. J. Snyder, *Copper ion liquid-like thermoelectrics.* Nature materials, 2012. **11**(5): p. 422-5.

130. C. Barreteau, D. Bérardan, E. Amzallag, L. D. Zhao, and N. Dragoe, *Structural and electronic transport properties in Sr-doped BiCuSeO.* Chemistry of Materials, 2012. **24**(16): p. 3168-3178.

131. Y. L. Pei, J. q. He, J. F. Li, F. Li, Q. J. Liu, W. Pan, C. Barreteau, D. Berardan, N. Dragoe, and L. D. Zhao, *High thermoelectric performance of oxyselenides: intrinsically low thermal conductivity of Ca-doped BiCuSeO.* NPG Asia Materials, 2013. **5**(5): p. e47.

132. G. Kresse and D. Joubert, *From ultrasoft pseudopotentials to the projector augmented-wave method.* Physical Review B, 1999. **59**(3): p. 1758.

133. J. Heyd, G. E. Scuseria, and M. Ernzerhof, *Hybrid functionals based on a screened Coulomb potential.* The Journal of Chemical Physics, 2003. **118**(18): p. 8207-8215.

134. T. R. Wei, F. Li, and J. F. Li, *Enhanced thermoelectric performance of nonstoichiometric compounds $Cu_{3-x}SbSe_4$ by Cu deficiencies.* Journal of Electronic Materials, 2014. **43**(6): p. 2229-2238.

135. H. J. Goldsmid and J. W. Sharp, *Estimation of the thermal band gap of a semiconductor from Seebeck measurements.* Journal of Electronic Materials, 1999. **28**(7): p. 869-872.

136. M. Dressel and G. Grüner, *Electrodynamics of solids: optical properties of electrons in matter.* 2002, Electrodznamics of Solids, Cabridge University Press. p. 332.

137. T. H. Zou, X. Y. Qin, D. Li, G. L. Sun, Y. C. Dou, Q. Q. Wang, B. J. Ren, J. Zhang, H. X. Xin, and Y. Y. Li, *Simultaneous enhancement in thermoelectric power factor and phonon blocking in hierarchical nanostructured β-Zn_4Sb_3-Cu_3SbSe_4.* Applied Physics Letters, 2014. **104**(1): p. 013904.

138. T. H. Zou, W. J. Xie, J. Feng, X. Y. Qin, and A. Weidenkaff, *Recent developments in β-Zn_4Sb_3 based thermoelectric compounds.* Journal of Nanomaterials, 2015. **2015**: p. 1-15.

139. D. Do, V. Ozolins, S. D. Mahanti, M. S. Lee, Y. S. Zhang, and C. Wolverton, *Physics*

of bandgap formation in Cu–Sb–Se based novel thermoelectrics: the role of Sb valency and Cu d levels. Journal of Physics: Condensed Matter, 2012. **24**(41): p. 415502.

140. D. Li, R. Li, X. Y. Qin, C. J. Song, H. X. Xin, L. Wang, J. Zhang, G. L. Guo, T. H. Zou, Y. F. Liu, and X. G. Zhu, *Co-precipitation synthesis of nanostructured Cu₃SbSe₄ and its Sn-doped sample with high thermoelectric performance.* Dalton Trans, 2014. **43**(4): p. 1888-96.

141. E. J. Skoug, J. D. Cain, P. Majsztrik, M. Kirkham, E. Lara-Curzio, and D. T. Morelli, *Doping effects on the thermoelectric properties of Cu₃SbSe₄.* Science of Advanced Materials, 2011. **3**(4): p. 602-606.

142. Y. Z. Pei, A. D. LaLonde, H. Wang, and G. J. Snyder, *Low effective mass leading to high thermoelectric performance.* Energy & Environmental Science, 2012. **5**(7): p. 7963.

143. H. S. Kim, Z. M. Gibbs, Y. L. Tang, H. Wang, and G. J. Snyder, *Characterization of Lorenz number with Seebeck coefficient measurement.* APL Materials, 2015. **3**(4): p. 041506.

144. J. Callaway, *Model for lattice thermal conductivity at low temperatures.* Physical Review, 1959. **113**(4): p. 1046.

145. W. J. Qiu, L. H. Wu, X. Z. Ke, J. H. Yang, and W. Q. Zhang, *Diverse lattice dynamics in ternary Cu-Sb-Se compounds.* Scientific Reports, 2015. **5**: p. 13643.

146. H. H. Xie, H. Wang, Y. Z. Pei, C. G. Fu, X. H. Liu, G. J. Snyder, X. B. Zhao, and T. J. Zhu, *Beneficial contribution of alloy disorder to electron and phonon transport in half-Heusler thermoelectric materials.* Advanced Functional Materials, 2013. **23**(41): p. 5123-5130.

147. J. H. Yang, G. P. Meisner, and L. D. Chen, *Strain field fluctuation effects on lattice thermal conductivity of ZrNiSn-based thermoelectric compounds.* Applied Physics Letters, 2004. **85**(7): p. 1140.

148. H. Goldsmid and A. Penn, *Boundary scattering of phonons in solid solutions.* Physics Letters A, 1968. **27**(8): p. 523-524.

149. G. Chen, M. Dresselhaus, G. Dresselhaus, J. P. Fleurial, and T. Caillat, *Recent*

developments in thermoelectric materials. International Materials Reviews, 2003. **48**(1): p. 45-66.

150. K. Biswas, J. He, I. D. Blum, C. I. Wu, T. P. Hogan, D. N. Seidman, V. P. Dravid, and M. G. Kanatzidis, *High-performance bulk thermoelectrics with all-scale hierarchical architectures.* Nature, 2012. **489**(7416): p. 414-418.

151. B. Poudel, Q. Hao, Y. Ma, Y. Lan, A. Minnich, B. Yu, X. Yan, D. Wang, A. Muto, and D. Vashaee, *High-thermoelectric performance of nanostructured bismuth antimony telluride bulk alloys.* Science, 2008. **320**(5876): p. 634-638.

152. W. J. Xie, J. He, S. Zhu, X. L. Su, S. Y. Wang, T. Holgate, J. W. Graff, V. Ponnambalam, S. J. Poon, and X. F. Tang, *Simultaneously optimizing the independent thermoelectric properties in (Ti, Zr, Hf)(Co, Ni) Sb alloy by in situ forming InSb nanoinclusions.* Acta Materialia, 2010. **58**(14): p. 4705-4713.

153. T. H. Zou, X. Y. Qin, Y. S. Zhang, X. G. Li, Z. Zeng, D. Li, J. Zhang, H. X. Xin, W. J. Xie, and A. Weidenkaff, *Enhanced thermoelectric performance of β-Zn₄Sb₃ based nanocomposites through combined effects of density of states resonance and carrier energy filtering.* Scientific Reports, 2015. **5**: p. 17803.

154. G. Y. Jiang, J. He, T. J. Zhu, C. G. Fu, X. H. Liu, L. P. Hu, and X. B. Zhao, *High performance Mg₂(Si, Sn) solid solutions: A point defect chemistry approach to enhancing thermoelectric properties.* Advanced Functional Materials, 2014. **24**(24): p. 3776-3781.

155. S. Y. Wang, X. Y. She, G. Zheng, F. Fu, H. Li, and X. F. Tang, *Enhanced Thermoelectric Performance and Thermal Stability in β-Zn₄Sb₃ by Slight Pb-Doping.* Journal of Electronic Materials, 2012. **41**(6): p. 1091-1099.

156. G. J. Snyder and E. S. Toberer, *Complex thermoelectric materials.* Nature Materials, 2008. **7**(2): p. 105-114.

157. K. Biswas, J. Q. He, Q. C. Zhang, G. Y. Wang, C. Uher, V. P. Dravid, and M. G. Kanatzidis, *Strained endotaxial nanostructures with high thermoelectric figure of merit.* Nature Chemistry, 2011. **3**(2): p. 160-166.

158. A. I. Boukai, Y. Bunimovich, J. Tahir-Kheli, J. K. Yu, W. A. Goddard, 3rd, and J. R.

Heath, *Silicon nanowires as efficient thermoelectric materials.* Nature, 2008. **451**(7175): p. 168-71.

159.   T. J. Zhu, C. G. Fu, H. H. Xie, Y. T. Liu, and X. B. Zhao, *High efficiency half-Heusler thermoelectric materials for energy harvesting.* Advanced Energy Materials, 2015. **5**(19): p. 1500588.

160.   V. Romaka, V. Chekurin, M. Shelyapyina, D. Frushart, Y. K. Gorelenko, Y. V. Stadnik, L. Romaka, and A. Gorin, *The conduction mechanisms in n-ZrNiSn intermetallic semiconductor heavily doped with a Cu donor impurity.* Ukrayins' kij Fyizichnij Zhurnal (Kyiv), 2007. **52**(1): p. 40-46.

161.   L. H. Huang, Q. Y. Zhang, B. Yuan, X. Lai, X. Yan, and Z. F. Ren, *Recent progress in half-Heusler thermoelectric materials.* Materials Research Bulletin, 2016. **76**: p. 107-112.

162.   C. B. Vining, W. Laskow, J. O. Hanson, R. R. Van der Beck, and P. D. Gorsuch, *Thermoelectric properties of pressure‑sintered Si$_{0.8}$Ge$_{0.2}$ thermoelectric alloys.* Journal of Applied Physics, 1991. **69**(8): p. 4333-4340.

163.   A. F. May, E. Flage-Larsen, and G. J. Snyder, *Electron and phonon scattering in the high-temperature thermoelectric La$_3$Te$_{4-z}$M$_z$ (M= Sb, Bi).* Physical Review B, 2010. **81**(12): p. 125205.

164.   Y. W. Chai and Y. Kimura, *Microstructure evolution of nanoprecipitates in half-Heusler TiNiSn alloys.* Acta Materialia, 2013. **61**(18): p. 6684-6697.

165.   G. Melnyk, E. Bauer, P. Rogl, R. Skolozdra, and E. Seidl, *Thermoelectric properties of ternary transition metal antimonides.* Journal of Alloys and Compounds, 2000. **296**(1): p. 235-242.

166.   K. Gofryk, D. Kaczorowski, T. Plackowski, J. Mucha, A. Leithe-Jasper, W. Schnelle, and Y. Grin, *Magnetic, transport, and thermal properties of the half-Heusler compounds ErPdSb and YPdSb.* Physical Review B, 2007. **75**(22): p. 224426.

167.   J. Pierre and I. Karla, *Giant magnetoresistance in RENiSb semiconductors (RE= Tb, Dy, Ho).* Journal of Magnetism and Magnetic Materials, 2000. **217**(1): p. 74-82.

168. K. Gałązka, S. Populoh, W. J. Xie, S. H. Yoon, G. Saucke, J. Hulliger, and A. Weidenkaff, *Improved thermoelectric performance of (Zr$_{0.3}$Hf$_{0.7}$) NiSn half-Heusler compounds by Ta substitution.* Journal of Applied Physics, 2014. **115**(18): p. 183704.

169. C. Fu, S. Bai, Y. Liu, Y. Tang, L. Chen, X. Zhao, and T. Zhu, *Realizing high figure of merit in heavy-band p-type half-Heusler thermoelectric materials.* Nat Commun, 2015. **6**: p. 8144.

170. A. F. May, E. S. Toberer, A. Saramat, and G. J. Snyder, *Characterization and analysis of thermoelectric transport in n-type Ba$_8$Ga$_{16-x}$Ge$_{30+x}$.* Physical Review B, 2009. **80**(12): p. 125205.

171. G. A. Slack and S. Galginaitis, *Thermal conductivity and phonon scattering by magnetic impurities in CdTe.* Physical Review, 1964. **133**(1A): p. A253-A268.

172. S. I. Kim, K. H. Lee, H. A. Mun, H. S. Kim, S. W. Hwang, J. W. Roh, D. J. Yang, W. H. Shin, X. S. Li, Y. H. Lee, G. J. Snyder, and S. W. Kim, *Thermoelectrics. Dense dislocation arrays embedded in grain boundaries for high-performance bulk thermoelectrics.* Science, 2015. **348**(6230): p. 109-14.

173. J. Krez, J. Schmitt, G. Jeffrey Snyder, C. Felser, W. Hermes, and M. Schwind, *Optimization of the carrier concentration in phase-separated half-Heusler compounds.* Journal of Materials Chemistry A, 2014. **2**(33): p. 13513-13518.

174. E. Rausch, B. Balke, T. Deschauer, S. Ouardi, and C. Felser, *Charge carrier concentration optimization of thermoelectric p-type half-Heusler compounds.* APL Materials, 2015. **3**(4): p. 041516.

175. J. Schmitt, Z. M. Gibbs, G. J. Snyder, and C. Felser, *Resolving the true band gap of ZrNiSn half-Heusler thermoelectric materials.* Materials Horizons, 2015. **2**(1): p. 68-75.

176. S. D. Guo, *Importance of spin–orbit coupling in power factor calculations for half-Heusler ANiB (A = Ti, Hf, Sc, Y; B Sn, Sb, Bi).* Journal of Alloys and Compounds, 2016. **663**: p. 128-133.

177. V. A. Romaka, P. Rogl, V. V. Romaka, Y. V. Stadnyk, E. K. Hlil, V. Y. Krajovskii, and A. M. Horyn, *Effect of the accumulation of excess Ni atoms in the crystal structure of*

the intermetallic semiconductor n-ZrNiSn. Semiconductors, 2013. **47**(7): p. 892-898.

178. Y. Kimura and Y. W. Chai, *Ordered structures and thermoelectric properties of MNiSn (M = Ti, Zr, Hf)-based half-Heusler compounds affected by close relationship with Heusler compounds.* Springer, 2014. **67**(1): p. 233-245.

179. H. Matsuura, Y. Nishino, U. Mizutani, and S. Asano, *Doping effects on thermoelectric properties of the pseudogap Fe_2VAl system.* Journal of the Japan Institute of Metals, 2002. **66**(7): p. 767-771.

180. C. S. Lue and Y. K. Kuo, *Thermoelectric properties of the semimetallic Heusler compounds $Fe_{2-x}V_{1+x}M$ (M= Al, Ga).* Physical Review B, 2002. **66**(8): p. 085121.

181. M. Mikami, K. Kobayashi, T. Kawada, K. Kubo, and N. Uchiyama, *Development of a thermoelectric module using the Heusler alloy Fe_2VAl.* Journal of Electronic Materials, 2009. **38**(7): p. 1121-1126.

182. R. O. Suzuki and T. Kyono, *Thermoelectric properties of Fe_2TiAl Heusler alloys.* Journal of Alloys and Compounds, 2004. **377**(1): p. 38-42.

183. A. Ślebarski, M. B. Maple, E. J. Freeman, C. Sirvent, D. Tworuszka, M. Orzechowska, A. Wrona, A. Jezierski, S. Chiuzbaian, and M. Neumann, *Weak ferromagnetism induced by atomic disorder in Fe_2TiSn.* Physical Review B, 2000. **62**(5): p. 3296.

184. M. Nakabayashi, *Magnetic and transport properties in Heusler-type Fe_2TiSn compound.* Physica B: Condensed Matter, 2003. **329-333**: p. 1134-1135.

185. S. Yabuuchi, M. Okamoto, A. Nishide, Y. Kurosaki, and J. Hayakawa, *Large Seebeck coefficients of Fe_2TiSn and Fe_2TiSi: First-principles study.* Applied Physics Express, 2013. **6**(2): p. 025504.

186. D. I. Bilc, G. Hautier, D. Waroquiers, G.-M. Rignanese, and P. Ghosez, *Low-dimensional transport and large thermoelectric power factors in bulk semiconductors by band engineering of highly directional electronic states.* Physical Review Letters, 2015. **114**(13): p. 136601.

187. A. Ślebarski, *Electron-correlation effects in a disordered Fe_2TiSn Heusler alloy.* Journal of Physics D: Applied Physics, 2006. **39**(5): p. 856-864.

188. C. S. Lue and Y. K. Kuo, *Thermal and transport properties of the Heusler-type*

compounds $Fe_{2-x}Ti_{1+x}Sn$. Journal of Applied Physics, 2004. **96**(5): p. 2681.

189. H. Hazama, M. Matsubara, R. Asahi, and T. Takeuchi, *Improvement of thermoelectric properties for half-Heusler TiNiSn by interstitial Ni defects.* Journal of Applied Physics, 2011. **110**(6): p. 063710.

190. W. J. Xie, Y. G. Yan, S. Zhu, M. Zhou, S. Populoh, K. Gałązka, S. J. Poon, A. Weidenkaff, J. He, X. F. Tang, and T. M. Tritt, *Significant ZT enhancement in p-type Ti(Co,Fe)Sb–InSb nanocomposites via a synergistic high-mobility electron injection, energy-filtering and boundary-scattering approach.* Acta Materialia, 2013. **61**(6): p. 2087-2094.

191. C. G. Fu, S. Q. Bai, Y. T. Liu, Y. S. Tang, L. D. Chen, X. B. Zhao, and T. J. Zhu, *Realizing high figure of merit in heavy-band p-type half-Heusler thermoelectric materials.* Nature Communications, 2015. **6**: p. 8144.

192. T. H. Zou, T. T. Jia, W. J. Xie, Y. S. Zhang, M. Widenmeyer, X. X. Xiao, and A. Weidenkaff, *Band structure modification of the thermoelectric Heusler-phase $TiFe_2Sn$ via Mn substitution.* Physical Chemistry Chemical Physics, 2017. **19**(28): p. 18273-18278.

152

Curriculum Vitae

Personal Information

Name：	Tianhua Zou
Nationality：	Chinese
Date of birth：	1986.08
Sex：	Male
Personal status：	Single
Mobile phone：	04917645863096
Email：	tianhua.zou@imw.uni-stuttgart.de
Address：	Heisenbergstr.3, MPI-IS, 70569 Stuttgart, Germany

Education Background

- 12/2014-01/2018   Ph.D./Chemical Materials Synthesis

  University of Stuttgart   Germany

  Supervisor: Prof. Dr. Anke Weidenkaff

  Thesis: Synthesis and thermoelectric properties of chalcogenide and half-Heusler phases

- 09/2011-07/2014   Master/Condensed Matter Physics

  Chinese Academy of Sciences   China

  Supervisor: Prof. Dr. Xiaoying Qin

  Thesis: Synthesis and thermoelectric properties of β-Zn_4Sb_3-based nanocomposites

- 09/2007-07/2011   Bachelor/Physics

  Xiangtan University   China

  Thesis: Fabrication and electrochemistry properties of graphene supercapacitor

Personal Skills

- English: bilingual teaching, in charge of the exercises course and the lab course for masters.

- Software: proficient in Microsoft Office Suite, Origion/Canvas, Highscore/Fullprove.

- Equipment: good at Arc Melter, SPS, LFA/TG/DSC, ZEM/PPMS, SEM, XRD.

Intership

- Monitor   Bao Steel, Shanghai China   2010

  I was responsible for mechanical measurement of the construction steel.

Publications

- **>20** papers in **SCI** journals, H factor **10**, citations > **200**

International Conferences

- 15TH European Conference on Thermoelectrics, September, 2017, Padua/Italy, Poster

- 2ND Stuttgart Workshop on Thermoelectrics, August, 2017, Stuttgart/Germany, Oral

- 14TH European Conference on Thermoelectrics, September, 2016, Lisbon/Portugal, Poster

- 1ST Stuttgart Workshop on Thermoelectrics, August, 2016, Stuttgart/Germany, Oral

- 34TH Annual International Conference on Thermoelectrics & 13TH European Conference on Thermoelectrics, July, 2015, Dresden/Germany, Oral

- 5TH SPP1386 Status Meeting, February, 2015, Bad Aussee/Austria, Oral

- IUMRS-ICAM2013 International Conference on Advanced Materials, September, 2013, Qingdao/China, Poster

Leadership & Team Spirit

- Monitor   Xiangtan University   2008-2009

Honors & Awards

- National Scholarship/Merit Student   Chinese Academy of Sciences   2014
- Outstanding Graduate/National Scholarship   Xiangtan University   2011
- First Class Scholarship/Merit Student   Xiangtan University   2010